Articulated patient model in high-precision radiation therapy

Inauguraldissertation

zur Erlangung des Doctor scientiarum humanarum (Dr.sc.hum.)

an der

Medizinischen Fakultät Heidelberg

der

Ruprecht-Karls-Universität

vorgelegt von

Hendrik Tim Teske

aus

Heilbronn

2018

Dekan: Herr Prof. Dr. med. Wolfgang Herzog

Doktorvater: Herr Prof. Dr. rer. nat. Oliver Jäkel

Contents

Acronyms

3D	three dimensional
ART	adaptive radiation therapy
BFGS	Broyden-Fletcher-Goldfarb-Shanno
CC	cross correlation
CT	computer tomography
CTV	clinical target volume
DIR	deformable image registration
DoF	degrees of freedom
DVF	displacement vector field
FEM	finite element method
FoV	field of view
GPU	graphics processing unit
HU	Hounsfield units
IGRT	image-guided radiation therapy
IMPT	intensity-modulated proton therapy
IMRT	intensity-modulated radiation therapy
IQR	interquartile range
kV	kilo-voltage
L-BFGS	limited-memory BFGS
MI	mutual information
MRI	magnetic resonance imaging
OAR	organ at risk
PET	positron emission tomography
PTV	planning target volume
SSD	sum of squared differences
TRE	target registration error
VIRTUOS	virtual radiotherapy simulation
VMAT	volumetric-modulated arc therapy

Chapter 1

Introduction

While radiation therapy is a highly precise and individualized treatment modality to cure cancer, changes in the anatomy of the patient such as organ motion pose a challenge to the administration of the optimal dose deposition in the target volume. Modern radiotherapy technically enables a highly conformal dose distribution with desired steep dose gradients at the boundaries of the irradiated volume and the organs at risk (OARs) to maximize the effectiveness of the treatment. However, such steep dose gradients are always associated with a high sensitivity to anatomical changes. Especially for the treatment with particles capable to create excellent dose gradients, dose distributions are not only deteriorated by proximate changes in the underlying tissue, but also by range uncertainties, resulting from different tissue heterogeneities along the beam path. Accordingly, imaging and sophisticated image processing methods are crucial to monitor these changes as well as strategies need to be designed for compensation or plan adaptation.

Deformable image registration (DIR) has evolved as the key tool for tackling the challenge of assessing occurred anatomical changes within the images. However for commonly used intensity based DIR methods, comparative studies benchmarking the performance of various algorithms revealed large discrepancies in the resulting accuracy, with reported deviations reaching up to 13 mm (Brock 2010). Typical intensity based DIR methods offer a fast way to assess anatomical changes, but are prone to misregistrations in regions governed by homogeneous intensity values or imaging artefacts (Kirby et al. 2011). Moreover, said methods are mostly limited to merely considering changes in the intensity distributions of the images without taking into account the nature of the underlying tissue, such as different elasticities. Thus, also non-physical or implausible deformations can be observed. The nascent use of biomechanical models in radiotherapy research offers to incorporate knowledge and details about the anatomy into the transformation model of the registration process, which results in a more natural regularization in particular for homogeneous regions where intensity distributions alone do not provide sufficient information to control the deformation. In general, biomechanical models promise to offer an increased overall biofidelity. Research driven state-of-the-art approaches are still accompanied with the requirement of exhaustive pre-processing tasks, such as the need for tissue segmentation or mesh generation. Furthermore, highly detailed biomechanical models are associated with a high computational effort.

Especially in the head and neck area, where tumors are located in close proximity to OARs and a multitude of bones and joints constitute complex deformations, the coexistence of steep dose gradients and a highly precise deformation assessment is mandatory for achieving the best possible treatment. This puts rigorous demands in terms of accuracy,

robustness and biofidelity on the transformation models of DIR approaches. Moreover, the high flexibility of the underlying skeletal anatomy constitutes a large influence on directly related soft tissue deformations. Until today, finite element method (FEM) based models constitute a high proportion among the different biomechanical models used in radiotherapy research. Yet it is still unknown, which approach is best suited for each of the different applications. Particularly in the head and neck area, a kinematics-based multi-body physics model coupled to a soft tissue deformation model seems auspicious for the accurate and robust assessment of anatomical changes in the patient. Furthermore, amalgamation of this biomechanical model, a customized optimizer and an appropriate image similarity metric to consolidate a biomechanically enriched registration approach is necessary to automatically extract occurring anatomical variations. Hereby, robustness, computational efficiency as well as a strategy to fit the biomechanical model to the image data is emphasized.

In this work, a novel kinematics-based deformation model is developed, which offers a high biofidelity in mimicking complex inter-fractional changes of the skeletal apparatus of patients undergoing radiotherapy. The feasibility of propagating the skeletal transformations into the soft tissue is investigated by coupling the kinematic model to an existing soft tissue deformation model. It is shown that the developed model is capable to forward-generate various anthropomorphic postures of the skeletal anatomy, meeting the requirements for the head and neck area, which is characterized by its high anatomical flexibility. The influence of custom parametrizations such as the permissible degrees of freedom (DoF) of the joints on the overall deformation behaviour, the achieved performance and resulting consequences is examined in a landmark-based study to reproduce inter-fractional skeletal postures.

Furthermore, a prototype of a biomechanics based registration approach is realized as a retrospective proof-of-concept study for the automated assessment of inter-fractional anatomical deformations, involving both small and large posture changes. In this process, a pipeline representing the complex interplay of the kinematic model, an appropriate similarity metric combined with a custom optimization strategy is established. On the basis of re-sampled transformed clinical images of occurred inter-fractional changes, the impact of this biomechanics based registration approach is demonstrated. The resulting prototype of a biomechanical head and neck deformation model is regarded as the basis for the construction of an anatomically comprehensive in-silico deformable patient avatar.

Chapter 2

Materials and Methods

2.1 Radiotherapy

Radiotherapy is based on the principle to destroy tumor cells through beams of ionizing radiation, while best sparing the healthy tissue. Within the irradiated cells, irreparable damage to the DNA is induced, which eventually leads to the death of the malignant cells (Santivasi and Xia 2013). Hereby, the most common beam types are photons and particles, such as protons or heavy ions, which are characterized by different depth-dose profiles as illustrated in Figure 1.
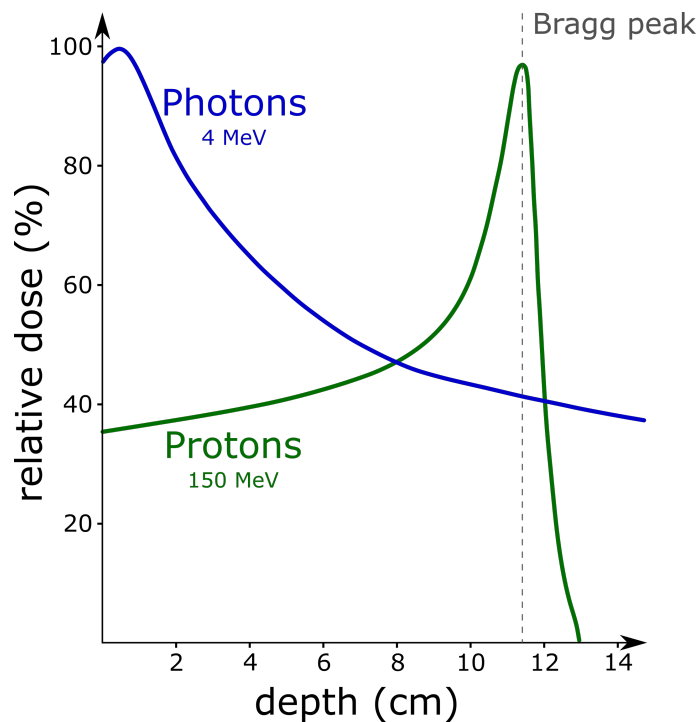

Figure 1: Illustration of the depth-dose profiles characteristic for photon beams (blue curve) and proton beams (green curve) in homogeneous matter. The bulk energy deposition of proton beams is found in the Bragg peak.

While photons show a nearly exponential dose falloff with their maximum energy deposited shortly after the entrance into the matter, particles such as protons or heavy ions deposit the bulk of their energy at a very local spot called the Bragg peak. The energy deposition finds its maximum when the particle has nearly completely slowed down and is minimal along the travelled path from the entrance to the Bragg peak. The spot of the bulk energy deposition, i.e. the location of the Bragg peak, can be modulated by the initial energy of the particles. For radiation treatment, such focused energy deposition is highly desirable because it enables the shaping of very steep dose gradients tailored to the patient anatomy. In particular, complex scenarios like the treatment of deeply located tumors surrounded by several OARs benefits from this possibility in achieving high doses in the target volume through superposition of several Bragg peaks, immediately flanked by low-dose regions for sparing the OARs.

Overall, particle treatment has the potential to offer a superior precision through focused range-modulated beams, compared to conventional photon treatment. However, a higher precision always comes with a higher sensitivity to potential anatomical variations and requires exact geometrical information about the structures of interest at the time of treatment.

2.1.1 Treatment planning

Radiotherapy treatment is preceded by a thorough planning process to determine the optimal dose distribution matching the individual anatomy of the patient for supporting the best achievable therapeutic success. This process involves an in-silico simulation of the dose application to find the best configuration in terms of beam parameters, which constitutes the treatment plan. To do so, volumetric image scans for localizing the tumor and OARs as well as electron densities of the tissues for dose calculation are required. Both, the geometrical information and the electron densities are usually obtained from X-ray computer tomography (CT) scans, however at the expense of additional dose exposure to the patient. To keep the additional dose at a minimum, the field of view (FoV) of the image scan is usually kept as small as possible to only cover the most critical anatomical structures. With the upcoming trend of treatment devices integrating magnetic resonance imaging (MRI) and a linear accelerator, non-ionizing imaging for radiotherapy planning can be harnessed with the additional benefit of providing a superior soft tissue contrast. As the electron densities can not be directly extracted from the intensity values of images obtained from MRI, different strategies were developed to overcome this issue through synthesis of artificial CT images based on tissue classification approaches (Hsu et al. 2013, Johansson et al. 2011) or atlas-based registration methods (Roy et al. 2014, Lee et al. 2017). Until today, acquisition of CT image scans for treatment planning is most common.

After image scan acquisition, delineation of the target volume and the OARs is mandatory for the identification of the exact geometrical boundaries of those structures, for which the target dose and dose constraints are imposed on during plan optimization. The delineation task is performed either in a completely manual way, assisted by semi-automated image processing methods or with the use of fully-automated approaches. While manual delineation is the most straightforward way of extracting the boundaries of the organs from the images, it is considered as a time consuming task for the clinicians and lacks reproducibility (Whitfield et al. 2013). Semi-automated delineation methods promise to considerably reduce the overall time required for this task. However, studies show that semi-automated delineation methods implemented in modern treatment planning systems

still require manual refinement of the resulting boundaries, since they only provide rough estimates of the actual anatomical structures (Sims et al. 2009, Ramkumar et al. 2016). Fully-automated delineation approaches are still subject to research and have not disseminated into clinics yet. Both the semi-automated and the fully-automated approaches mainly focus on OAR delineation. Those structures are clearly visible in most of the time, have distinct boundaries and show only minor variations in shape and appearance. On the contrary, this may not be the case for tumors. Additionally, the definition of the irradiated target volume also covers microscopic cancer cells, which usually are not visible at all in typical planning image scans. Consequently, the target delineation requires the expertise of an experienced clinician and is done manually in most cases. The use of additional imaging modalities can provide additional anatomical information for the delineation process. For example the use of MRI helps in delineation of structures located within the soft tissue or the integration of functional imaging such as positron emission tomography (PET) provides additional information about metabolic processes. The delineated structures of interest together form the static representation of the patient anatomy at the time of treatment planning, on which basis the dose constraints will be defined. Driven by clinical evidence and experience and constrained by the time available, this static model merely consists of the most relevant anatomical structures for the plan optimization, for which reason additional structures for example muscles or bones are not included and thus are usually not considered for delineation.

Desired dose values for the target and the maximum tolerable doses for the individual OARs are defined according to clinical guidelines. Together with the treatment devices available at the clinics, different beam configurations allow for precise irradiation of the target volume while ensuring the best possible OAR sparing. This is backed up by modern treatment techniques such as intensity-modulated radiation therapy (IMRT) and volumetric-modulated arc therapy (VMAT) for the treatment with photons and intensity-modulated proton therapy (IMPT) and raster scanning techniques for particles. Such modern concepts have shown improved dose coverage of target volumes located in close proximity to OARs and are associated with less radiation-induced side-effects by improving OAR sparing through shaping of steep dose gradients (Steneker et al. 2006, Palma et al. 2008, Scorsetti et al. 2010, Stieler et al. 2011, Holt et al. 2013, Romesser et al. 2016). Especially the head and neck area represents such a highly complex anatomical site, where tumors are often located in close proximity to many OARs (Feng and Eisbruch 2007).

The application of the prescribed dose is commonly divided into multiple treatment sessions, assuming fractionation might improve the therapeutic ratio between tumor eradication and late normal tissue injury through different radiobiological effects (Thames et al. 1983). Depending on the treatment context and tumor characteristics, hyperfractionated (Withers 1993) or hypofractionated (Pollack and Ahmed 2011) treatment schemes may be considered. In hyperfractionation, low radiation doses per fraction are applied over a high number of treatment sessions to exploit biological effects like hyper radiation sensitivity (Lambin et al. 1993, Joiner et al. 2001). In contrast, modern high precision radiotherapy enables the utilization of hypofractionation schemes, delivering high doses to the tumor in overall less treatment fractions. Consequently, an optimal sparing of healthy tissue must be guaranteed, which puts high requirements on the precision of the treatment. Therefore, there is a tendency towards using hypofractionation in combination with particle treatment (Carabe-Fernandez et al. 2010). The decrease in the number of treatment sessions is directly related to an overall reduction of radiation treatment time, potentially leading to a more cost-effective and less burdensome treatment for the patient.

2.1.2 Anatomical variations

As a logical consequence from fractionated treatment schemes, variations in the anatomy of the patient at the time of treatment compared to the planning phase are inevitable. Such inter-fractional changes on the one hand occur due to the inability to position the patient on the treatment table in an exact identical position and posture as during planning. On the other hand, gradual physiological changes of the anatomy over the course of radiation therapy, for example tumor shrinkage as a typical response to radiation treatment (Hoffmann et al. 2018) or weight loss of the patient (Albertini et al. 2008) commonly occurring in approaching late treatment fractions are sources of anatomical variations. Moreover, organ displacement can also be indirectly induced for example by different filling states of the bladder (Chen et al. 2018). Besides, also intra-fractional changes due to internal organ motion, induced by breathing or digestion need to be considered to ensure a precise dose delivery (Bortfeld et al. 2002, Bert and Durante 2011).

Since the treatment plan is based on the static anatomy of the patient at a specific point in time, anatomical deviations from the treatment plan in subsequent treatment sessions lead to deteriorations of the actual dose deposition. The higher the conformity of the planned dose distributions is, the potentially higher the negative implications on the actually delivered dose is, in case anatomical variations are present and are not accounted for. Especially for particle therapy, inter-fractional variations are one of the major sources for causing range uncertainties (McGowan et al. 2013).

Inter-fractional changes can be categorized into simple offsets and more complex deformations of the anatomy. While offsets represent rigid shifts in the position of the patient, straightforward countermeasures can be taken in order to bring the patient into the correct treatment position. For the assessment and compensation of deformations, usually more effort is required since they are characterized by combinations of non-linear dense transformations (Sotiras et al. 2013) on a global and local scale, depending on the elasticity properties of the underlying tissue. A prominent example for deformations occurring in the head and neck region are changes in the orientation and position of the bones, which propagate into the soft tissue, invoking non-linear changes to the geometry of adjacent organs. In contrast to offsets, the assessment and compensation of deformations in general is a more challenging task.

2.1.3 Consequences of deformations

The existence of deformations in the anatomy at the time of treatment implies deviations from the planned dose distribution. If not corrected for, this could lead to the deposition of excessive doses in healthy tissue and OARs if they are located near dose fall-off regions (Mori et al. 2008), potentially causing severe side-effects. Moreover, deformations might also impair the coverage of the target volume. The sensitivity of irradiation to anatomical deformations is strongly influenced by the steepness of dose gradients, the dose per fraction and the beam type. The steeper the dose gradients are, the higher the chances that normal tissue is located in regions with a high prescribed dose after the anatomical change. This is especially problematic under hypofractionated treatment schemes, where relatively high doses are delivered per fraction. This makes particle treatment particularly vulnerable to deformations since it allows for steep dose gradients and is often conducted as a hypofractionated treatment.

Moreover, deformations induce range uncertainties of the particle beams, leading to over- or undershoot effects. Changes in the tissue heterogeneity along the beam path have

a direct impact on the location of the Bragg peak, i.e. the high-dose spot. For example the shift of an air cavity into the beam path as a result of a deformation can cause a longitudinal shift of the Bragg peak and thus leads to an overshoot effect as illustrated in Figure 2. In case of an OAR located directly behind the target, it may receive an intolerable dose. Kumagai et al. (2009) observed overshoot and undershoot effects in pancreatic cancer treatment caused by bowel gas movement, leading to dosimetric variations. Accordingly,
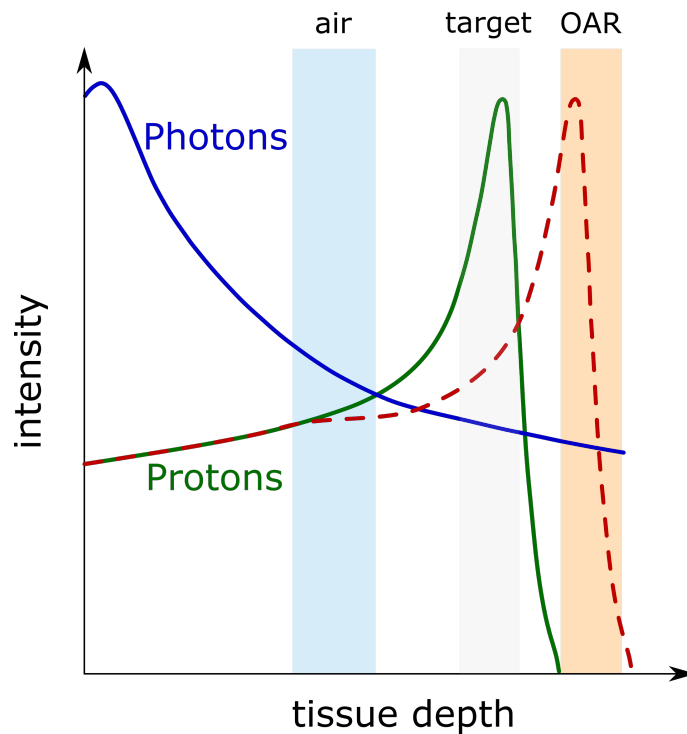
Figure 2: Illustration of the impact of changes in the tissue density along the beam path on the depth-dose profiles of photons and protons. The shift of an air cavity into the beam path results in a longitudinal shift of the bulk energy deposition for protons (dashed red line), which leads to an over-shoot effect of the target, potentially delivering high doses to an adjacent OAR.

undershoot effects can occur when more dense structures move into the beam path. For example in prostate cancer treatment, daily variations of the soft tissue and femur rotations have shown a severe impact on the lateral tissue thickness (Trofimov et al. 2011), thus potentially affecting the path length of particles.

2.1.4 Motion management

Due to the high flexibility of the human anatomy and its accompanying heterogeneous deformation behaviour, the management of deformations during radiotherapy becomes one of the most crucial tasks to guarantee the best possible treatment for the patients. In order to reduce inter-fractional changes to a minimum during radiotherapy, effort is taken to bring the patient into the same position as during treatment planning.

The treatment of different tumors, located in different areas of the body require the patient to be treated in a specific posture to be most effective. The posture is determined according to clinical guidelines, but also depends on the patient's comfort. For example in

lung or breast cancer treatment, patients typically are positioned in an arms-up posture to avoid unnecessary irradiation of the arms. Particularly in particle therapy, also arms-down postures become possible with the advantages of being more comfortable for the patient, which leads to better perseverance of that posture during longer treatment sessions (Depauw et al. 2015). Different strategies exist to assess and compensate for anatomical variations in the patient anatomy remaining after the initial positioning of the patient.

2.1.4.1   Immobilization

Immobilization is used before treatment in assisting the re-positioning of the patient to mitigate the effects of inter-fractional variation and during treatment to retain the posture of the patient and to mitigate intra-fractional motion. In both scenarios, treatment uncertainties are effectively reduced. Different immobilization techniques are used for different anatomical sites, for example in the head and neck area, scotch-cast masks fitting to the external surface of the individual patient are prepared during the treatment planning step and applied directly before treatment for re-positioning (Lohr et al. 1999, Jensen et al. 2012b). Alternatively thermoplastic masks are widely in use for immobilization of the head and neck region (Ostyn et al. 2017). However, the use of such devices does not guarantee an absolute immobilization and consistent patient setup (Amelio et al. 2013). For the head and neck area, a comparison study of scotchcast and thermoplastic masks led to the conclusion that both types result in comparable three dimensional (3D) re-positioning accuracies of approximately 3 mm to 4 mm on average (Jensen et al. 2012b). Similar results were found in a comparison study of different thermoplastic masks with systematic mean 3D errors of 2.4 mm to 3.1 mm for the head, 1.7 mm to 2.3 mm for the neck and 2.5 mm to 3.7 mm for the shoulder area (Gilbeau et al. 2001). A more sophisticated immobilization device for the head and neck area is presented by Ostyn et al. (2017) as a proof of concept to further improve the setup accuracy. For the head and neck area and beyond, vacuum mattresses commonly provide additional fixation and are used for daily re-positioning (Nevinny-Stickel et al. 2004).

Abdominal compression devices promise to limit intra-fractional motion of tumors for example located in the kidneys (West et al. 2018), the liver (Hu et al. 2017) or the lungs (Bouilhol et al. 2013) due to breathing. Other immobilization techniques such as deep inspiration breath-hold concepts require the active contribution of the patient during treatment and promise to facilitate the treatment of moving targets for both, photon and particle therapy (Boda-Heggemann et al. 2016).

2.1.4.2   Safety margins

A widely used strategy to account for uncertainties in patient setup, target motion and deformations is to define additional safety margins around the target volume. Margins are used to ensure a consistent target coverage in the presence of the uncertainties by increasing the actually irradiated volume. However, the irradiation of a larger volume always comes at the cost of higher dose to the normal tissue surrounding the target, which is in conflict with the aim of a highly precise dose delivery. According to the International Commission on Radiation Units and Measurements, standards for margin definitions in the context of IMRT were defined (International Commission on Radiation Units and Measurements 1993, 1999). While the definition of the clinical target volume (CTV) includes the macroscopic malignant tissue as well as potential microscopic tumor

infiltrations, the planning target volume (PTV) also accounts for uncertainties arising from patient setup and organ motion.

Deriving the extent of the margins in order to guarantee a safe treatment of the patient on the one hand while ensuring full target coverage on the other hand plays an important role in treatment planning. Early margin recipes for photon treatment were defined by van Herk et al. (2000) using dose-probability based approaches, which were widely adopted in clinical routine. The CTV to PTV margin is used to ensure that 90% of a patient cohort has a CTV coverage of more or equal to 95% of the prescribed dose (van Herk 2004). Since then, research over the last years is focusing on new methods to derive reduced margins without losing robustness and deterioration of target coverage (van Kranen et al. 2016, Witte et al. 2017). Studies have shown that for a typical IMRT head and neck cancer treatment, CTV to PTV margins of 3 mm maintain local tumor control (Chen et al. 2014b). For the treatment with particles, the PTV concept can not be adequately applied. Rather beam-specific margins need to be defined, including proximal and distal margins (Li 2009). In general, a larger safety margin is always connected to a less conformal dose distribution (McGowan et al. 2013).

2.1.4.3 Image-guided radiotherapy

In image-guided radiation therapy (IGRT), image scans of the anatomy just before treatment are acquired for the purpose of reducing geometric setup uncertainties. Therefore, either in-room CT on-rails linear accelerator combinations (Thieke et al. 2006, de Crevoisier et al. 2006) or cone-beam CT imaging devices attached to the gantry (Oelfke et al. 2006) are widely used. This enables an imaging while the patient remains immobilized for treatment. Recent MRI guided approaches (Mutic and Dempsey 2014) allow for non-ionizing imaging with the benefit of a higher soft tissue contrast.

By comparison of the fraction image scans to the image scans obtained during treatment planning, offsets in the target volume or OARs can be calculated and consequently, a correction vector for the treatment couch can be derived. Such translational shifts of the patient can be mechanically corrected by most treatment tables. Conventionally, rigid image registration is used to derive such correction vectors. In a study investigating the remaining setup uncertainties after IGRT correction, van Kranen et al. (2009) report on an overestimation of the precision when quantifying the overall setup accuracy by rigidly matching a large region in the images. Local systematic deformations and random deformations were observed to be larger compared to the evaluation on a global scale, ranging up to 3.4 mm and 1.5 mm, respectively. Modern commercial systems additionally allow for mechanical correction of rotations using a 6 DoF robotic treatment couch (Gevaert et al. 2012b), further reducing remaining setup uncertainties (Gevaert et al. 2012a). Although IGRT is an effective concept to achieve smaller PTV margins by correcting for patient offsets, anatomical deformations are not accounted for and still remain.

2.1.4.4 Adaptive radiotherapy

In adaptive radiation therapy (ART), sophisticated image processing methods are used to account for deformations in the anatomy of the patient with the aim of reducing the inter- and intra-fractional uncertainties to a minimum. It follows the concept of adapting the initial treatment plan to the anatomy at the respective time throughout the whole treatment process. Compensation of intra-fractional deformations can be realized by gating (Keall et al. 2002) or real-time tracking (Colvill et al. 2016) approaches. Plan-of-the-day

or adaptive replanning approaches promise to consider inter-fractional deformations before each treatment session.

In a plan-of-the-day approach, a library of different treatment plans representing different treatment scenarios and anatomical variations is generated, from which the best fitting plan at the respective time is selected right before the treatment fraction, depending on the current anatomy of the patient. The generation of such a library of plans requires access to representations of typical anatomical variations in the area of interest, for example either by acquisition of multiple images of the same patient on different days (Chen et al. 2013) or by using motion models of specific organs to provide an estimate of their geometrical variations (Heijkoop et al. 2014). Potential dosimetric benefits from following a plan-of-the-day concept were reported for the treatment of cervical cancer (van de Schoot et al. 2017, Seppenwoolde et al. 2016) and bladder cancer (Meijer et al. 2012). However, plan-of-the-day approaches are not yet widely available in clinical routine due to the fact that most commercial treatment planning systems are lacking relevant features like the automated generation of treatment plans, causing the manual generation and evaluation of multiple treatment plans per patient to be a very time consuming task. Moreover, the whole plan generation, evaluation and decision making process puts high demands on automated data processing routines. First clinical implementations of the plan-of-the-day approach were reported (Meijer et al. 2012, Heijkoop et al. 2014, Seppenwoolde et al. 2016, Hafeez et al. 2017). It was already shown that an automated generation of treatment plans is feasible even for complex VMAT scenarios and promises treatment plans of high quality (Sharfo et al. 2016). Depending on the magnitude of the remaining anatomical deviations between the selected best fitting plan and the actual anatomy of the patient, reduced margins are still required to compensate for these uncertainties.

Instead of providing a library of plans before each treatment fraction, the adaptive replanning approach aims at immediately taking into account the current inter-fractional deformations and the already delivered dose from previous fractions, followed by an on-the-fly calculation of a new treatment plan tailored to the current anatomy. Different replanning strategies exist, ranging from updating the treatment plan once after a fixed number of fractions have passed to the generation of a new plan on a daily basis in case the deformations exceed predefined thresholds (Dawson and Sharpe 2006), realized in offline or online approaches (Lim-Reinders et al. 2017). For rendering an online replanning approach clinically feasible, the newly generated treatment plans need to be available shortly after the fraction image scans were acquired to avoid additional time delays. The methods and tools involved in such an adaptive process are facing major challenges. The quantification of the anatomical changes regarding the initial treatment plan has to be robust and accurate since manual corrections entail additional time spent. Furthermore, the generation of a new treatment plan needs to be automated and achievable in reasonable time. In addition, new challenges to the conventional quality assurance program arise (Yan 2008, Peng et al. 2011). For replanning strategies implementing one to three re-planning events in the head and neck area, dosimetric benefits compared to conventional IGRT were reported (Schwartz et al. 2012, 2013, Wu et al. 2009, Kataria et al. 2016, Ahn et al. 2011, Jensen et al. 2012a, Chen et al. 2014a, Góra et al. 2015). First clinical trials for online adaptive replanning in head and neck cancer were enrolled and potential clinical feasibility is indicated (Mao et al. 2017). The feasibility of an automated generation of prostate treatment plans in less than two minutes was reported (Kontaxis et al. 2017). As of today, clinical experience in replanning approaches is limited regarding the time at which a replanning event should occur, dosimetric thresholds to trigger the replanning

event, the selection of patients potentially benefitting and the volumes as well as the extent of safety margins (Kataria et al. 2016).

A key role in ART comes to registration methods used to assess the occurred anatomical offsets and deformations based on the provided image scans. Accurate transformation models are required to describe such variations in an automated fashion within a reasonable time. Quantification of the variations is then used as the basis for further plan adaptation processes. Based on that, geometric and dosimetric thresholds can be determined to decide when to trigger a replanning event. In case replanning is indicated, delineated contours on the planning CT can be automatically propagated onto the fraction image scans to reduce the time needed for manual re-delineation. Furthermore, the dose is back-propagated onto the planning CT for consideration in the following fractions. Besides that, the demonstration of dosimetric advantages such as a better target coverage or an improved sparing of OARs in adaptive treatment concepts compared to conventional approaches become possible by using deformation models and registration approaches to describe and automatically extract these quantities from the image scans, making them indispensable for modern radiotherapy treatment concepts.

2.1.5 Image registration

Automated assessment of inter-fractional anatomical deformations is a prerequisite for ART. Image registration has become the tool of choice for such challenging task. Since its advent in the field of radiotherapy, a vast variety of algorithms with different underlying concepts and parametrisations were reported in literature (Maintz and Viergever 1998, Hill et al. 2001, Sarrut 2006, Sotiras et al. 2013, Brock et al. 2017). A transformation model, an optimizer and a similarity metric make up the three basic components of a registration method. Generally, registration methods share the common concept of taking both, the planning image scan and the fraction image scan as inputs in order to find the best transformation for aligning the anatomy. In an optimization procedure, the transformation model is iteratively fitted to the images, while the quality of the fit is continuously assessed by the means of the similarity metric.

The primary application of image registration is found in IGRT and ART for assessing anatomical deformations to either extract the best correction vector for patient re-positioning or to propagate the delineated contours of the planning image scan to the fraction images. In particular DIR, also accounting for non-linear changes, is additionally used to map the applied dose in the treatment fractions back to the planning image scan in order to obtain an estimate of the already applied overall dose. Besides that, the fusion of images originating from multiple different modalities such as PET or MRI to assist in individualizing the treatment (Leibfarth et al. 2013), support the delineation process (Kessler 2006) or enable the evaluation of the tumor response to radiation therapy (Bhatnagar et al. 2013).

In general, registration methods in the context of high precision radiotherapy face the challenge to provide reliable and accurate results within a short time. Depending on the application context, emphasis put on one or the other requirement may be stronger. While accurate results are desired to enable steep dose gradients, robustness of the registration methods is an increasingly important factor towards realization of ART and the associated need of automating image processing workflows. Timeliness of the algorithms is essential in online plan adaptation scenarios when the patient is positioned on the treatment table, waiting to get treated.

State of the art DIR methods used in radiotherapy on the one hand promise accurate results with associated uncertainties within the sub-millimetre range, evaluated on dedicated patient cohorts and regions of interest. On the other hand however, currently used DIR methods are prone to uncertainties in areas with homogeneous image intensities due to the lack of discriminant features like prominent intensity gradients (Kirby et al. 2011, Juang et al. 2013). Moreover, image artefacts, for example caused by dental fillings, are a common cause for a degraded performance of image registration methods (Brock et al. 2017). Misregistrations can also occur when features guiding the registration method are located in areas of highly similar intensity distributions like features found on the vertebrae within the spinal area. Furthermore, the achievable performance of DIR methods is affected by the choice of a suitable transformation model, optimizer and similarity metric (Brock et al. 2017). Each transformation model is associated with uncertainties since it only represents an approximation of the true deformations happening in the heterogeneous tissue. Furthermore, optimizer and similarity metric are both also very context-sensitive.

Brock (2010) revealed large discrepancies among the results of different registration methods, evaluated under the same conditions on a common data pool. In this comparison study, maximum errors of up to 13 mm were reported. Hardcastle et al. (2012) evaluated different DIR algorithms for the application of automated contour propagation from planning image scans to the fraction image scans and reported about 27% of the propagated target volume delineations required major manual corrections. Those findings highlight the necessity for a thorough evaluation of DIR methods for their clinical use (Brock et al. 2017).

2.1.6   Deformation models

Deformation models play a key role in describing anatomical changes in the context of ART. As part of an image registration method, they approximate the deformation behaviour of the underlying tissue and provide the resulting transformation as a displacement vector field (DVF). The DVF describes the deformation as the set of offsets corresponding to the image voxels between two or more image scans. Unlike rigid transformation models only accounting for global translations and rotations, deformation models usually provide more DoF in order to be able to represent non-linear transformations.

A variety of transformation models based on mathematical equations (Klein et al. 2010, Moteabbed et al. 2015), physical laws (Pyo et al. 2013, Gorthi et al. 2011, Wu et al. 2010, Ehrhardt et al. 2007, Crum et al. 2005) or biomechanical rules (Al-Mayah et al. 2015, Neylon et al. 2014, Li et al. 2016, Han et al. 2017) have been used. While the mathematical methods based on splines (Unser 1999) still are the prevailing deformation models used in radiotherapy, there is a noticeable trend over the last years towards using more sophisticated biomechanical models (Al Mayah 2018, chap. 5). Spline based models approximate deformations by mathematical interpolation between several supporting points, extracted as characteristic features from the images. Although such models are popular due to their general applicability, transparency and computational efficiency (Crum et al. 2004), they are likely to result in unrealistic deformation behaviour, deviating from that of the real tissue, depending on the number and distribution of utilized supporting points. Approaches using physically based deformation models such as fluid models (Crum et al. 2005) aim at improving the approximation of the deformation behaviour by providing a higher flexibility in representing large and highly localized deformations. By regularization through underlying physical laws, non-compliant deformations are avoided. Still, most physically

based deformation models do not differentiate between different tissue types. Biomechanical models promise to achieve a patient-individual and even tissue-individual deformation behaviour by incorporating detailed knowledge about the geometry and the nature of the involved materials and objects, such as their mechanical properties like stiffness or elasticity. This enables the description of even complex heterogeneous deformations of high biofidelity, but comes at the cost of increased computational load. In contrast to the models mentioned above, biomechanical models rely on additional information, which need to be obtained prior modelling. Deformation models based on biomechanics have been used for describing the deformation behaviour of various body regions like the head and neck area (Al-Mayah et al. 2010), the lungs (Han et al. 2017), the liver (Polan et al. 2017) or the prostate (Wu et al. 2006). However, the associated effort in construction and parametrisation of such models leads to the fact that the majority of biomechanical models reported in current literature are limited to specific anatomical regions or individual organs and can not be generally applied to the whole patient.

In the head and neck area, biomechanical models of different underlying concepts have been investigated. Al-Mayah et al. (2015) report on a FEM based biomechanical model showing improved registration performance when increasing the level of details in form of boundary conditions of skin, vertebrae, mandible and a dose-volume change coefficient. Neylon et al. (2014) have developed a spring-mass model to describe the heterogeneous deformation behaviour of the anatomy, achieving physically meaningful deformations. du Bois d'Aische et al. (2007) adopted a kinematics based transformation model for the spine coupled to a FEM based soft tissue model and show its feasibility in an automated registration approach.

The need for more realistic deformation models to support ART on the one hand and the increase in available computation power on the other hand has led to the development and use of more detailed deformation models. Especially in the context of daily replanning to compensate for complex anatomical changes, such models promise to provide a more accurate representation of the deformed anatomy at a greater expense of computation effort. Instead of transforming the image space to represent anatomical changes, most biomechanical models aim at virtually replicating the patient anatomy to build up an in-silico anthropomorphic patient model with a similar deformation behaviour. This model then can be deformed to represent the anatomy of the patient in different conditions while being less prone to uncertainties caused by homogeneous intensity distributions or imaging artefacts in contrast to conventional intensity-based models. While intensity-based deformation models may provide sufficiently good results for very small ranges of anatomical variations, biomechanical models promise to be accurate even for larger changes of the anatomy, like opening and closing of the mouth (Brock et al. 2017). Unlike the assessment of already occurred deformations in the anatomy, biomechanical models further provide the ability to forward-simulate arbitrary anatomical changes by making use of the extracted geometry information from the image data. Together with the mechanical laws to describe the deformation behaviour, the simulation of arbitrary anatomical states such as different postures of the patient becomes possible. Such a simulation of various deformations can for example be used for the generation of a library of different postures used in a plan-of-the-day approach (Heijkoop et al. 2014) or the biomechanical model can serve as a reference to benchmark clinically implemented DIR methods as part of implemented quality assurance measures (Teske et al. 2017b, Qin et al. 2018).

2.1.7   Validation of deformable image registration

Until today, little is known about the uncertainties associated with different DIR approaches and their consequences in ART. Validation of DIR methods is a prerequisite for their use in a clinical environment. Depending on the DIR application, different requirements must be met. While the geometrical uncertainties of DIR methods at the boundaries of the organs are of special interest for contour propagation scenarios, the accuracy of DIR algorithms within the whole image scan needs to be considered for dose-mapping or -accumulation scenarios. For the latter, Tilly et al. (2013) and Saleh-Sayah et al. (2011) have shown that even small geometrical errors can cause considerable dosimetric errors in regions with steep dose gradients.

Qualitative evaluation of the results of DIR methods can be supported by visual assessment of the remaining differences between the transformed image scan and the fraction image scan, usually performed manually with the help of image overlay techniques (Brock et al. 2017). Quantitative evaluation can be realized based on the use of identifiable anatomical landmarks, which are manually tagged by one or more observers (Castillo et al. 2009). By calculation of the target registration error (TRE) (Fitzpatrick and West 2001), the associated uncertainty can be determined. Although landmarks are considered as the gold standard approach for evaluation of DIR uncertainties, results are only reliable at the location of the defined landmarks. No inference can be drawn about uncertainties to be the same in areas between those landmarks (Oh and Kim 2017). This renders the evaluation by anatomical landmarks suitable in case many distinct features distributed across the whole area of interest can be identified or the deformation behaviour in areas between the landmarks is regularized by an anthropomorphic deformation model in a way that the uncertainty of such model can be assumed instead. Implantation of artificial markers in areas where few to none anatomical landmarks may provide remedy to a certain degree, is however not often considered due to the invasive procedure and its associated risks.

Contour based evaluation of the accuracy mainly provides insight about uncertainties at the boundaries of certain organs (Zhang et al. 2007). A prominent example is the calculation of the dice similarity coefficient (Dice 1945) as a measure of overlap between the delineated organs in both, the transformed image and the target image. However, contour based approaches lack the quantification of DIR accuracy in the inside of organs of interest (Pukala et al. 2013). Both, the results of landmark-based and contour-based approaches are dependent on interobserver and intraobserver variations of the experts, tasked to delineate the structures.

Deformable physical phantoms provide a way to generate known deformations of the physically replicated patient anatomy enriched with artificial markers (Kashani et al. 2007). After imaging of the phantom before and after the deformation, the offsets of the marker positions are regarded as the reference transformation. DIR methods using both images as input are evaluated based on the residual deviations of all marker positions. Drawbacks in deformable physical phantoms can be found in their anatomical structures, generally represented with a low level of detail and in the discrepancy between the deformation behaviour of the used materials for the phantom and the actual anatomical tissues, leading to potentially unrealistic deformations (Pukala et al. 2013).

Similar to replicating the anatomy by constructing deformable physical phantoms, computational patient models can provide reference deformations of the patient anatomy. These models range from simple geometric transformations (Lu et al. 2004) up to sophisticated biomechanical models (Segars et al. 2013, Neylon et al. 2014, Teske et al. 2017b).

For every induced deformation, the whole DVF is known and can be used as a reference for the evaluation of DIR methods. It has to be noted that the reliability of the results are totally dependent on the quality of the reference model. The assessment of uncertainties associated with DIR methods on the basis of DVFs provides the quantification of the accuracy on the voxel level, rendering such evaluation concepts suitable for dose-mapping and dose-accumulation scenarios.

2.2 Head and neck cancer

Cancers occurring in the different regions of the head and neck as shown in Figure 3 are collectively referred to as head and neck cancers. Despite their common description, they can be differentiated into the type of squamous cell carcinomas and salivary gland cancers. While the majority of the head and neck tumors arise from the squamous cells of the oral cavity, larynx and hypopharynx, there also uncommonly exist tumors in the salivary glands and the sinonasal tract (Stewart et al. 2014, p. 422). Head and neck
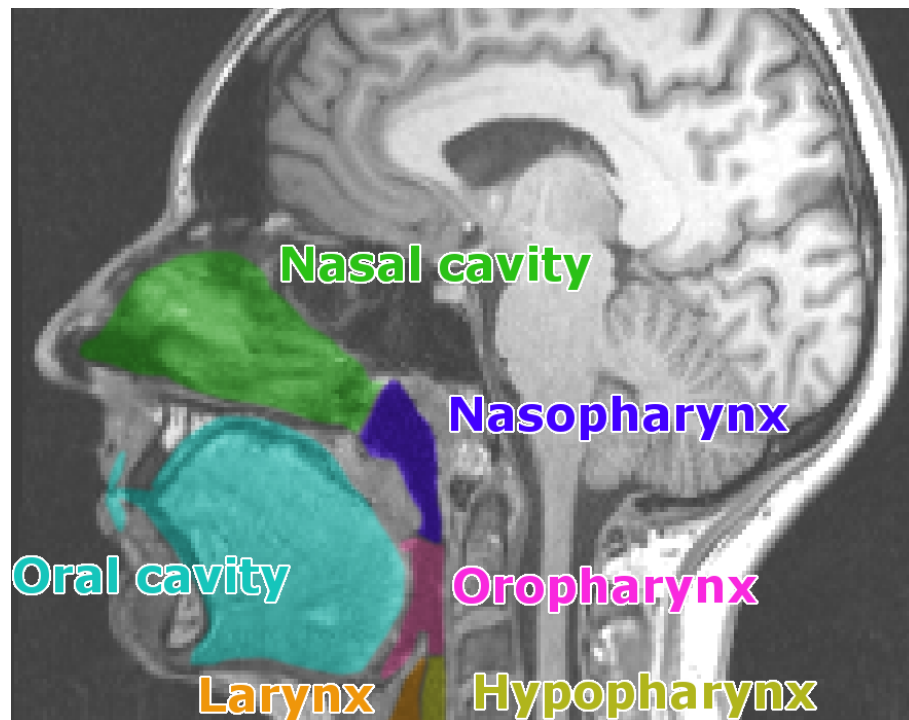
Figure 3: Illustration of the major sub-regions in the head and neck including the oral cavity, nasal cavity, nasopharynx, oropharynx, hypopharynx and larynx. The regions of interest are highlighted with different colors on an exemplary sagittal image slice acquired by MRI.

tumors involve the pharynx region, the larynx region, the oral cavity, the nasal cavity including the paranasal sinuses and the salivary glands.

The treatment of head and neck cancers extends from single treatment approaches of surgery, chemotherapy and radiotherapy towards a combined multidisciplinary treatment approach. For early-stage head and neck cancers, either surgery or radiotherapy is conducted. For locally advanced head and neck cancers, combinations of the single-modality

treatments promise improved prognosis, locoregional control and organ function (Lo Nigro et al. 2017).

Over the last years, major improvements in modern radiotherapy and surgery were achieved. While surgical treatment of early-stage head and neck cancers benefits from new approaches like the minimally invasive transoral endoscopic head and neck surgery, the precision of radiotherapy was considerably increased by the techniques of IMRT, VMAT and ART. Irradiation of head and neck cancer is a highly complex task due to many OARs that are located in close proximity to the tumor (Dirix and Nuyts 2010). The ability to precisely shape the high dose regions around the target volumes with steep dose gradients directly outside of these areas to spare normal tissue has shown to reduce radiation induced adverse side-effects, such as xerostomia (Nutting et al. 2011), dysphagia (Feng et al. 2010) or trismus (Kraaijenga et al. 2015). By taking into account the anatomical changes of the patient through treatment plan adaptation over the course of radiotherapy, improved local control (Schwartz and Dong 2011) and better quality of life scales (Yang et al. 2013) can be achieved. Further, the use of VMAT strongly reduces the treatment time while providing similar or better dose conformity to the PTV and OAR sparing (Alvarez-Moret et al. 2010). Future treatment approaches using IMPT promise further patient benefits by offering improved conformity of treatment plans. Prospective randomized trials comparing IMRT and IMPT for head and neck cancers are currently ongoing (Leeman et al. 2017).The use of highly conformal radiation treatment plans allows for adequate sparing of OARs like spinal cord, brainstem or salivary glands while maintaining high dose distributions in the target volume.

2.3 Patient data

In this work, the datasets of two exemplary patients are used for the evaluation of the developed kinematic model and its applications. The image data of one patient was acquired during a fractionated radiotherapy treatment, while the data of another patient consists of a pre-treatment and post-treatment scan. In this manuscript, the former is referred to as patient 1 and the latter as patient 2.

Patient 1
Patient 1 underwent typical IMRT for head and neck cancer treatment. A planning CT was acquired for treatment planning and fraction CTs were acquired before every fraction. Treatment was delivered over a total of 32 fractions. Immobilization was realized by a combination of a scotch-cast head mask attached to a stereotactic frame, a vacuum mould and small tattoos on the shoulders to assist in the positioning. As demonstrated in Figure 4, the FoV of the planning CT covers the region from the cranial end of the skull up to the 7th thoracic vertebra, the fractions range to the 6th thoracic vertebra.

Correction of the patient offset was realized with the pre-registration of a stereotactic frame attached to the head mask between the planning CT and all fractions. The planning image scans were acquired by a *Toshiba Aquilon* (Toshiba, Otawara, Japan) device with a slice distance of 3 mm and a pixel distance of 0.98×0.98 mm. Weekly kilo-voltage (kV)-CT images were acquired by a *Siemens Primatom* (Siemens OCS, Malvern, PA) scanner, which combines a linear accelerator with an in-room CT scanner.

Patient 2
Image data of patient 2 was obtained from *The Imaging Cancer Archive* (Clark et al. 2013) as part of the *Head-Neck Cetuximab Collection* (Bosch et al. 2015). The images
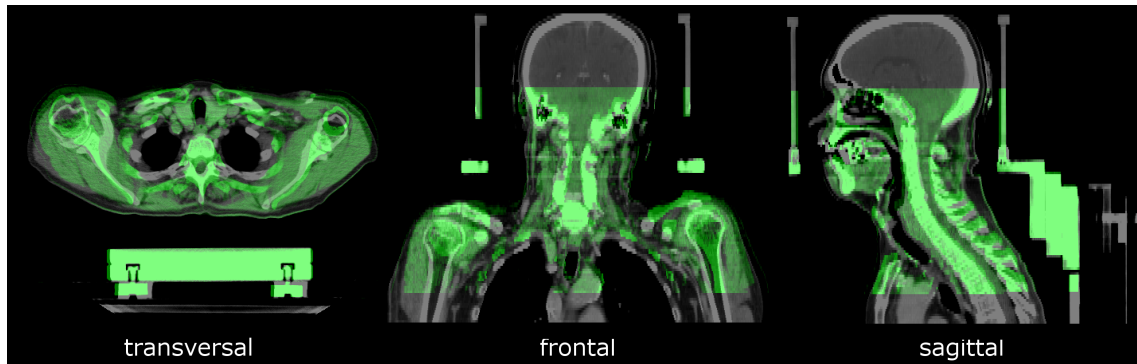
Figure 4: Image scans showing the anatomy of patient 1 at the time of treatment planning (grey) and before an exemplary treatment fraction (green) as overlay. Exemplary transversal, frontal and sagittal image slices show the inter-fractional changes in the anatomy.

were acquired in a randomized phase III trial of radiation therapy and chemotherapy for stage III and IV head and neck carcinomas with pre-treatment and post-treatment image scans for response assessment. As shown in Figure 5, the pre-treatment CT scan was acquired with the patient having his arms in an up position and covers the whole upper body up to the pelvis. The post-treatment CT scan ranges up to the 6th thoracic vertebra and shows the patient in an arms-down posture.
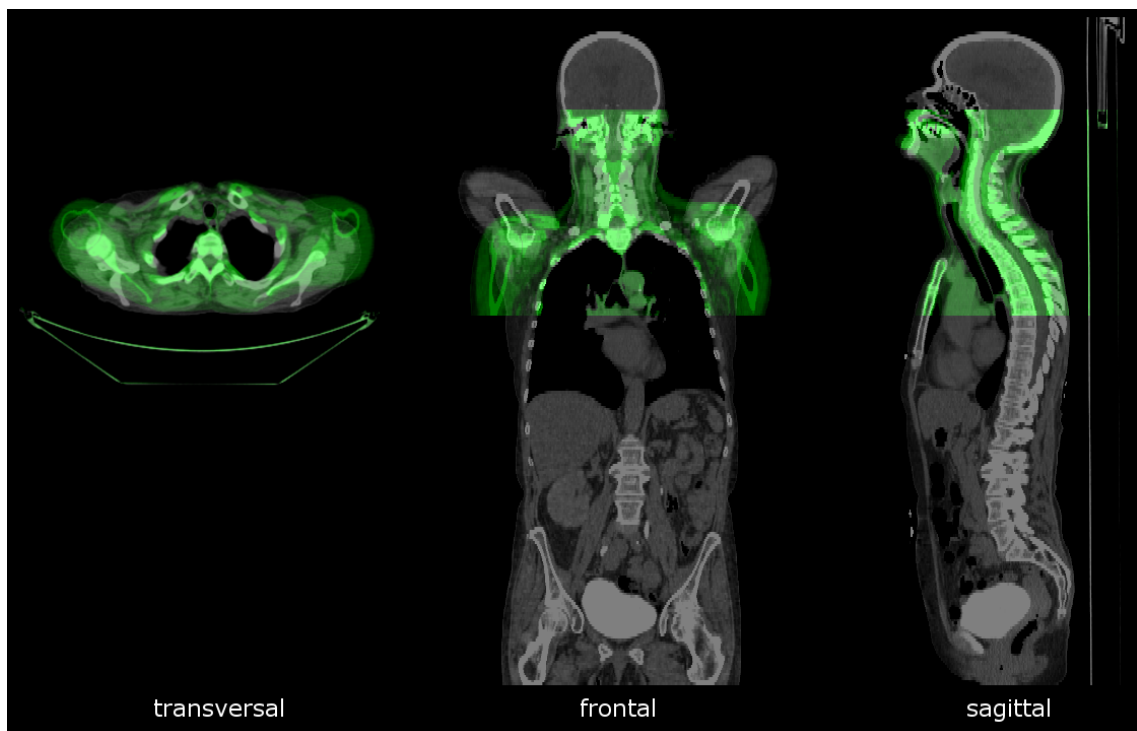

Figure 5: Image scans showing the anatomy of patient 2 at the time of radiotherapy treatment planning (grey) and after the treatment (green) as overlay. Exemplary transversal, frontal and sagittal image slices illustrate the large anatomical variation associated with the arms-up to arms-down posture change.

Pre-treatment and post-treatment CT image scans were acquired with a PET/CT *GE Discovery* (General Electric Medical Systems, Milwaukee, WI, USA) device and were already pre-registered. The slice distance is 3.75 mm and the pixel distance is 1.37×1.37 mm.

2.4   Software toolkits and libraries

In the context of this work, different software toolkits are used to support different tasks in the model construction and evaluation, the visualization, and the computations involved. Together with the contribution to this work, used toolkits are briefly introduced.

An in-house developed radiotherapy treatment planning system *Virtual radiotherapy simulation (VIRTUOS)* (Bendl et al. 1995) provides the underlying data structures, functionalities for visualization and methods to support the delineation of anatomical structures of interest. *Simbody* (Sherman et al. 2011) is an open source multibody physics toolkit, which supports inverse kinematics calculations as well as provides the data structures and associated functionality for rigid bodies, joints and constraints. A detailed description is found in section 2.8. *3D Slicer* (Fedorov et al. 2012) is an open source software platform for medical image processing and visualization. In this work, it is used to manually identify, tag and store anatomic and intensity-based feature points on the bones. The DIR method *Anaconda* (Weistrand and Svensson 2014), implemented in *Raystation* treatment planning system (RayStation 4.5.1, Raysearch Laboratories, Stockholm, Sweden), and the landmark-based DIR algorithm *Landwarp* (Shusharina and Sharp 2012) implemented in the radiotherapy image processing toolbox *Plastimatch* (Sharp et al. 2010) are used to for comparison purposes of the results achieved by the developed kinematic model during posture generation.

2.5   Computational optimization methods

Optimization in general can be described as a minimization of a function with n parameters. In contrast to brute force sampling of the whole parameter space and subsequent selection of the configuration yielding the best objective value, optimization strategies are used to find the solution in terms of the optimal set of values for the n parameters in a faster and more cost-efficient way. For example iterative optimization strategies achieve convergence to the best solution as soon as certain imposed convergence criteria are met. These are usually defined depending on the context of the optimization problem. Examples for simple criteria are a maximum number of iterations or the definition of an objective value, which is considered to yield a good enough solution to the problem. The convergence time can be improved by the evaluation of gradients or Hessians, which however come at the cost of a higher computational complexity per iteration. A meaningful initialization of the optimization method through a-priori knowledge about the data further lowers the time needed to find the solution.

A vast variety of optimization strategies exist. The choice of an appropriate strategy depends on multiple aspects. On the one hand, the characteristics of the optimization problems such as the nature of the objective function and constraints, the number of parameters or the smoothness of the function favour some optimization strategies over others (Nocedal and Wright 1999). On the other hand, also auxiliary conditions specified by the application requirements such as a fast convergence time, robustness against local

minima or even the extensibility of the algorithm further may have a considerable impact on the decision, which algorithm is the best suited.

2.5.1   Simplex downhill optimization

A widely used method to solve nonlinear optimization problems with multiple parameters is the simplex downhill method (Nelder and Mead 1965). In order to find the minimum in the objective function in a heuristic direct search method, a N-simplex with $N+1$ vertices is set up for a N-dimensional parameter space. For example a tetrahedron comprising four vertices is set up for the optimization of three parameters. After initialization, each vertex of the simplex represents a parameter configuration, for which an objective value is calculated. The vertices of the simplex are ordered according to this value. To find the minimum objective function within the parameter space, the vertex P_h associated with the highest objective value gets replaced in every iteration by a new vertex representing a new parameter configuration and thus resulting in a new objective value. The vertex P_l with the lowest objective value is maintained as it represents the best parameter configuration among the other vertices. By utilization of four basic simplex operations as shown in Figure 6, the optimization workflow is described as follows.

First, the vertex P_h is reflected at the centroid $\overline{P}$ of all vertices except P_h, resulting in a new vertex

$$P_r = (1 + \alpha)\overline{P} - \alpha P_h$$

with the reflection coefficient α. If the objective value of P_r lies between those of P_l and P_h, then P_h is replaced and the process is restarted. If P_r has reached a new minimum compared to the objective value of all previous vertices, P_r is expanded and a new vertex position is calculated according to

$$P_e = \gamma P_r + (1 - \gamma)\overline{P}$$

with γ being the expansion coefficient. If the objective value of P_e is lower than the one of P_l, P_h is replaced by P_e and the process is restarted. If P_r has reached a new maximum objective value, the new vertex position is calculated as

$$P_c = \beta P_h' + (1 - \beta)\overline{P}$$

with β as contraction coefficient and P_h' being the vertex with the minimum objective value among P_h and P_r. The vertex P_h is replaced by P_c and the process is restarted unless the objective value of P_c is higher than P_h'. In that case, all simplex vertices are compressed according to

$$P_i = (P_i + P_l)/2$$

with i ranging from 1 to $N + 1$ and the process is restarted.

In its original implementation by Nelder and Mead (1965), the simplex downhill algorithm is prone to converge in local minima of the objective function. Several approaches are reported in literature (Press and Teukolsky 1991, Luersen and Le Riche 2004, Chelouah and Siarry 2005), modifying the behaviour of the optimization approach or combining it with another optimization strategy with the goal of more robustly finding the global minimum instead.
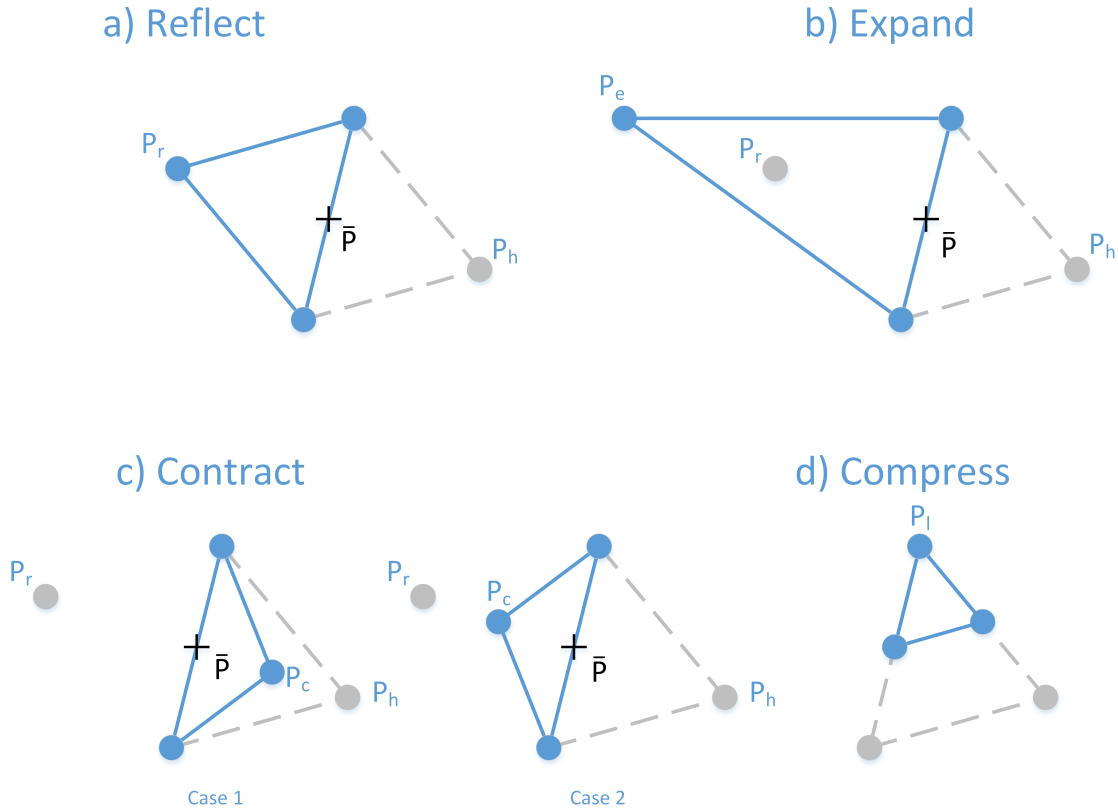
Figure 6: The four basic operations used in a simplex downhill optimization illustrated for three simplex vertices (points) sampling the search space. The vertices after any simplex operation (blue points connected by solid lines) resemble the new simplex originating from the previous simplex (grey points connected by dashed lines). Reflect, expand and contract involve the centroid $\overline{P}$ (black cross) of all vertices except the one with the highest objective value P_h. P_r, P_e and P_c denote the new vertices as a result of the operations. P_l is the vertex with the minimal objective value, which is not replaced. During the contract operation, either the vertex P_h or the vertex P_r is contracted depending on which has the lower objective value.

2.5.2   Broyden-Fletcher-Goldfarb-Shanno optimizer

The Broyden-Fletcher-Goldfarb-Shanno (BFGS) algorithm is an iterative optimization method for solving nonlinear unconstrained optimization problems. A fast convergence is achieved by maintaining a relatively low computation cost per iteration through the iterative approximation of the inverse Hessian. Instead of storing a full history of gradients needed for this approximation, the limited-memory BFGS (L-BFGS) variant of the optimizer only makes use of the most recent set of gradients, through which a reduction of the total memory needed is achieved (Liu and Nocedal 1989). This is especially advantageous for large-scale optimizations involving a large number of parameters.

2.6 Image registration

Image registration is the process of finding the geometric transformation between two image series, which leads to the best spatial alignment of both image contents. Here, the stationary image is referred to as the reference image and the image, which is transformed to match the reference image, is referred to as the moving image. The process of alignment is illustrated in Figure 7 and can be summarized as follows:
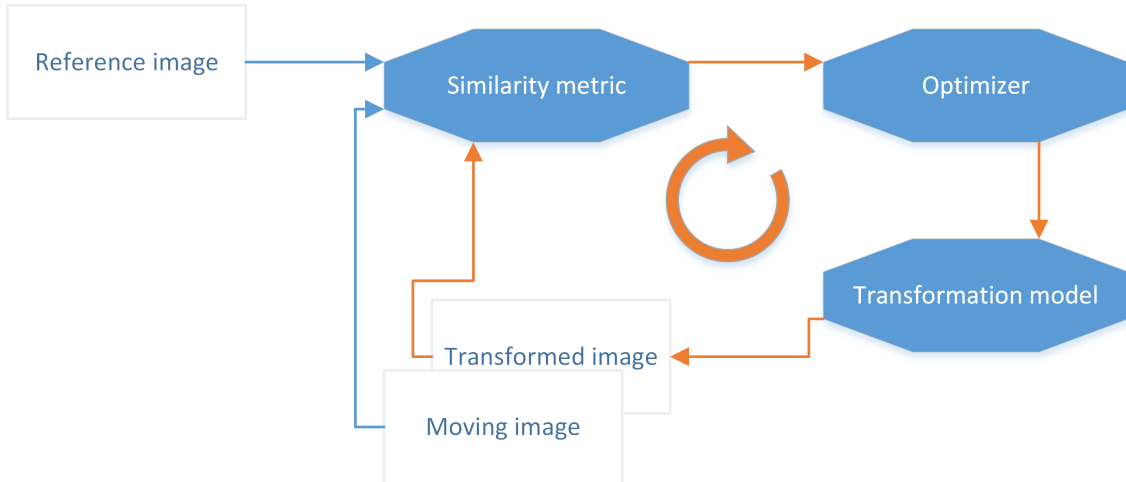
Figure 7: Schematic image registration pipeline as an iterative optimization process to maximize the similarity between the moving and the reference image. The basic modules are the similarity metric to quantify the degree of alignment, the transformation model to transform the image content and the optimizer to find the optimal parameters of the transformation model, which lead to the best alignment.

First, the similarity between the moving image and the reference image is calculated according to a similarity metric. In an iterative optimization process, the free parameters provided by the transformation model are updated and the moving image is then transformed according to the rules defined by the transformation model and subsequently re-sampled on the grid of the reference image. The resulting transformed image and the reference image are then used as input for the similarity metric in the next iteration. This process is repeated until both images are perfectly aligned, which is expressed as the highest similarity.

2.6.1 Transformation model

The transformation model specifies in which way an image or the content of an image can be transformed and thus has a large impact on the achievable registration result. In particular, it determines the number of free transformation parameters, which restrict the DoF of the solution space of the optimizer. The number of DoF is an important factor affecting the computation time.

A variety of transformation models exist. In order to achieve a rigid alignment of an object, a rigid body transformation model is used. If the object is deformable, the use of a non-rigid transformation model is required in order to adequately represent such changes. While the rigid body transformation model is a physical model having 6 DoF, deformable transformation models are realized in a variety of ways, typically involving much higher

DoF. Simple models have adopted geometrical deformation approaches interpolating the deformation within the image space. Hereby, supporting points are distributed in the image space with 3 translational DoF each. The transformation behaviour in between these points is exclusively defined by mathematical basis functions, which typically do not consider the underlying material properties of the objects represented by the images. Widely used basis functions in the medical field are thin-plate-splines (Bookstein 1989) or B-splines (Klein et al. 2007). More sophisticated transformation models respecting the material properties tend to include physical motion laws in order to mimic the deformation behaviour of the object. Popular biomechanical models to represent soft tissue deformations in the human anatomy are based on the FEM. Besides those, also other biomechanical approaches like spring-mass models or kinematics based approaches are under investigation as alternatives due to their potential to appropriately model anatomical variations at an overall lower computational cost. The transformation model affects the quality of the achievable registration result to a large degree by providing the ability to transform the objects the way they are actually transformed. The number of details the transformation model can be enriched with controls the permissible transformation space. This allows for the creation of specialized models to represent the transformation behaviour of dedicated objects, for example Chai et al. (2011) present a FEM based model for the human bladder. This way, transformations contradicting the transformation behaviour defined by the nature of an object can be prevented, which leads to a smaller solution space for the optimizer.

2.6.2   Similarity metric

The similarity metric serves as an objective function in the optimization process during image registration. It quantifies the dependence of two sample sets. Its maximum value is found in case both sets are fully dependent. Different metrics have been established for the calculation of the similarity between a pair of two images. In case both images are of the same modality, mono-modal similarity measures can be applied. Mono-modal similarity measures are based on the assumption that a linear relationship of the image intensities between both images exist. Multi-modal similarity metrics on the other hand are needed in case both images are of different modalities. For the latter, measures from the information theory have been successfully applied. Widely used mono-modal metrics are for example the sum of squared differences (SSD) (Sarrut et al. 2006) or the cross correlation (CC) (Samant et al. 2008). The mutual information (MI) (Maes et al. 1997) is the most popular method among the multi-modal similarity metrics. However, the MI is known to lose its statistical power with a decreasing sample size, rendering it inconclusive in case the sample size is too small (Andronache et al. 2006). This limits its use in estimating the local similarity between many small sub-regions of the images. Additionally in the context of image registration, used similarity metric estimators are affected by interpolation artefacts. These are likely to introduce additional local extrema in the overall objective function, making the optimization process more challenging (Pluim et al. 2000).

2.6.3   Optimizer

The role of the optimizer in the image registration process is to find the values corresponding to the set of transformation parameters, which minimize or maximize an objective function. To reach that goal in the most time-efficient way, an optimization strategy is

employed for updating the parameter values. Each change in the parameter values requires the transformation model to transform and re-sample a new image, which is then compared via the similarity metric.

Most popular optimization strategies follow an iterative approach to find the most efficient path in the solution space towards the global extremum. The choice of an optimization strategy is mainly driven by two main characteristics: Time efficiency and robustness. While the overall convergence speed can be increased by evaluating gradients or Hessians of the objective function, a benefit can only be achieved when these quantities exist for the given objective function and their calculation is not too costly. With the ubiquitousness of parallel computing, parallelized optimization strategies are increasingly adopted, promising a reduction of the overall computation time. The robustness of an optimization strategy, for example to consistently converge to a global extremum in the objective function, is directly related to the underlying optimization problem. A major challenge is the commonly non-convex characteristic of objective functions in image registration problems. The presence of many local extrema requires additional effort to find the global solution. While for example simulated annealing as an optimization strategy is a popular approach to find global extrema in objective functions which have multiple local extrema (Ehrgott et al. 2010), also the extension of local optimizers or a hybrid approach can improve the robustness to converge to the global extremum (Rahami et al. 2011). For image registration in the context of ART, a good time efficiency of the optimizer is essential in order to quickly assess inter-fractional anatomical changes and potentially trigger further steps towards replanning. Moreover, a high robustness is important to guarantee flawless registration results without the need to perform manual corrections to the resulting transformation afterwards. Online treatment plan adaptation can only be realized when both criteria are met.

2.6.4 Validation

Since image registration is an ill-posed problem, validation of its results relies on the approximation of the ground-truth deformations. Those are most commonly approximated by expert-defined surrogates, such as anatomical landmarks. Landmarks are salient anatomical points, which can be uniquely identified in pairs of images. Obtaining these landmarks in a fully automated way currently is not yet feasible, which leads to the fact that in most of the times landmarks manually defined by expert observers are used as the reference for the description of the true anatomical changes. Such a manual localization is known to be connected with intraobserver and interobserver variability (Vinod et al. 2016). Different observers may localize the same landmarks at a slightly different position due to a differing experience level. Variations even occur for the same observer, depending on the observer's condition. These observer-defined landmarks are used to assess the accuracy of image registration results. The accuracy is typically described by the TRE, which is defined as the mean distance between the transformed landmarks obtained by registration and the observer-defined landmarks, if the same landmarks are not used as input for the registration (Fitzpatrick and West 2001).

2.7 Biomechanical models

In contrast to conventional intensity based transformation models transforming the image domain, biomechanical models allow for considering different tissue properties. A bio-

mechanical model approximates the anatomical deformation behaviour by making use of mechanical methods. Adopted formalisms for mechanical laws provide specific parameters to consider different physical tissue properties like stiffness and shear. This allows for an assignment of tissue properties of different organs to the parameters in the mechanical motion laws. In contrast to conventional intensity based transformation models, assignment of tissue properties requires the exact geometry of the organs, usually obtained by delineation.

The availability of the organ geometries and their deformation behaviour described by mechanical laws provides the ability to forward simulate different deformations in reducing the number of input information required to describe the motion. While for example interpolation-based methods using supporting points to control the deformation require a large number of such independent points to be defined and translated consistently for simulating an organ deformation, a parametrized biomechanical model for example only requires the definition of a force, which is applied towards a point on the surface of the extracted geometry. Approaches based on different mechanical laws have been successfully translated for different anatomical regions in the human body.

2.7.1   Spring-Mass model

A spring-mass model represents the anatomy of the human body as a system consisting of mass particles, which are connected by springs and dampers. The deformation behaviour can be adjusted by changing the topology of the system, for example by changing the discretization level of the object or by altering the number of spring connections between the particles. Furthermore, the parametrization of the springs and dampers allows for the approximation of a tissue specific deformation behaviour.

The motion of each mass particle is described according to Newton's second law of motion

$$F(t) = -kx(t) - \beta \dot{x}(t) = m\ddot{x}(t)$$

with F being the force, the spring constant k, the dampening coefficient β, the mass m and the displacement of the spring x. To obtain the position of each mass particle after deformation of the whole spring-mass model, a system of coupled ordinary differential equations is to be solved.

Neylon et al. (2014) translate this concept to model deformations in the head and neck anatomy. Their spring-mass model additionally includes shear spring forces and dashpot damping forces. In general, spring-mass models can offer a computationally efficient way of modelling deformations of the human anatomy. However, most spring-mass models are known to be not convergent and may not meet the accuracy requirements for medical applications (Nealen et al. 2006).

2.7.2   Finite element method based model

The deformation behaviour of the human anatomy can be described by constitutive equations, which are based on physical laws. For example the tissue can be approximated as an elastic material, with its deformation characterized as a minimum variation of total energy as

$$\Delta = \frac{1}{2} \int_{\Omega} \sigma^T \varepsilon d\Omega + \int_{\Omega} F^T D d\Omega$$

with Ω being the continuous domain of the elastic body, F the external force, D the displacement in this domain, σ the stress vector and ε the strain vector (Chai et al. 2011). The FEM can be used to approximate the deformation behaviour of an elastic body by following a numerical approach for solving partial differential equations, expressing the physical laws on a discretised representation of this body. The problem domain ω is discretised into several small elements, frequently of tetrahedral form. Material properties can be assigned to each of the elements. Boundary constraints to neighbouring elements also need to be defined. Different material properties can be described by different values for the density, i.e. the mass per volume, the Young's modulus to modify the stiffness or elasticity of an element or the Poisson's ratio to model its compressibility. For achieving a model of high biofidelity, a qualitatively good approximation of these properties is required. For example to model anatomical deformations of the human body, extensible effort is required to approximate those properties for the different tissue types. The properties can be derived for example from strain tests on cadaveric specimen experiments (Egorov et al. 2002) or via elastography methods (Mariappan et al. 2010). Generation of the meshes consisting of the finite elements for the different tissue types require the extraction of the exact organ boundaries from the object representation. Subsequent refinement of these meshes may be necessary for example in order to decrease the element size in the mesh at specific areas of interest, where a higher accuracy is desired. Moreover, also additional manual refinement is often required, such as the smoothing of the mesh boundaries at sliding surfaces. Although the total DoF of a FEM based model can be reduced by an adequate choice of the used mesh types and mesh size, this method still is associated with a high computational cost.

2.7.3   Chainmail based model

A biomechanical model based on the chainmail concept follows the idea of subdividing the object of interest into a three dimensional grid of elements, which are connected to their neighbours by geometrical constraints. Transformations of the elements propagate along the connections throughout this grid. Geometrical constraints limit the relative deformations occurring between two adjacent elements and control the permissible range of translation as well as the range of the shear (Gibson 1997). This concept is illustrated in Figure 8.

The deformation of the whole object is described by the transformations of each chainmail element in the connected grid. One or more of these elements can serve as initiators of a deformation, which propagates throughout this grid. Through the adjustment of the constraint parametrization, the deformation behaviour can be adapted to heterogeneous object materials such as different tissue types (Schill et al. 1998). Because the elements of the chainmail approach can be directly derived from the image without the requirement of a dedicated mesh obtained via delineation, a direct mapping of image intensities to constraint parametrizations with a material transfer function becomes feasible. This way, the complex deformation behaviour of heterogeneous tissue can be represented. The original chainmail concept was further extended by allowing for rotational motion propagation, which has shown to improve the meaningfulness of the deformation results for the soft tissue in the head and neck area (Teske et al. 2017b). Further potential to include volume preservation was demonstrated to take into account tissue shrinkage or growth effects (Bartelheimer et al. 2017).
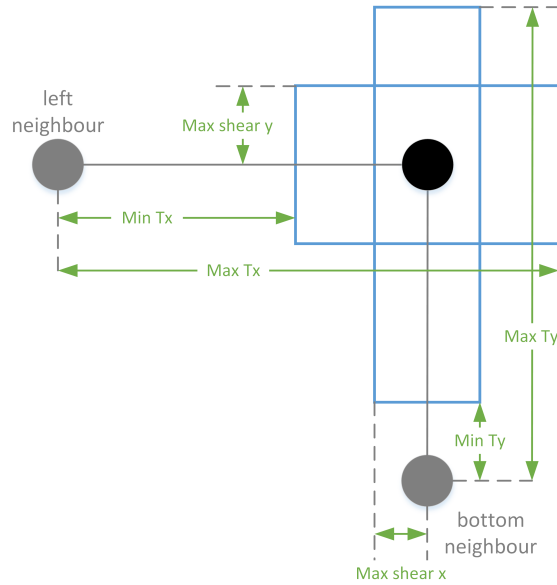
Figure 8: Illustration of the permissible motion range (blue boxes) of a chainmail element (black point) relative to its neighbours in the grid exemplary for the application in two dimensions. Minimal and maximal translation and shear constraints (green) are geometrically determined. Schematic according to Gibson (1997).

2.7.4   Kinematics based model

A kinematics based model in this work is referred to as a multibody system, describing transformations by kinematic motion laws. A multibody system consists of multiple rigid bodies, which are connected by joints. Two exemplary multibody systems are illustrated in Figure 9. The joints allow for relative motion between the bodies and can represent
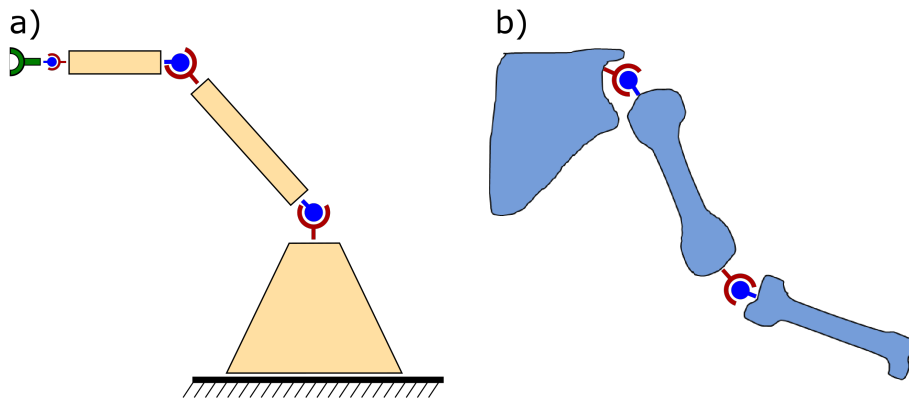
Figure 9: Two exemplary multibody systems representing a) a robot arm consisting of three rigid bodies (yellow) and an end-effector (green), connected by three joints in between and b) a humanoid arm with the bones modelled as the rigid bodies (light blue) connected by joints. Transformations of the individual rigid bodies are constrained by the DoF of the joints.

different translational or rotational DoF, such as prismatic joints having one translational DoF or ball and socket joints with three rotational DoF. A typical example for a multibody

system is a robotic arm, consisting of rigid parts, which are linked by joints. The end of the robotic arm is usually called the end-effector, e.g. representing the tip of a tool.

Kinematics in general is known as the study of motion without taking into account mass properties of the objects and forces acting upon them. In the context of a multibody system, it describes the mapping between parameters of the joints such as their rotation angles and the position coordinates of the rigid bodies. While the calculation of the position coordinates for the rigid bodies in a given multibody system as a function f of the specified values for the joint parameters is called forward kinematics and can be formulated as

$$X = f(\Theta),$$

where the vector of joint parameters is denoted as Θ and the vector of position coordinates of the rigid bodies is denoted as X, obtaining the joint parameters as a function f^{-1} of the rigid bodies' position and orientation is called inverse kinematics and can be described as

$$\Theta = f^{-1}(X).$$

With an inverse kinematics approach, the input in form of the position and orientation of the end-effector is enough to calculate all the joint parameters along the robotic arm as well as the coordinates of all other rigid parts. The connectivity of the rigid bodies allows for the propagation of the body transformations throughout the multibody system. However, the solution to an inverse kinematics problem is not necessarily unique and sometimes even does not exist due to the restrictions defined by the multibody system. The higher the number of bodies and joints in a multibody system is, the more parameter configurations lead to the same position and orientation of the end-effector. Many numerical approaches exist to solve inverse kinematics problems. The most prominent are Jacobian pseudoinverse methods (Whitney 1969), Jacobian transpose methods (Wolovich and Elliott 1984), damped least squares methods (Wampler 1986), cyclic coordinate descent methods (Wang and Chen 1991) or conjugate gradient methods (Zhao and Badler 1994). Each of the different methods comes with its own advantages and disadvantages depending on the definition and peculiarities of the problem, mostly in regard of numerical stability, computational efficiency, smoothness of the motion, scalability and extensibility of the methods.

As an exemplary method to solve the inverse kinematics equations, the Jacobian pseudoinverse approach is described (Buss 2004, Meredith and Maddock 2004). With this approach, the joint parameters Θ are iteratively approximated until the end-effector reaches its desired position. The incremental change in every iteration is obtained by the Jacobian matrix J as a function of Θ, which is defined as $J(\Theta) = (\frac{\partial f}{\partial \Theta_j})_j$. The forward kinematics equation to describe the velocities of the end-effector can be written as

$$\dot{X} = J(\Theta)\dot{\Theta}$$

with the dot notation denoting the first derivatives. The change in the end effector parameters ΔX caused by the change in joint parameters $\Delta\Theta$ can be estimated as

$$\Delta X \approx J\Delta\Theta.$$

This is rewritten corresponding to an inverse kinematics problem as

$$\Delta\Theta = J^{-1}\Delta X.$$

In an iterative process, first the difference between the target position X_t of the end-effector and its current position X is calculated as

$$\Delta X = X_t - X.$$

The Jacobian inverse is estimated with the Moore-Penrose pseudoinverse (Ben-Israel and Greville 2003, p. 27) J^+ as

$$J^+ = J^T (JJ^T)^{-1}.$$

The error of J^+ is estimated as

$$err = \|(I - JJ^{-1})\Delta X\|.$$

This process is repeated until ΔX is within a pre-defined error range. In the following iterations, the values for Θ are updated by the values of the current iteration (Meredith and Maddock 2004).

Besides its broad dissemination in the field of robotics, kinematics based models are also widely used for the animation of avatars, i.e. computer characters (Girard and Maciejewski 1985, Lee et al. 2009). Especially inverse kinematics plays a key role in the generation of various postures of the avatar due to the intuitive concept of transforming the rigid bodies instead of determining specific joint angles. The description of human-like motion with a kinematics based model is not limited to the use-case of animating avatars in computer games or movies, but can also be made use of in the medical field. Prosthesis construction in orthopaedics (Bandara et al. 2017, Chao and Lim 2013) and gait analyses in rehabilitation medicine (Carmo et al. 2012, Kainz et al. 2016) are only two possible applications, which have adopted kinematics to describe the motion and variations of the human skeletal anatomy. Kinematics based models of the skeletal anatomy offer a real-time capable anthropomorphic modelling of different postures by effectively reducing the parameters needed to those involved with the implemented joints.

2.8   Inverse kinematics realized by Simbody

Simbody is an open-source multibody physics toolkit for the simulation of articulated biomechanical systems and consists of a diverse set of tools to support the modeling of multibody systems as well as handles the solving of kinematic and dynamic equations of motion (Sherman et al. 2011). To ensure a computationally efficient simulation, internal coordinate formulations (Kane et al. 1983, chap. 1) are used. This provides the use of a minimal set of system equations, which can be formulated as computationally inexpensive ordinary differential equations (Seth et al. 2010), known as the *minimal coordinate set approach*. Moreover, this enables the use of coordinate projection methods (Eich 1993) as a robust and efficient alternative to conventional constraint stabilization methods to prevent numerical drift in the constraints (Masarati 2011). A prerequisite for internal coordinate formulations is to represent the kinematic chain, i.e. the rigid bodies connected by joints, as a topological tree structure. Such a kinematic tree describes a multibody system free of topological loops, which enables a considerably easier calculation of the equations of motion (Featherstone 2008, p. 3). The kinematic tree consists of elements, i.e. rigid bodies, which each are connected to one unique parent element, up to the root element of the tree. In the *Simbody* toolkit, a mobilizer completely specifies the permissible unconstrained motion between two rigid bodies connected by a joint (Seth et al. 2010). Such a mobilizer between the scapula and the humerus is illustrated in Figure 10.
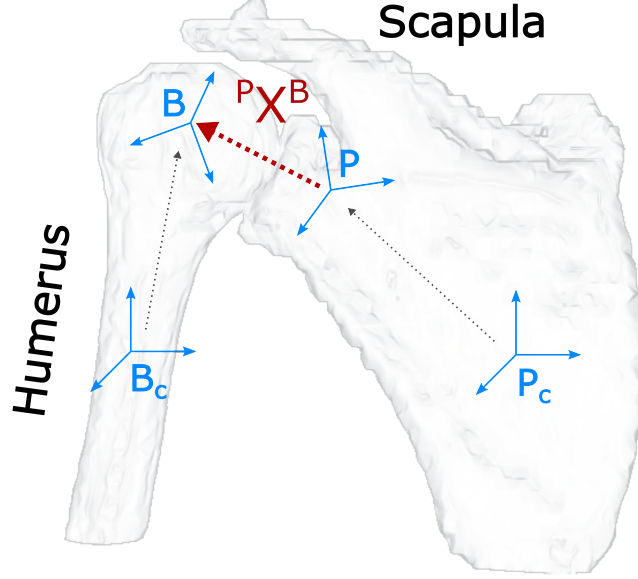
Figure 10: The mobilizer (red) specifies the permissible motion as the transformation $^PX^B$ between the scapula as the parent body P and the humerus as the child body B connected in a kinematic graph. The coordinate frames (blue) for the anchor points in the scapula and humerus are defined relative to the coordinate frames of the rigid bodies, defined in the centroids of the bones P_c and B_c, respectively. Dotted lines indicate relative coordinate transformations.

Each mobilizer introduces new coordinates and speeds, thus adding DoF to the overall multibody system. Mobilizers are described by its internal coordinates based on the concept of a hinge matrix (Jain et al. 1993). The mobilizer from parent body P to child body B is characterized by the following equations (Seth et al. 2016):

$$^PX^B \equiv \left[\begin{array}{cc} ^PR^B(q) & ^Pp^B(q) \end{array}\right], \tag{2.1}$$

$$^PV^B \equiv \left\{\begin{array}{c} ^P\omega^B(q,u) \\ ^Pv^B(q,u) \end{array}\right\} = {}^PH^B(q) \cdot u, \tag{2.2}$$

$$^PA^B \equiv {}^P\dot{V}^B = {}^PH^B\dot{u} + {}^P\dot{H}^Bu, \tag{2.3}$$

$$\dot{q} = N(q)u. \tag{2.4}$$

The transformation $^PX^B$ consists of the rotation matrix R and the translation vector p. Velocity $^PV^B$ and acceleration $^PA^B$ represent spatial quantities and are specified by the hinge matrix H and its time derivative $\dot{H}$. The spatial velocity consists of an angular part $^P\omega^B$ and a linear part $^Pv^B$. The kinematic coupling matrix N relates the time

derivatives of the generalized coordinates q to the generalized speeds u with the purpose of maintaining numerical stability (Sherman et al. 2011). Equations (2.1)–(2.4) define the relative kinematics of a rigid body with respect to its parent body. By recursive traversal of the kinematic tree from the root element to the most distal elements, the spatial kinematics of each body can be computed (Seth et al. 2016).

According to Seth et al. (2010), the transformation $^P X^B$ of an exemplary ball and socket mobilizer between parent body P and child body B is calculated as

$$^P X^B = \begin{bmatrix} ^P R^B(q) & 0 \end{bmatrix}$$

where $q = \{\theta_1, \theta_2, \theta_3\}$ is the Euler sequence of rotations. The ball and socket mobilizer only has rotational DoF. Its hinge matrix $^P H^B$ is defined as

$$^P H^B = \begin{bmatrix} 1 & 0 & 0 & 0 & 0 & 0 \\ 0 & 1 & 0 & 0 & 0 & 0 \\ 0 & 0 & 1 & 0 & 0 & 0 \end{bmatrix}^T$$

and specifies the spatial velocity of B in P. In case of ball and socket mobilizers $^P \dot{H}^B = 0$. The kinematic coupling matrix N maps from angular velocity to Euler angle derivatives:

$$N(q) = \begin{bmatrix} \cos\theta_3 / \cos\theta_2 & -\sin\theta_3 / \cos\theta_2 & 0 \\ \sin\theta_3 & \cos\theta_3 & 0 \\ -\sin\theta_2 \cos\theta_3 / \cos\theta_2 & \sin\theta_2 \sin\theta_3 / \cos\theta2 & 1 \end{bmatrix}.$$

In contrast to mobilizers granting mobility to the multibody system, kinematic constraints reduce mobility by imposing additional constraint equations, which enforce algebraic relationships between values of the mobilizer coordinates or their time derivatives. Such constraints can be defined on the level of generalized coordinates, speeds or accelerations. Constraints imposed between two rigid bodies can indirectly affect many other bodies depending on the connections in the kinematic tree and thus can be computationally expensive. All bodies affected by such constraints are found by iteratively traversing the kinematic tree in inboard direction, i.e. towards the root element, while determining the first body, which is a predecessor body shared by all bodies, directly affected by the constraints. All mobilizers along the paths are affected by the constraint equations. The concept of introducing constraints to the multibody system can be exploited to circumvent loops in the topology of the kinematic chain and thus to enable the use of an internal coordinate formulation. In a kinematic chain containing a topological loop, one of the rigid bodies associated with the loop is split into two parts, on which a holonomic constraint, i.e. a constraint on the position level, is imposed. Typically, a weld constraint type is used to inhibit any transformation between the two split body halves. This type of constraint adds six constraint equations to the multibody system.

Simbody provides a solver for inverse kinematics problems in case multiple end-effectors are defined within a multibody system, realized with an L-BFGS optimization approach according to the implementation proposed by Liu and Nocedal (1989). Multiple end-effectors mean that the positions and orientations for several rigid bodies are initially determined, while all joint parameters of the multibody system are sought via inverse kinematics. The different end-effectors may also be in conflict with each other, when for example the positions of all end-effectors cannot be satisfied at the same time. Pairs of corresponding points on the rigid bodies are used to define the input transformations on

the end-effectors. Each pair consists of a marker, which identifies a spatial location within the coordinate system of a rigid body, and an observation, which defines the desired target location of that marker in the world coordinate system. The goal of the optimization is to minimize the distance between marker and observation for every pair of corresponding points. The objective function can be defined as a weighted least squares problem as

$$\min_q \left(\sum_i^N w_i \|o_i - m_i(q)\|^2 \right)$$

where q is the set of joint coordinates in the multibody system, w_i is the weight associated to the ith pair of corresponding points, consisting of the marker m and the observation o. By default, all pairs of markers and observations are equally weighted. In the optimization approach, the set of joint coordinates q is sought, which minimizes the given objective function and satisfies holonomic constraints imposed within the multibody system.

2.9 Image processing methods

2.9.1 Image re-sampling

The content of a 3D image scan is usually sampled on a regular voxel grid of a fixed resolution. Applying a transformation T to such an image scan results in a transformed or even deformed grid. For example T can be described as a DVF, which holds the translation of each voxel to its new position, disregarding the original voxel grid. For obtaining an image scan after transformation, the transformed voxels together need to be re-sampled onto a regular grid. This is done by applying the inverse of the transformation T^{-1} to each transformed voxel and by subsequent interpolation of the voxels in between, which were not targeted by the inverse mapping function. State of the art re-sampling methods on image scans make use of parallelization techniques to implement the inversion of DVFs on modern graphics processing units (GPUs). For example Rodríguez Aguilera et al. (2015) present an interactive re-sampling algorithm, following a 3D rasterization technique, on the GPU.

2.9.2 Medial axis transform

The medial axis transform of a 3D object in a volumetric image scan can be defined as the set of all voxels corresponding to that object, which have more than one closest point on the surface (Xia and Tucker 2009a). The resulting topological skeleton of the object provides a reduced representation of the characteristic features of an object, and is thus often used in the field of shape analysis and image processing (Quadros et al. 2004, Näf et al. 1997, Macrini et al. 2011). There exist many different ways to calculate the medial axis transform of an object. Popular approaches are based on thinning (Palágyi and Kuba 1997), voronoi diagrams (Dey and Zhao 2004) and distance fields (Xia and Tucker 2009b). In the field of 3D image processing, the distance field of an object can be efficiently calculated on the voxel grid (Wang and Tan 2013). An exemplary illustration of the resulting topological skeleton produced with the use of a distance field method is shown in Figure 11 for a two dimensional image of a humerus bone.
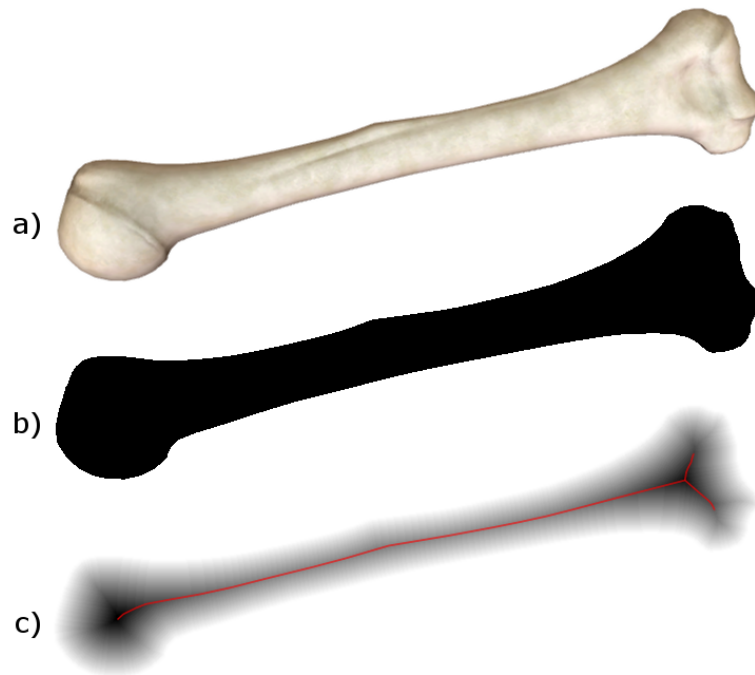
Figure 11: Illustrative process of calculating the medial axis transform of an exemplary humerus bone in two dimensions. The original representation of the bone is shown in a). After applying a binary mask in b), all voxels corresponding to the bone are shown in black. The resulting distance field on all those voxels is shown in c) where voxels with a larger distance to the surface obtain a darker grey value that those located closer to the surface. The medial axis of the bone is illustrated as a red line, representing the topological skeleton of the image of the bone.

Chapter 3

Results

The process of constructing the biomechanical deformation model based on the individual anatomy of the patient is described in section 3.1. The evaluation of the achieved accuracy and robustness of the model in reproducing smaller and larger changes in the posture of the patient using observer-defined landmarks is found in section 3.2. The forward-simulation of different arbitrary postures is demonstrated in section 3.3. Finally, the integration of the biomechanical model into an automated registration approach is covered in section 3.4.

3.1 Construction of a head and neck kinematic model

This chapter describes the construction of a biomechanical model for the assessment of deformations of the patient anatomy in the context of ART. Based on the assumption that changes in the skeletal anatomy are the most prominent source to cause deformations in the overall head and neck area, the developed biomechanical model focuses on the representation of different postures of the patient. The posture is mainly characterized by the positions and orientations of the bones, composing the flexible skeleton of the patient. A kinematic approach is utilized to describe changes in the skeletal posture. Based on those skeletal deformations, a heterogeneous chainmail based model is initialized to allow for the propagation of transformations of the bones into the soft tissue.

Kinematics describes the motion in a multi-body system, consisting of rigid bodies and joints (see section 2.7.4). This concept is transferred onto the human anatomy to describe the interplay of bones and connecting joints. The individual bones of the skeleton are treated as rigid bodies, rendering changes in position and orientation to be the only permissible transformations. Implemented joints then connect these bones according to the physiological joints in the human body. Controlled by the DoF of the joints, the position and orientation of the connected bones is described relative to each other.

3.1.1 Generic dependency graph

Construction of such a kinematics based model of the human anatomy requires knowledge about the relationship of the individual bones to their corresponding joints. The information which bone is connected to which joint is modelled as a generic dependency graph as shown in Figure 12, independent from the individual patient anatomy.

The dependency graph includes the majority of the highly mobile synovial joints in the region ranging from the skull down to the pelvis. Although bones and joints located at
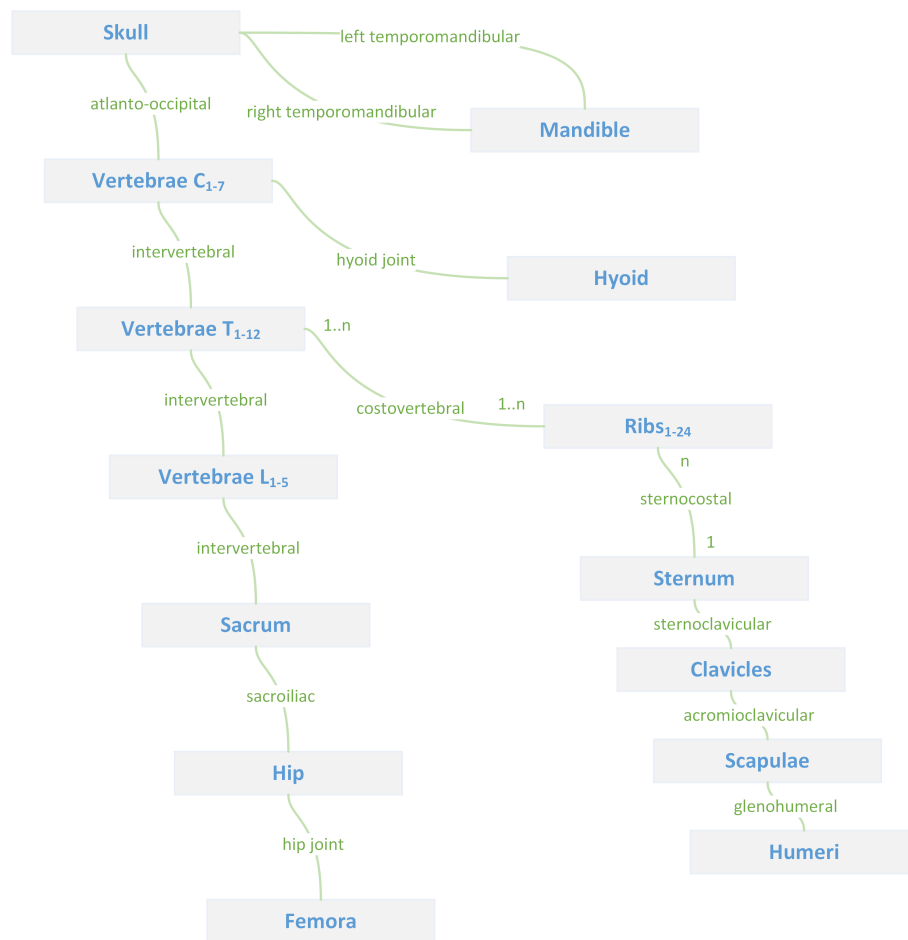
Figure 12: Illustration of the generic dependency graph of a subregion of the human skeletal anatomy, showing the relationship between the bones (grey boxes) and the joints (green connections). This graph includes the upper anatomy from skull to humeri and ranges in the pelvis down to the fermora. Skull and mandible are simultaneously connected by the two temporomandibular joints.

the outer extremities, such as the the hands or feet are not taken into account due to the fact that those regions do not contain OARs critical for radiotherapy and thus are usually outside the FoV of the acquired image scans, said bones and joints could easily be added to the graph. Also fibrous joints such as the sutures of the skull, characterized to grant little to no mobility, were not included in the dependency graph due to their marginal impact on the overall mobility of the skeleton.

3.1.2   Mapping of the individual anatomy

The generic relationship of the bones and the joints is transferred onto the individual anatomy of the patient, demonstrated for patient 1 as a typical head and neck image dataset (see section 2.3). Based on the volumetric image scans acquired for treatment planning, the individual geometry of each bone is obtained by manual delineation of the separate bones, followed by the extraction of their 3D voxelized representations. The delineations of the ribs additionally include the costal cartilages for simplification, which

are located adjacent to the sternum. Together, all the bones form the static skeleton of the individual patient, representing the anatomy at the treatment planning time (see Figure 13). The origin of the frame of reference for each bone is determined to be coincident with the calculated centre of mass of these extracted 3D representations, which will also be used as the origin for the coordinate frame for the corresponding rigid body in the multibody system.
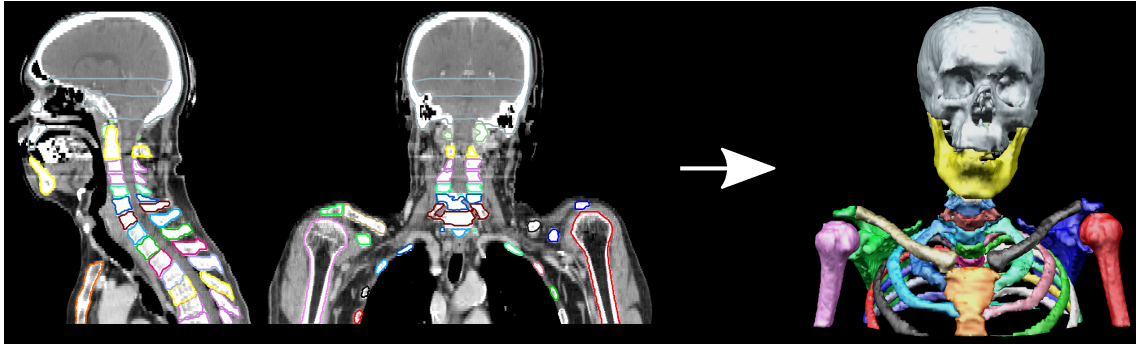

Figure 13: Illustration of the separately delineated bones of patient 1, highlighted by different colors, in an exemplary sagittal and frontal slice (left-hand side of the white arrow) and extracted as 3D representations (right-hand side), forming the static skeleton used as a basis for the kinematics based model.

3.1.3 Parametrization of joints

For the task of granting mobility to the extracted static skeleton, joints are included to connect the bones according to the dependency graph. To do so, the type, the number of DoF and the position of the centre of the joint need to be determined. Nearly all joints were approximated as ball-and-socket joints with 3 DoF, thus allowing for rotations around the body axes. One exception was made for the connection between the hyoid bone and the spine. Due to the fact that the hyoid bone is only distantly articulated to the vertebrae, a 6 DoF joint was used to connect the hyoid bone to the 5th vertebra in order to achieve a weaker coupling of the translations. In addition to rotations around the body axes, the 6 DoF joint also allows to represent translations in three directions. Due to a limited FoV in the planning image scans, some bones and joints may not be fully covered and as a result, may only be partially visible. Joints located outside of the images were not considered in the kinematic model. For the head and neck dataset of patient 1, this was the case for the lower sternocostal joints connecting the ribs to the sternum, starting from the 4th ribs downwards.

The locations of the joints relative to the bones determine the centres of rotation of the transformations happening in the skeletal anatomy of the patient. In order to automatically approximate the positions of the centres of the joints, two approaches involving different levels of detail were implemented. On the one hand, a straightforward approximation is based on the assumption that every joint can be adequately positioned in a nearest neighbour based approach. A more sophisticated method, on the other hand, comprises distinct joint positioning routines based on the individual joints (Teske et al. 2017a). Both approaches are compared in order to investigate if a simple nearest neighbour based approach is able to sufficiently position all joints.

The straightforward approach approximates the position of the centres of all the joints following a nearest neighbour calculation on each pair of connected bones. For that purpose, the smallest distance between any two voxels of the connected bones is calculated. The joint position is approximated to lie midway this distance. In the alternative approach, individual positioning routines were implemented encompassing the following bones.

a) The glenohumeral joint located between humerus and scapula is involved in large ranged motions such as the elevation of the arm. The position of a ball and socket joint should therefore lie in the centre of the humeral head to yield an improved approximation of the transformation behaviour in contrast to being located in the gap between the humeral head and the boundary of the scapula in a nearest neighbour approach. Veeger (2000) has already shown, that the centre of the humeral head represents a good approximation of the centre of a spherical joint. In order to algorithmically find the centre of the humeral head, a distance field is calculated on the delineated 3D representation of the humerus, yielding the minimal distance of every voxel to the nearest surface of the bone (see section 2.9.2). That voxel with the largest distance is considered as the centre of the humeral head, thus as the position of the joint.

b) The acromioclavicular joint is located between the scapula and the clavicle. Due to the proximity of both bones at several distinct locations, a positioning method alternative to the nearest neighbour approach is implemented. For that, the medial axes transforms of scapula and clavicle are calculated, based on which the joint position is determined to lie in the middle of the nearest distance between the points of both axes.

c) The costovertebral joint connects the tip of the rib to the corresponding vertebral body. Due to the complex shape of the vertebrae and the resulting ambiguity in nearest neighbour based positioning approaches along the whole spine, a custom positioning routine is applied. In order to robustly derive the joint centre, a distance field is calculated to determine the centre of the vertebral body and to yield the medial axes of the rib. Both, the centre of the vertebral body and that point on the medial axis of the rib, which has the nearest distance to the centre of the vertebral body, are connected by a line. Halfway its distance, the joint is approximated to be located.

d) The intervertebral joint connects two adjacent vertebrae. In order to achieve a positioning less affected by shape variations of the vertebrae, the location of the joint centre is approximated to lie halfway the distance of the line, connecting the centroids of two neighbouring vertebrae.

e) The atlanto-occipital joint connects the skull with the 1st cervical vertebra, called the atlas. In order to maintain a centred joint position, its location is estimated to lie on the curve, approximating the spinal curvature on a level with the points of contact of atlas and skull.

f) The hyoid joint describes the distant articulation of the hyoid bone in respect to the spine. In order to achieve a centrally located joint, its position is determined to lie halfway the distance between the line connecting the centroids of the hyoid bone and the 5th cervical vertebra.

Remaining joint positions are calculated according to the previously mentioned nearest neighbour approach. Both, the simple and sophisticated joint positioning approach are compared on the basis of visual assessment of the joint positions as partially shown in Figure 14.
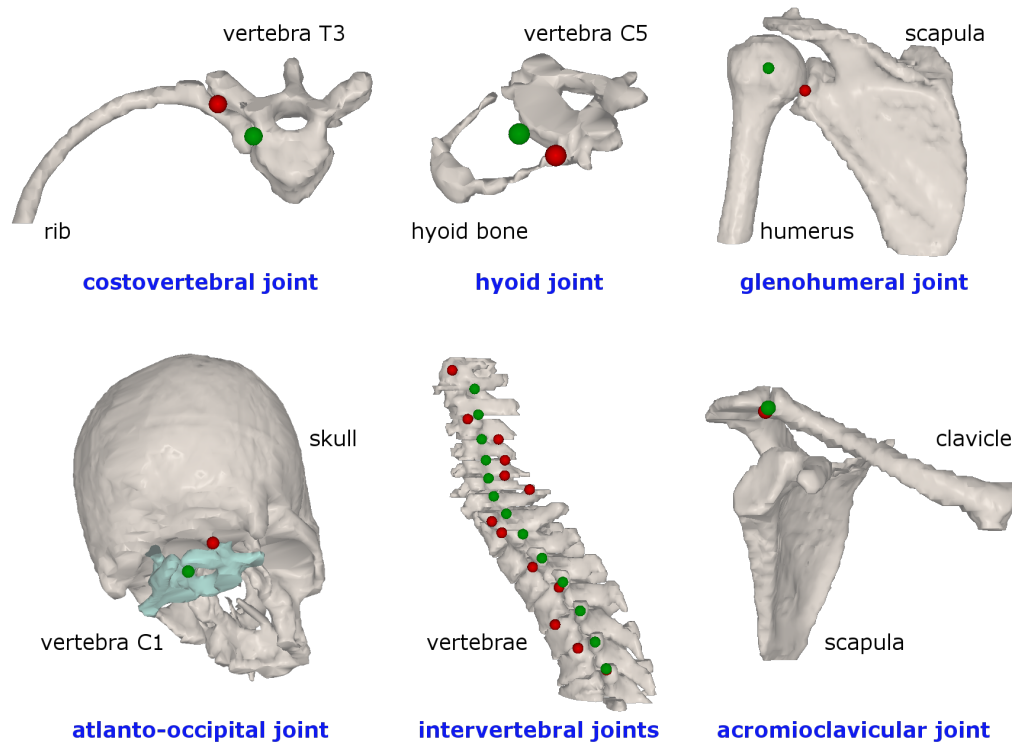

Figure 14: Exemplary positions of the rotation centres of different joints, determined according to the nearest neighbour approach (red) and the sophisticated approach involving custom positioning routines (green). The 1st cervical vertebra in the bottom left is highlighted in cyan for a better visual distinction of the boundaries to those of the skull.

Visual assessment reveals inappropriate positions of the joint rotation centres among all of the highlighted nine different joints. A nearest neighbour based positioning results in strongly deviating positions of the intervertebral joints, lying either in the centre of the vertebral body or at the posterior tip of the vertebra. Adjacent bones with multiple candidates for nearest distances dedicated to their shape could lead to deviating joint positions. This is especially the case for the costovertebral joint, the hyoid joint and the atlanto-occipital joint. For example the hyoid joint could be located on either the left or the right side, depending on the configuration of the anatomy at the time of image acquisition. Overall, a strong sensitivity of the delineation quality on the resulting joint positions seems to be given in case a simple nearest neighbour based approach is used. In contrast, the sophisticated joint positioning approach shows a weaker dependency on small variations in the delineated structures, leading to more centrally located joint positions for the hyoid joint, the atlanto-occipital joint and the intervertebral joints. Moreover,

custom positioning routines allow for determining more specific joint positions like the costovertebral joint and the glenohumeral joint. The position of the acromioclavicular joint shows no big difference between both approaches for this exemplary patient.

3.1.4   Kinematic motion behaviour

The use of the dependency graph of the bones and joints as shown in Figure 12 as a kinematic graph with a tree topology (described in section 2.8) requires some additional steps to be taken. First, the dependency graph is converted into a tree topology with a unique root element and without loops being present in the whole graph. The skull is chosen as the root element of the kinematic tree for the reason that it is usually immobilized in head and neck cancer radiation treatment. The generic dependency graph involves topological loops formed by the ribs, vertebrae and sternum as well as the mandible, which is connected to the skull via the left and right temporomandibular joints. In order to avoid kinematic loops, each bone is required to have a single unique predecessor bone. This is achieved by equally splitting up the representations of sternum and mandible into a fixed number of parts. This number equals the number of joints connecting predecessor bones prior the split, so that each split part of the sternum and each split part of the mandible uniquely connect to one predecessor bone. The sternum and the mandible are then replaced by their corresponding split parts, which were modelled as separate rigid bodies. To still maintain the rigidity of those bones as a whole, the individual parts are welded together using kinematic constraints, which inhibit any transformation between the split parts. Due to the relatively high computational effort involved for constraints, the minimal number of constraints required to weld all parts is automatically determined. Figure 15a shows the kinematic model with the joints and split parts of mandible and sternum, Figure 15b shows the resulting kinematic graph with a tree topology.

For the kinematic model of patient 1, the mandible is split into two parts, while the sternum is split into six distinct parts. A total of one kinematic constraint for the mandible and five kinematic constraints for the sternum are needed to preserve the rigidity of the assembled bones. Besides the modelled physiological joints, an additional virtual joint is added to connect the skull as the root element to an external frame of reference in order to allow for translation and rotation of the whole skeleton relative to the environment. The constructed head and neck kinematic model based on the image data of patient 1 (patient 2) incorporates 41 (38) bones, connected by 46 (47) physiological joints. This results in a total of 147 (150) DoF of the modelled skeleton, including the virtual joint and excluding the DoF removed by the use of kinematic constraints.

The underlying kinematic graph describes the relationship of the bones and joints to each other and allows for the description of the motion propagation across several joints according to kinematics. The *Simbody* toolkit (see section 2.8) is used to assist with the construction of the kinematic model and the solving of the inverse kinematic equations. A deformation of the skeletal anatomy can be described as the total of the local transformations of the individual bones associated to each corresponding voxel. Changes in the skeletal posture of the patient also involve a deformation of the soft tissue. The transformation of every individual bone of the skeleton is used to initialize a heterogeneous soft tissue model (Teske et al. 2017b). This way, a meaningful initialization for the calculation of the propagated deformation in the soft tissue surrounding the bones is guaranteed.
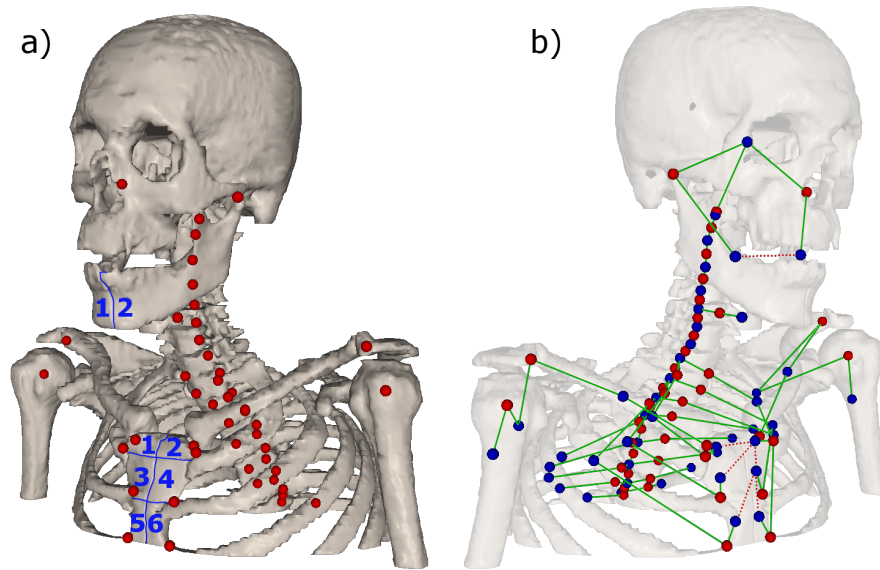
Figure 15: Illustration of the kinematic model of the exemplary patient 1 as a) the joint positions and split bones and b) the kinematic graph with a tree topology. Annotations highlight the positions of the joints (red spheres), the centres of mass of the bones (blue spheres) as well as the enumerated split parts of the mandible and sternum (blue numbers) with the associated kinematic constraints (dashed red lines) within the kinematic tree (green lines).

## 3.2 Evaluation of the kinematic model

Adaptive radiotherapy strongly relies on the assessment of deformations within the anatomy of the patient between planning and treatment fraction. An accurate and robust quantification of these anatomical changes is essential in order to guarantee an adequate adaptation of the treatment plan with the aim of a highly conformal and up-to-date treatment. Consequently, a thorough evaluation of the transformation model, as a key element in the assessment of deformations, needs to be carried out. Based on the assumption that variations in the skeletal posture of head and neck patients are the main reason for causing deformations in the whole anatomy, this section deals with the evaluation of accuracy and robustness of the kinematic model in mimicking various postures.

3.2.1 Reference transformations

Assessment of the accuracy and robustness of the developed kinematic model for the purpose of mimicking skeletal postures requires a good estimate of the true anatomical changes between treatment sessions and planning. Based on the image scans acquired during treatment planning and just before the treatment fractions, a gold-standard landmarks-based approach (see section 2.1.7) is used in order to extract a reference for the actually occurred deformations. For this evaluation, the image data of an exemplary patient undergoing small posture changes typically occurring during radiotherapy (patient 1) and the image data of one patient with large variations in the posture (patient 2) is taken into account. Details about the image data of both head and neck cancer patients can be found in section 2.3.

Salient feature points were defined on the planning CT image of patient 1 with a total of 185 features and on the PET-CT image of patient 2 with a total of 168 features, distributed over the whole skeleton on every bone covered by the FoV. The distribution of the features on the skeleton is shown in Figure 16 for both patients.
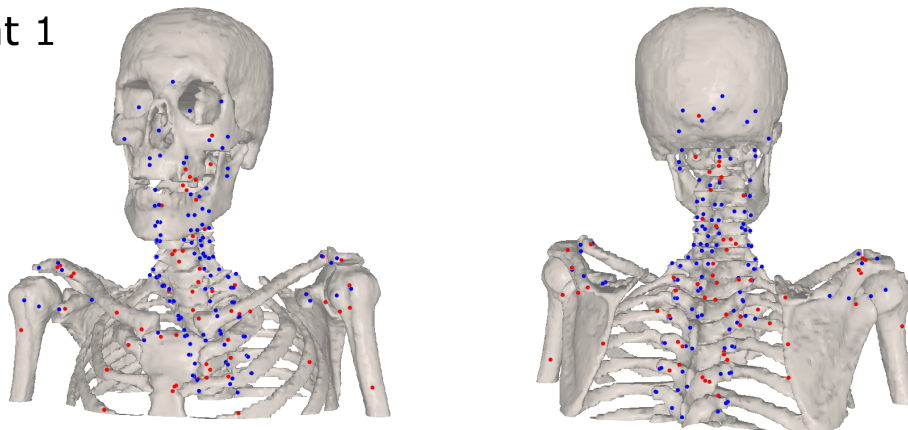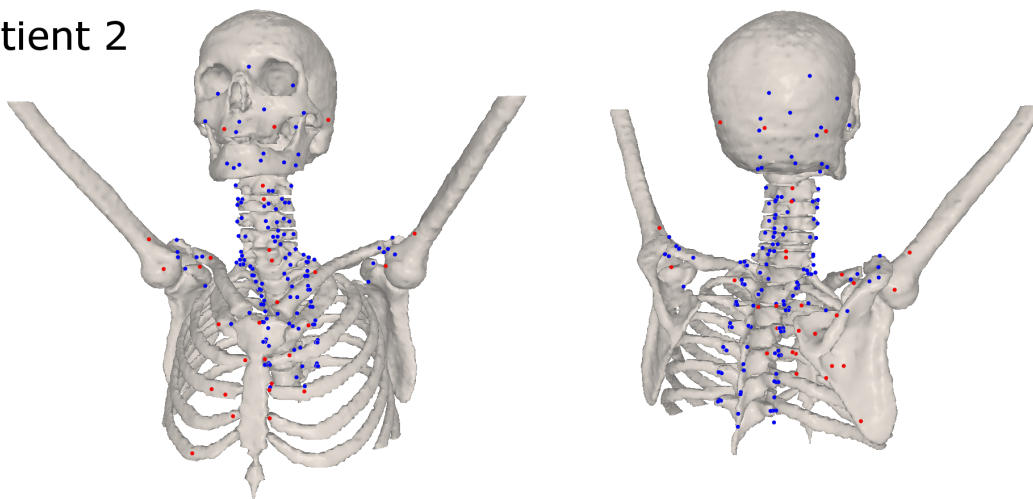
Figure 16: Overlay of the distribution of manually determined anatomical (blue points) and intensity-based (red points) feature points by one observer on the reference anatomy extracted from the image scans of patient 1 and patient 2. All feature points are located within the bony tissue.

The feature points are grouped into 125 anatomical feature points and 60 intensity-based feature points for patient 1 and 139 anatomical and 29 intensity-based feature points for patient 2, respectively. While the anatomical features like the distinctive processes of the vertebrae are generally shared by most patients, the intensity-based features, such as ossifications in the craniovertebral junction for example, are rather patient specific. Corresponding feature points found on the fraction image scans are referred to as corresponding points. The corresponding points of all the features on the reference image scans were then manually located and tagged by one to four expert observers on a subset of the fraction CT image scans for patient 1 and by one expert observer on the planning CT image scan for patient 2.

Tagging of these salient points in the images was done through manual placement of fiducial markers in either transversal, coronal or sagittal views using the *3D Slicer* (Fedorov et al. 2012) application. For patient 1, the subset of fraction image scans is comprised of the 1st, 2nd, 5th, 15th, 19th and the 28th fraction. Those fractions were chosen based on a visual assessment of the largest present changes in the skeletal anatomy throughout the treatment course. The expenditure of time for the manual task of pinpointing corresponding points accounted for about 4 hours per fraction per observer. Limited by the smaller FoV for the fraction images of patient 1 compared to the planning image, no corresponding feature points could be identified for the most caudally located 6th, 7th and 8th ribs and the 6th and 7th thoracic vertebrae. For patient 2, the feature points were defined from the skull reaching down to the 7th ribs and 7th vertebra. The pairs of feature points on the reference anatomy and the corresponding points on the changed anatomy at another time are referred to as landmarks.

After the manual identification of the landmarks, outliers were identified and excluded. A three-stage outlier detection approach was implemented. In the first stage, a rigidity criterion was imposed on all feature points that correspond to the same bone. The feature points responsible for a violation of the rigidity criterion were identified as follows:

For each bone, the distances of the feature points on the reference image scan were compared to the distances of the corresponding feature points on the image scans acquired at another point in time. Under the assumption that a rigid transformation of a bone does not induce changes to these measured distances, a threshold of 3.0 mm was imposed as a rigidity criterion on the difference of the measured distances among the reference and the corresponding feature points to account for deviations induced by interobserver variations. Those feature point positions contributing the most to these altered distances greater than the threshold were identified and excluded in further evaluation studies. In the second stage, an outlier criterion was defined among the feature points identified from the different observers in a leave-one-observer-out manner with the aim of detecting and eliminating those of the remaining feature points, whose position deviate from the positions defined by the other observers with a value larger than a certain threshold according to a three-sigma criterion. This threshold value is also determined empirically. In an iterative approach, for each feature point and each observer, the mean $\bar{p}_{other}$ and the standard deviation σ_{other} on the positions of one feature point across all other observers than the current is calculated. The distance d is calculated between the position defined by the current observer $p_{current}$ and $\bar{p}_{other}$. The position defined by each current observer is regarded to be an outlier if $\sigma_{other} > 2.0$ mm and $d > 3\sigma_{other}$ hold true. For the third stage, the standard deviation for each feature point across all observers is calculated. If it is larger than a fixed value of 2.0 mm, this feature point and all of its located positions are regarded as an outlier and were removed from the set of the remaining feature points. Results of the outlier detection are summarized in Table 2.

Table 2: Overview of the numbers of outliers found during the staged outlier detection.

	Outlier identification		
Fraction	stage 1	stage 2	stage 3
F02	12	2	0
F28	11	2	0

Between 11 and 12 of the defined corresponding feature points per fraction across all observers did not meet the rigidity criterion, imposed on the individual bones. Two

corresponding points for each fraction were excluded after the leave-one-observer-out test. The standard deviation of the individual feature points was less than the fixed threshold of 2.0 mm, hence no additional feature points were excluded in this stage.

3.2.2   Interobserver variation

Landmarks distributed on the bones of patient 1 and patient 2 are used as reference positions for the evaluation of the kinematic model by manually determining the positions of highly characteristic feature points on the skeletal anatomy. The landmarks obtained for patient 1 and patient 2 represent the changes of the anatomy between different points in time. Such a manual process of identifying and finding feature points in the different image scans is always prone to subjective influences of the observers, for example a different level of experience and anatomical knowledge. Other factors to consider are the degrees of clarity and ambiguity of the points. Some feature points are clearly visible within the images while for others, the anatomical region at that location is more blurred or distorted based on the underlying image quality. This is also affected by different window level settings for the visualization. The degree of ambiguity of the feature points is defined as the probability of inadvertently exchanging different feature points. These points considered, the dependency of the individual observer on the process of finding and identifying the feature points is measured by the quantification of the interobserver variation. For that purpose, a total of four observers were asked to find the corresponding feature points for patient 1 in the 2nd fraction and the 28th fraction. The same window level setting was used for all observers to reduce the impact on the clarity of the visualization.

Based on the resulting outlier-free set of corresponding feature points, the interobserver variation for every individual feature point per fraction is defined as the corrected sample standard deviation s over their spatial coordinates $p = [x, y, z]^T$ of every observer according to

$$s = \sqrt{\frac{1}{N-1} \sum_{i=1}^{N} (p_i - \overline{p})^2}$$

with N being the number of different observers. The mean interobserver variation per fraction is calculated by taking the mean of the interobserver variations of the individual feature points.

The mean interobserver variation for the 2nd fraction over all its feature points accounts for $[0.42, 0.38, 0.67]^T$ mm, ranging from a minimum of $[0.01, 0.03, 0.09]^T$ mm to a maximum of $[1.69, 1.20, 1.92]^T$ mm. For the 28th fraction, a mean of $[0.39, 0.43, 0.79]^T$ mm, minimum of $[0.05, 0.03, 0.06]^T$ mm and maximum of $[1.30, 1.38, 1.95]^T$ mm were found, respectively. The interobserver variation in the cranio-caudal z-direction is markedly higher than for the other directions. The distributions of the interobserver variations grouped by anatomical and intensity-based feature points is shown as a boxplot in Figure 17a for the 2nd fraction and in Figure 17b for the 28th fraction. While the box of the boxplot contains values ranging from the first to the third quartile, the whiskers reach out up to the minimum and maximum values. The median is indicated as a horizontal line located in the box. The same scheme is applied for all other bloxplots in this work. The anatomical and the intensity-based feature points show no noticeable difference regarding their interobserver variation.

The interobserver variations grouped by the individual bones, the feature points are assigned to, are illustrated in Figure 18. Feature points assigned to bones, which have
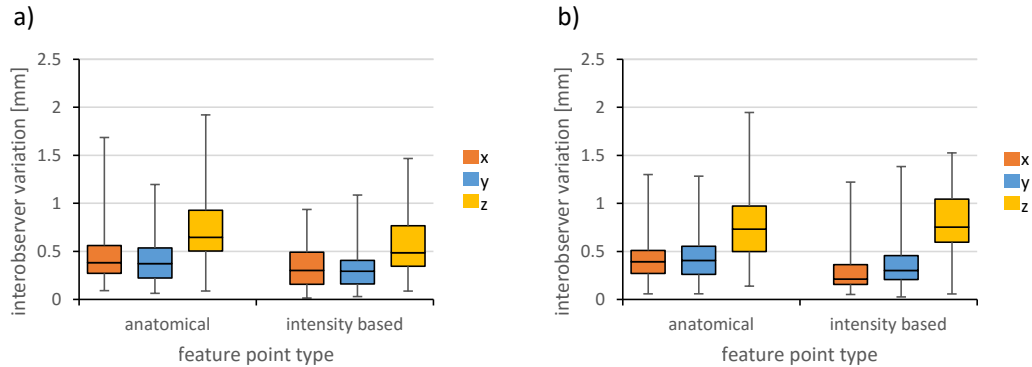
Figure 17: Resulting distributions of the interobserver variations grouped by anatomical and intensity-based feature point types for a) the 2nd fraction and b) the 28th fraction for patient 1 in x,y and z direction over all four observers.

multiple occurrences in the anatomy such as the scapula with the left scapula and the right scapula are aggregated. The same applies to multiple bones of the same type, such as the ribs and the vertebrae. The number of fiducial points associated to the grouped bones is additionally shown. The interobserver variation grouped by bones reveals no large differences among the different bones. For each individual bone, the interobserver variation along the z-axis is predominant.

The interobserver variation of the individual feature points is shown in Figure 19. Resulting 95% percentiles are slightly smaller for the intensity-based feature points with $[0.79, 0.67, 0.98]^T$ mm and $[0.72, 0.84, 1.38]^T$ mm compared to the anatomical feature points with $[0.88, 0.74, 1.32]^T$ mm and $[0.89, 1.0, 1.5]^T$ mm for the 2nd and 28th treatment fraction, respectively. This might indicate that intensity-based feature points are more characteristic and easier to identify by the human observers. The interobserver variation for all other treatment fractions is assumed to be within the same range as the resulting variations for the 2nd and 28th fraction.

a)

b)
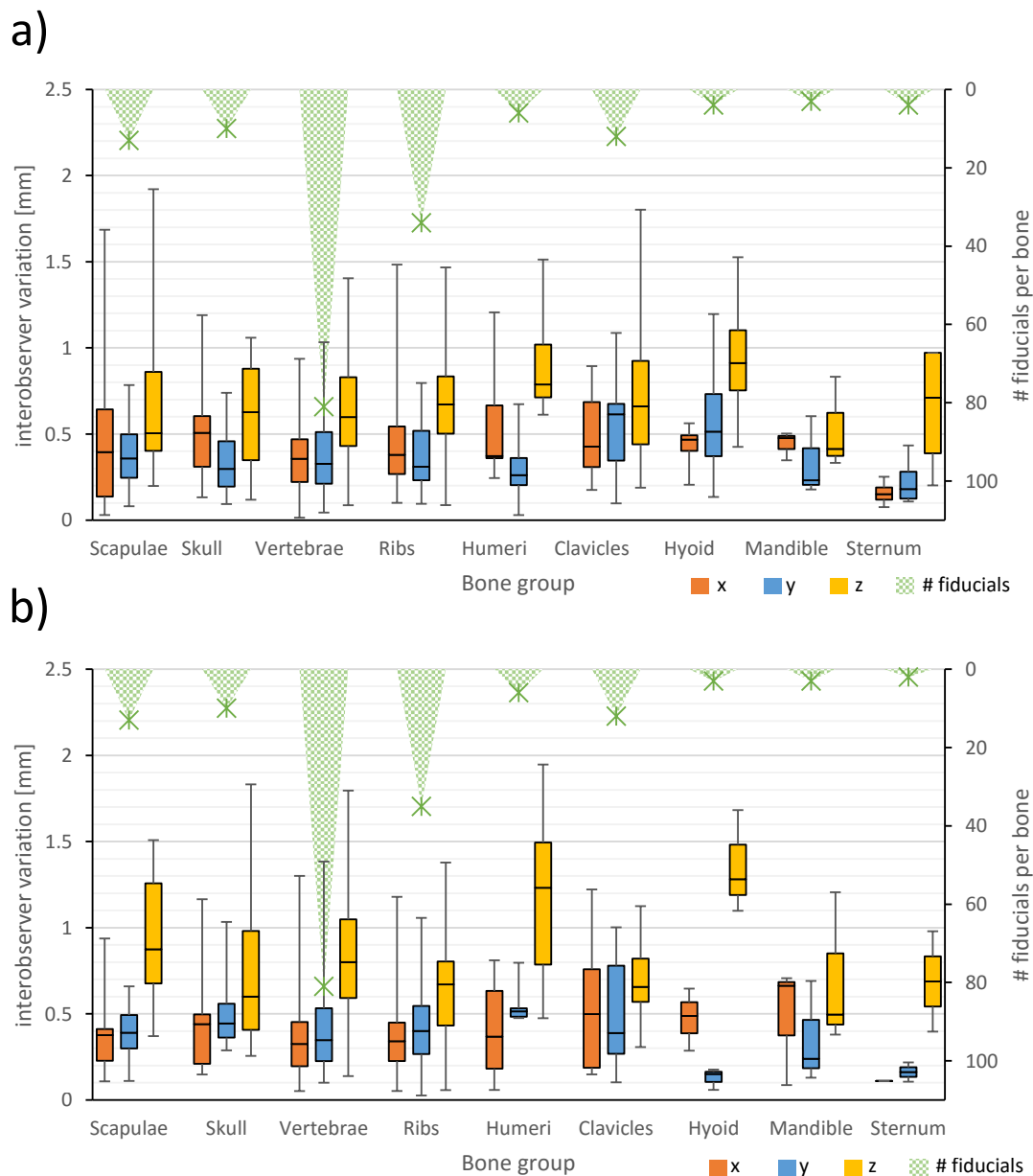
Figure 18: Resulting distributions of the interobserver variation grouped by the individual bone types for a) the 2nd fraction and b) the 28th fraction of patient 1. Bones with multiple occurrences like scapulae, ribs or vertebrae are aggregated. The number of fiducials set per bone group is shown on the inverted secondary y-axis in green color, respectively.
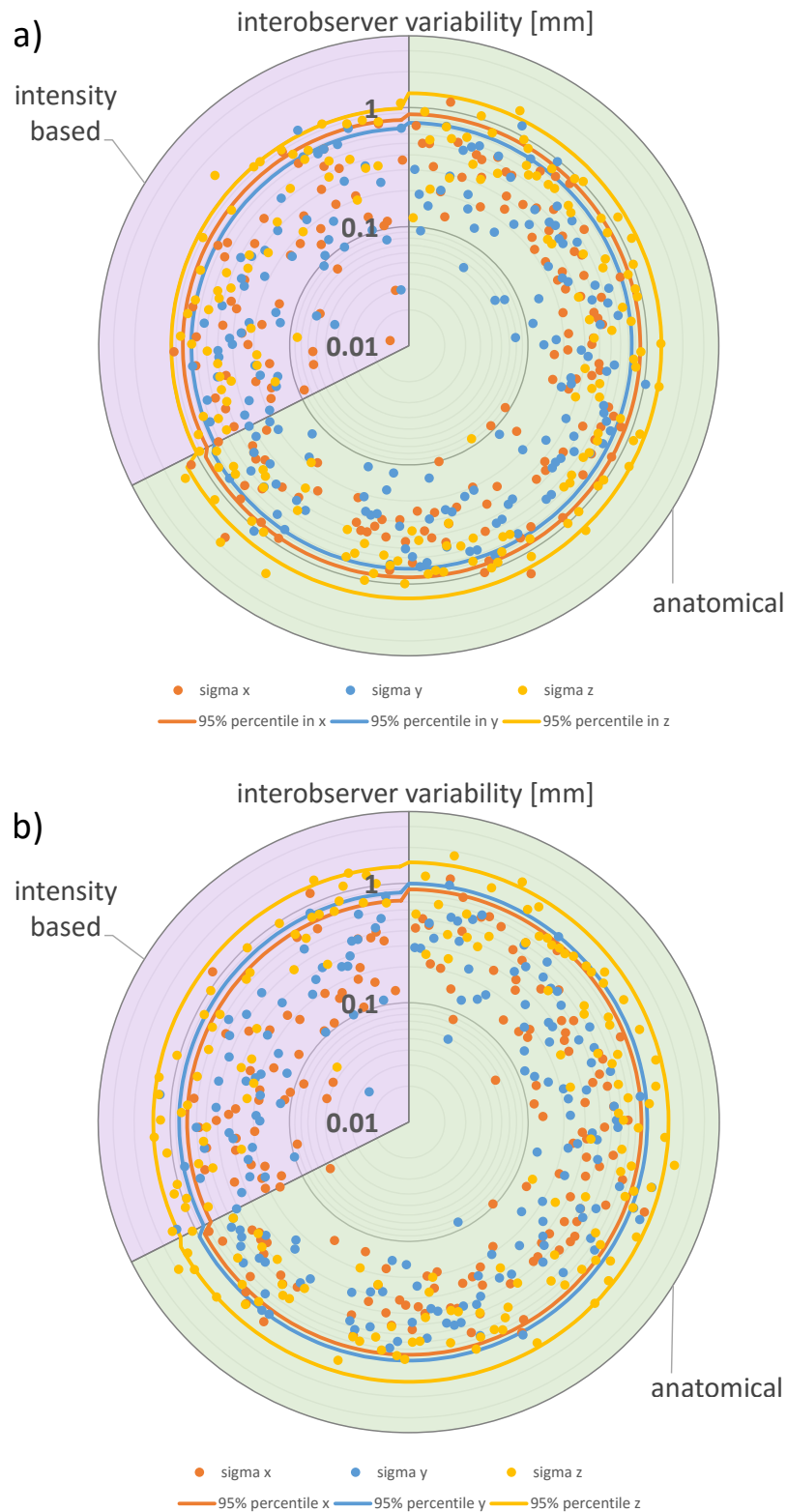
Figure 19: Distribution of the interobserver variation σ for each individual feature point as a radial plot for a) the 2nd and b) the 28th treatment fraction of patient 1. The points are arranged in groups of anatomical (green background) and intensity-based (light purple background) feature points. The 95% percentile is indicated as radial lines, grouped by those two feature point types. The interobserver variability is shown on an exponential scale.

3.2.3 Accuracy

As part of the evaluation of the kinematic model, its accuracy is assessed. It is quantified, how accurate the developed kinematic model based on the anatomy at the time of treatment planning is able to mimic the different postures of the patients occurring right before the treatment fractions. The quantification involves the datasets of patient 1, representing commonly occurring anatomical changes during the course of radiotherapy and patient 2, in which large changes in the skeletal posture occur. The sets of outlier-free landmarks obtained from the observers (as described in section 3.2.1) for both patients are used as the reference estimates of the true anatomical changes.

3.2.3.1 Feature point matching

While the feature points from the reference image scans represent the initial configuration of the skeleton, the corresponding points obtained from the image scans of the fractions are regarded as the reference for the skeletal configuration in these fractions, respectively. The same landmarks are used as an input for the kinematic model in order to mimic the skeletal postures of the fractions. To do so, each landmark is assigned to its corresponding bone of the skeleton by the smallest distance measured between the feature point defined in the reference image scan to the surface of each bone. Those feature points located in the very proximity of two different bones are assigned according to a lookup table, which was generated as a by-product during the initial definition of the feature points on the planning images. All landmarks corresponding to one bone describe the change in position and orientation of that bone between the planning image and the fraction image. As described in section 2.8, landmarks are converted to pairs of markers and observations used by the *Simbody* toolkit to define the desired transformations of the bones. In an optimization approach, the inverse kinematics problem is solved and the resulting posture of the whole skeleton is obtained.

The accuracy of such generated postures is denoted as the mean of the residual errors over all feature points. Residual errors on the feature points are calculated as the measured distance between positions of the observer-obtained corresponding points from the fractions and the positions of the feature points from the reference images transformed by the kinematic model as a result of the generated postures. In those cases, in which several sets of landmarks from different observers exist, one posture for each set of landmarks is generated and evaluated. This applies to the 2nd and 28th fraction of patient 1.

Accuracy over all fractions
For patient 1, the accuracy as the mean of the residual errors of the feature points achieved by the kinematic model in mimicking the true anatomical changes between planning CT and the 1st 2nd, 5th, 15th, 19th and 28th fraction CTs ranges from 0.78 mm to 1.23 mm, with a mean of 0.97 mm. The large anatomical changes in patient 2 are reproduced by the kinematic model with an accuracy of 1.22 mm. Figure 20 shows the distribution of the residual errors per fraction and observer.

While the scattering of the residuals for patient 1 given by the interquartile range (IQR) ranges from 0.41 mm to 0.81 mm, maximum errors of up to 3.87 mm for the 19th treatment fraction are observed. The IQR between the first and third quartile is illustrated as the height of the box in the boxplot shown. For patient 2, the IQR of 0.91 mm is slightly larger compared to patient 1 and the maximum error is considerably larger with a value of 6.96 mm.
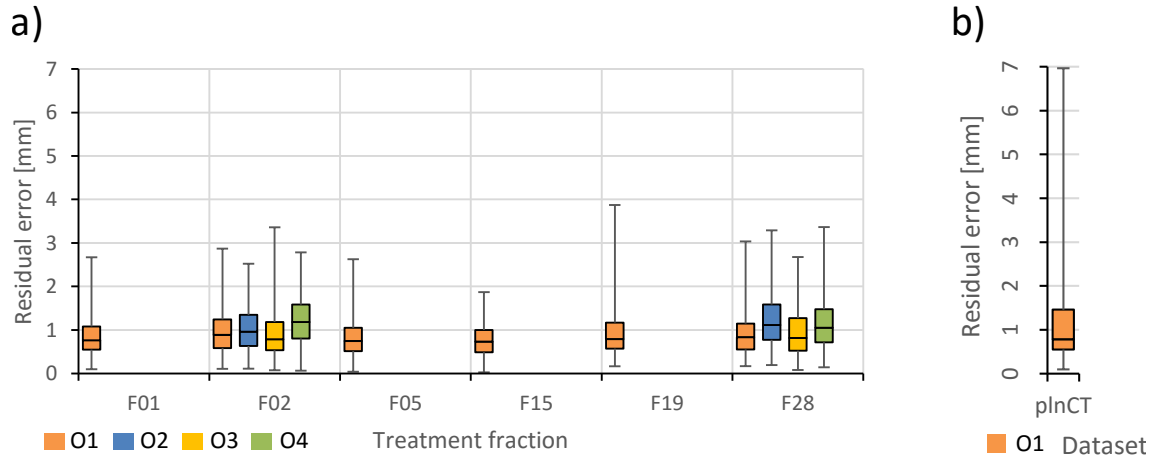
Figure 20: Distribution of the residual errors measured between the observer-defined corresponding feature points on the fraction image scans and the transformed feature points as a result of the kinematics based model of a) patient 1 and b) patient 2 for the four different observers (highlighted by different colors).

Accuracy grouped by bones

The residual errors of the feature points clustered by the bone groups, which they are assigned to, for both patients are shown in Figure 21. The 2nd treatment fraction of patient 1 was selected to be illustrative for all other fractions of the same patient. For patient 1, the median residual error averaged over the four different observers for each bone group accounts for a minimum of 0.70 mm for the humeri and for a maximum of 1.29 mm for the skull. The IQR averaged over the observers ranges from a minimum of 0.43 mm for the humeri, up to a maximum of 0.80 mm found for the skull. The largest of the maximum residual errors averaged over all observers are found for the skull and the vertebrae with 2.57 mm, while the smallest of the maximum residual errors accounts for 1.20 mm for the hyoid bone. For patient 2, the minimum of the median residual errors across all bone groups is found to be 0.43 mm for the hyoid bone. Accordingly, the maximum equals to 4.69 mm for the clavicles. The IQR ranges from a minimum of 0.16 mm for the hyoid bone, up to a maximum of 1.49 mm for the humeri. The largest mean residual error of 6.96 mm is found for the clavicles and the smallest maximum error accounts for 0.56 mm for the hyoid bone.
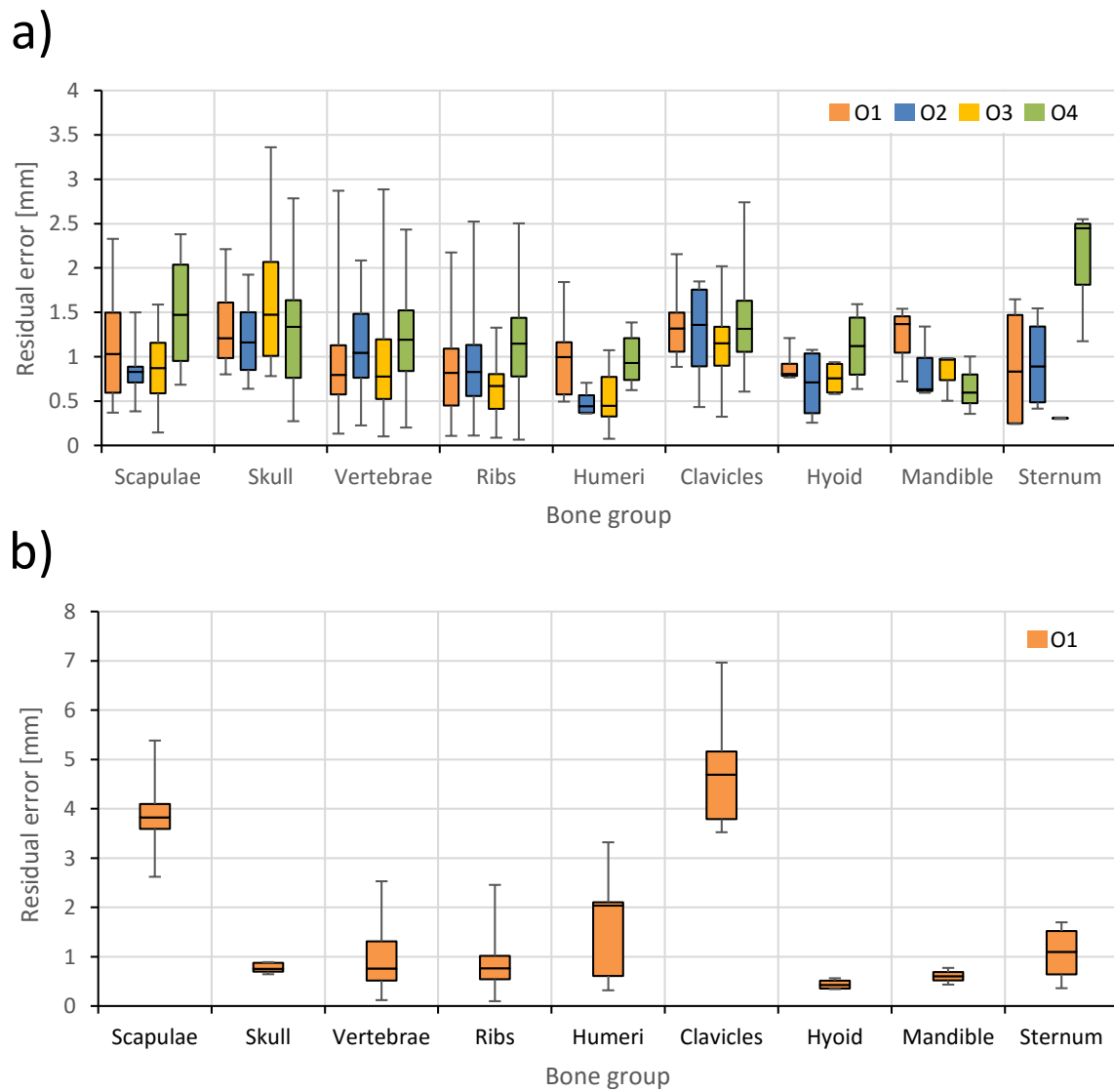
Figure 21: Boxplot showing the distribution of the residual errors of the feature points clustered according to the bone groups, they are located on, for a) patient 1 and b) patient 2. The residual errors with the different observers as reference are distinguished by the colors orange, blue, yellow and green.

Accuracy on individual landmarks

Figure 22 illustrates the distribution of the mean residual errors and the standard deviations per feature point including all fractions and observers, exemplary for patient 1. While the median of such mean residual errors equals to 0.94 mm, the median standard deviation accounts for 0.46 mm. It is observed that a few landmarks indicate a larger mean residual error and scatter range, for example the intensity-based feature point F533 and the anatomical feature point F6. The feature points are labelled in a way that anatomical features are enumerated from F1 to F125, while the intensity-based features range from F500 to F559.
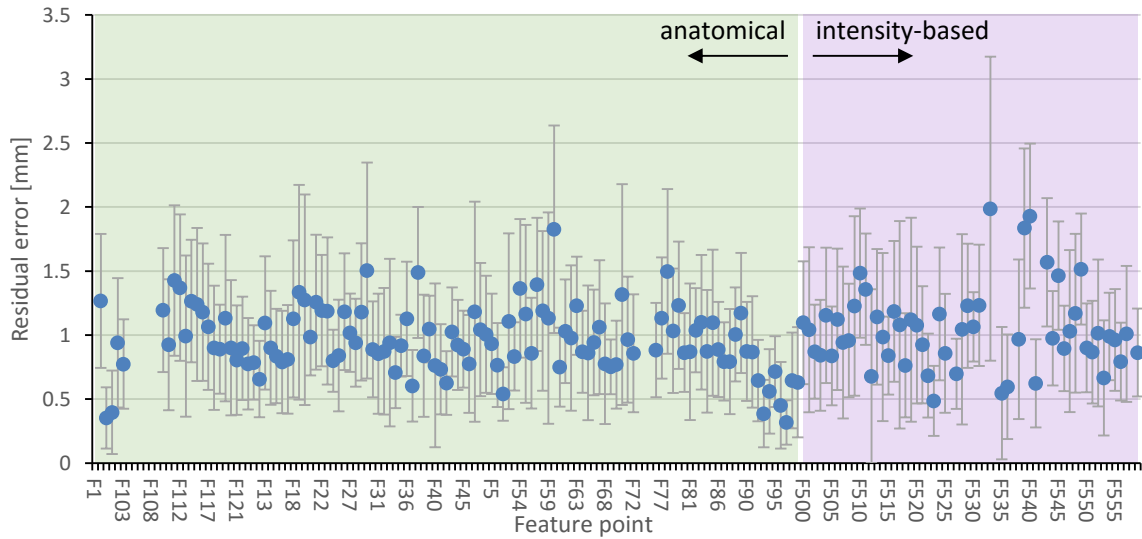
Figure 22: Resulting residual errors per feature point (blue points), averaged over all four observers including their corresponding standard deviation (whiskers). Anatomical feature points are highlighted with a green background and intensity-based feature points with a light purple background. The data shown corresponds to the 2nd fraction of patient 1.

3.2.3.2   Impact of joint positioning

For the quantification of the impact of the different joint positioning approaches as described in section 3.1.3 on the accuracy, two independent kinematic models were constructed. The first one had the joints positioned according to the nearest neighbour approach, while the second used the more sophisticated custom positioning approach. For both kinematic models, the same feature points of one exemplary observer, referred to as observer 1 in the previous studies, for patient 1 and patient 2 were used as an input to mimic the same postures across different treatment fractions. Both parametrizations of the kinematic models are compared in Figure 23 in regard of their achieved mean accuracy.

Averaged over all treatment fractions of patient 1, the resulting overall mean accuracy of 0.88 mm using the sophisticated joint positioning approach involving joint-specific positioning routines differs only marginally from the 0.90 mm achieved with the nearest-neighbour positioning approach. For patient 2, a larger difference can be observed between the overall mean accuracy of 1.65 mm for the nearest-neighbour approach and 1.22 mm for the sophisticated positioning approach, respectively.

Clustered by the different bone groups as shown in Figure 24, the largest difference in
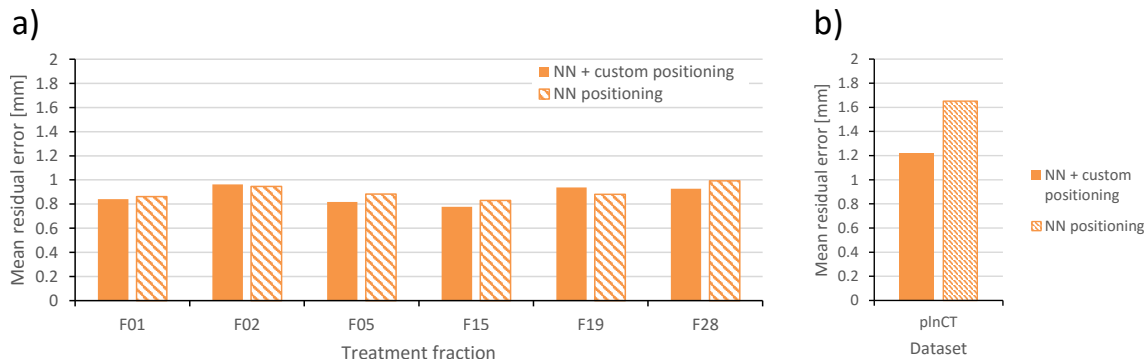
Figure 23: Comparison of the mean residual errors on all feature points for a) every treatment fraction of patient 1 and b) for the planning CT of patient 2 between two joint positioning approaches. The fully filled bars indicate the results for the nearest neighbour based positioning (NN) and the partially filled bars indicate the results for the approach using custom positioning routines for different bones.

the mean accuracy between both positioning approaches for patient 1 is found for the humeri with a difference of 0.52 mm, in favour of the sophisticated joint positioning approach. Also the accuracy of the scapulae shows a higher difference of 0.22 mm, respectively. For patient 2, the large anatomical change of the arms-up posture to the arms-down posture reveals even larger impacts of the different joint positioning approaches on the accuracy of the generated postures. Particularly in the shoulder area, large differences can be observed. The humeri, scapulae and clavicles achieve absolute improvements regarding their mean accuracies of 8.08 mm, 3.06 mm and 1.60 mm compared to the accuracies achieved with the nearest neighbour approach.

a)

b)
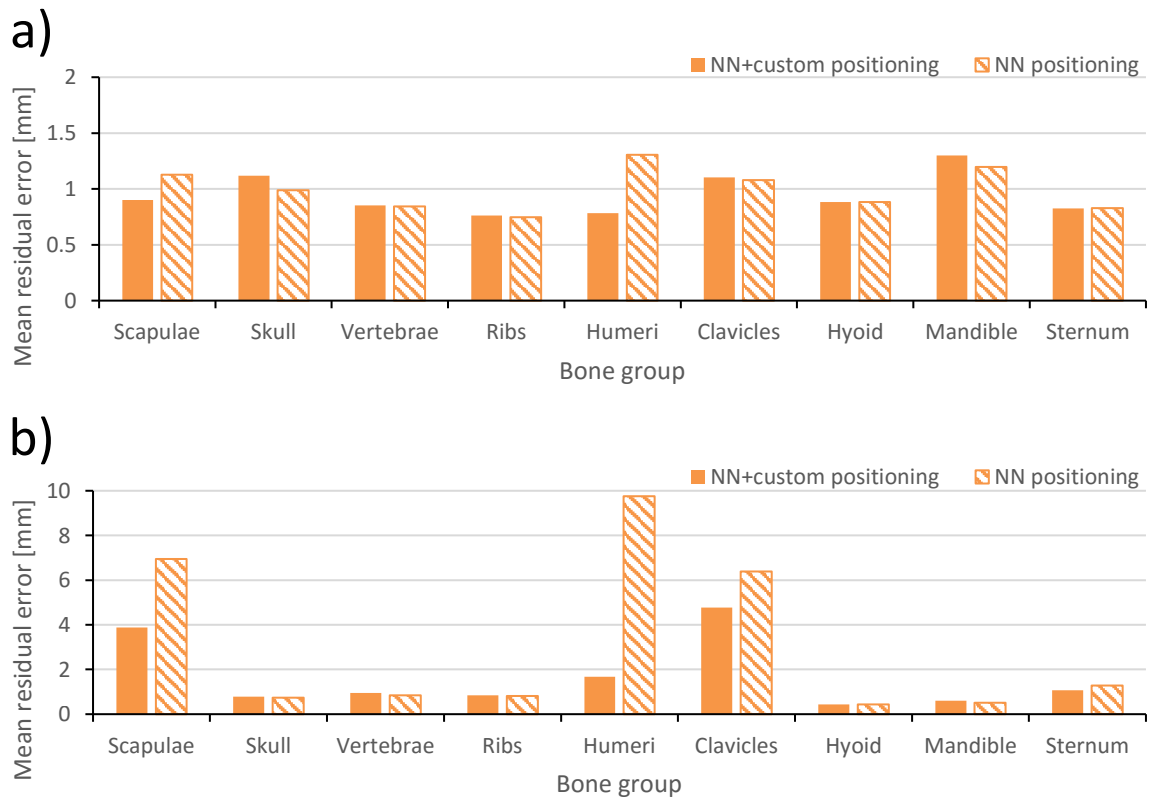
Figure 24: Comparison of the mean residual errors on all feature points clustered by the different bone groups for a) patient 1 averaged over all fractions and b) patient 2 between the two different joint positioning approaches. While the partially filled bars indicate the positioning approach using only nearest neighbour derived joint positions (NN), the fully filled bars indicate the additional use of joint specific positioning routines.

3.2.3.3 Impact of joint types

The impact of approximating all joints except the hyoid joint as 3 DoF ball-and-socket joints on the accuracy is evaluated by comparison with the same kinematic model, except for using 6 DoF joints instead. The increase in the DoF allows the joints to additionally translate about the three body axes. Analogously to the comparison of the two joint positioning approaches, the evaluation is performed on the same landmarks of an exemplary observer for both patients. As shown in Figure 25, the use of the 6 DoF joints results in an overall mean accuracy of 0.64 mm for all fractions of patient 1 compared to the 3 DoF joints resulting in 0.88 mm. A higher accuracy for the 6 DoF joints is consistently observed across all examined treatment fractions. For patient 2, the overall mean accuracy is 0.53 mm for the 6 DoF joints and 1.22 mm for the 3 DoF joints.

Figure 26 shows the results for the mean residual errors clustered by the bone groups. The largest differences in patient 1 are observed for the mandible and the sternum with an accuracy of 1.30 mm and 0.83 mm for the 3 DoF joints compared to 0.53 mm and 0.30 mm for the 6 DoF joints. For patient 2, the largest differences in the accuracy for the two joint types are shown for the clavicles, scapulae and humeri. For those bones, an accuracy of 4.78 mm, 3.89 mm and 1.68 mm is achieved with 3 DoF joints, while the accuracy is 1.17 mm, 0.63 mm and 0.43 mm respectively for the 6 DoF joints. For both patients and
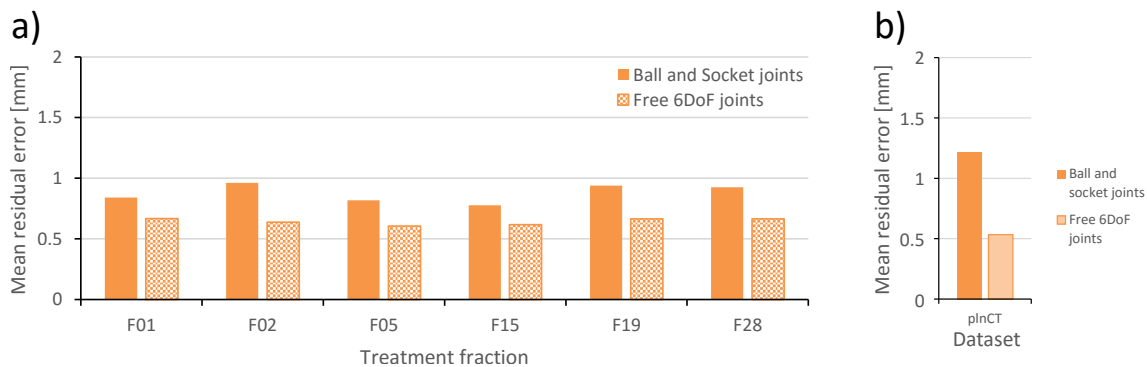
Figure 25: Comparison of the mean residual errors of all feature points in mimicking the skeletal postures of a) all examined fractions for patient 1 and b) the radiotherapy planning image scan for patient 2. Results of the 3 DoF joints are represented by fully filled bars and the results when using 6 DoF joints are represented by the partially filled bars, respectively.

every bone group, the use of 6 DoF joints results in an improvement of the mean accuracy.
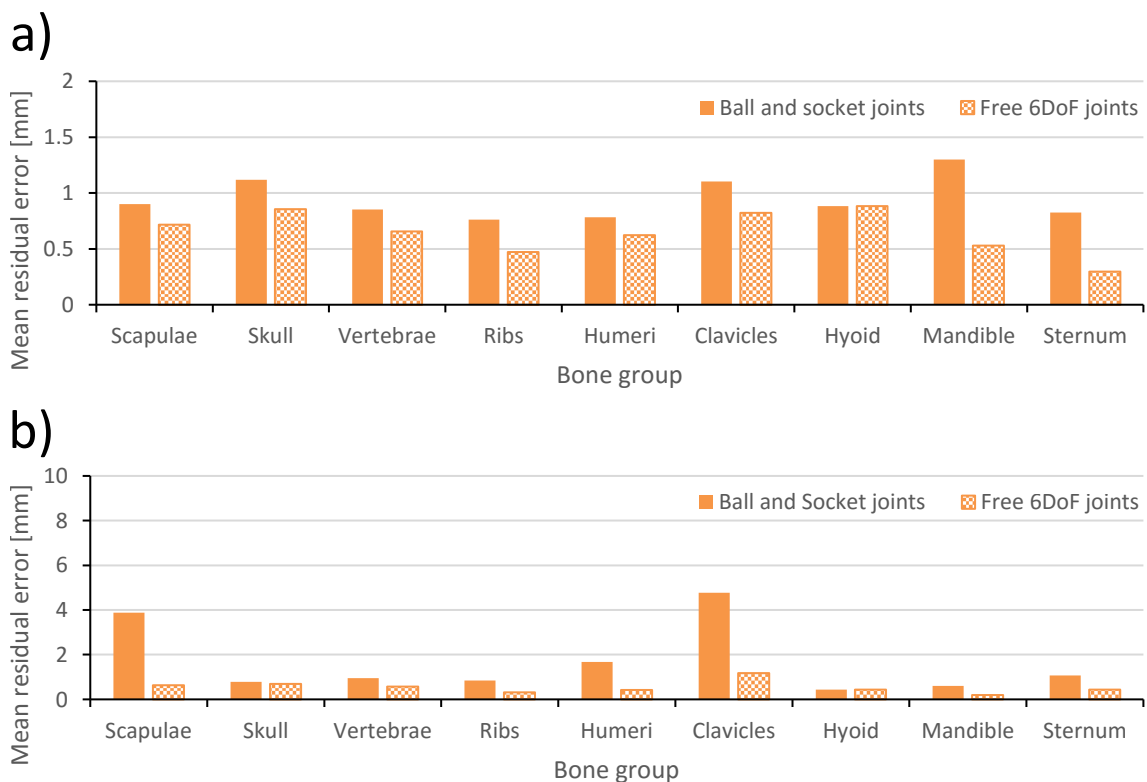
Figure 26: Resulting mean residual errors clustered by bone groups for reproducing skeletal postures by the kinematic models parametrized with either 3 DoF joints (fully filled bars) and 6 DoF joints (partially filled bars). Mean residual errors averaged over all examined fractions are shown for patient 1 in a) and results for the posture in the planning CT for patient 2 are shown in b) with a different scaling of the y-axis.

The impact of using 6 DoF free joints instead of 3 DoF ball-and-socket joints on the computation time needed for the kinematic model to simultaneously optimize the transformations of the rigid bodies based on all input landmarks is assessed. While the kinematic model with the 3 DoF joints requires ≈ 0.5 s on average to calculate the final posture, the use of 6 DoF joints consumes ≈ 3.9 s on average for the same task, which represents an increase by a factor of 7.8.

3.2.4 Robustness

Automated registration approaches for ART are guided by characteristic image information in both image scans subject to register. Biomechanical deformation models use this information as input to deform the patient anatomy in-silico. Besides the ability to accurately fit the modelled anatomy to the images, the robustness of the model against deficient input is an important quality. The evaluation of the robustness of the kinematic model for reproducing different postures encompasses a) the accuracy assessment of passively transformed bones, i.e. having no landmarks as a direct input, and b) the impact of wrong landmarks on the accuracy of the generated postures.

3.2.4.1 Leave-N-bones-out experiment

In contrast to using all landmarks distributed across all bones as input for the kinematic model for reproducing different postures, the robustness of the kinematic model is evaluated with only a subset of those landmarks as input to generate the same postures. The accuracy is then evaluated on those bones, which did not receive an input in form of landmarks. For that purpose, leave-N-bones-out experiments were performed in which N bones do not contribute to the set of input landmarks for the kinematic model, as described in Figure 27. As being representative, only the landmarks of one observer (observer 1) are included in this evaluation.
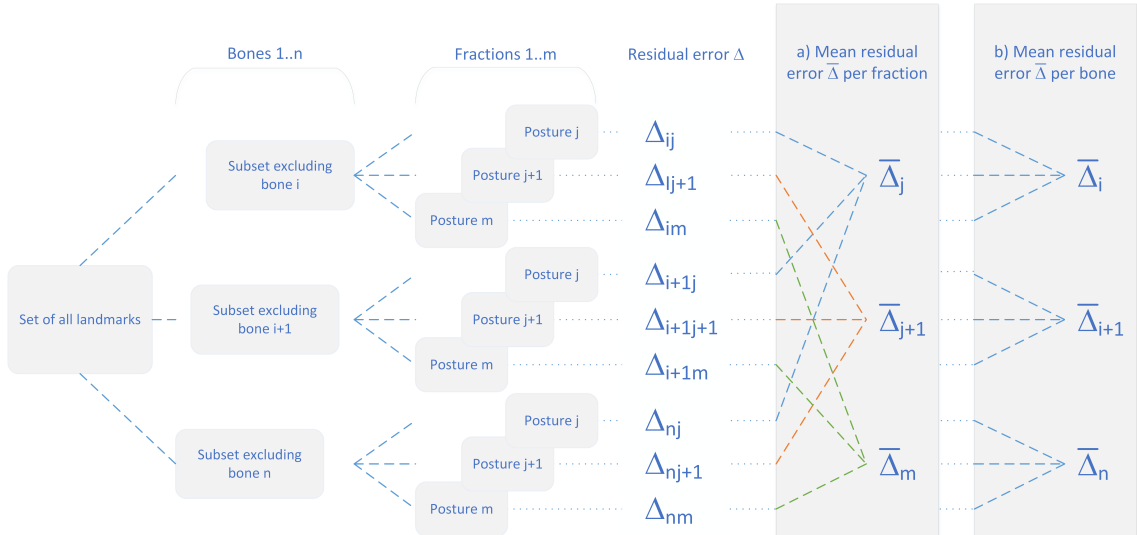

Figure 27: Schematic representation of the leave-N-bones-out experiment, exemplary for $N = 1$. Residual errors on the passively transformed bones, which did not receive input landmarks, after posture generation with the kinematic model are calculated and averaged a) per treatment fraction and b) per bone.

First, in a leave-one-bone-out experiment, the set containing all landmarks of all bones for each patient is divided into multiple subsets. The number of subsets equals the number of bones included in the kinematic model. Each subset contains all landmarks except those assigned to the bone, which is selected to be left out. Based on each subset, the landmarks are used as input for the kinematic model to reproduce the different postures of the 1st, 2nd, 5th, 15th, 19th and 28th fraction image of patient 1 and the arms-down posture change of patient 2. For each of the resulting generated postures per subset of landmarks, the residual errors on the feature points on the passively transformed bone, which did not receive landmarks as input, are calculated. The accuracy of the transformation of that bone is then calculated as the mean of those residual errors.

Analogous, a second leave-two-bones-out experiment is conducted. Instead of leaving out a single bone, a pair consisting of two connected bones is left out in each case. Hence, the number of subsets of landmarks equals the number of distinct pairs of two connected bones. If the landmarks of one bone are left out in two different subsets, the assessed mean residual errors of that bone per posture and subset are averaged in order to specify its accuracy.

Accuracy over all fractions

The accuracy of the kinematic model in reproducing postures measured on the passively transformed bones for both patient 1 and patient 2 is shown in Figure 28. Besides, the achieved accuracy when all landmarks are taken into account is shown for comparison.
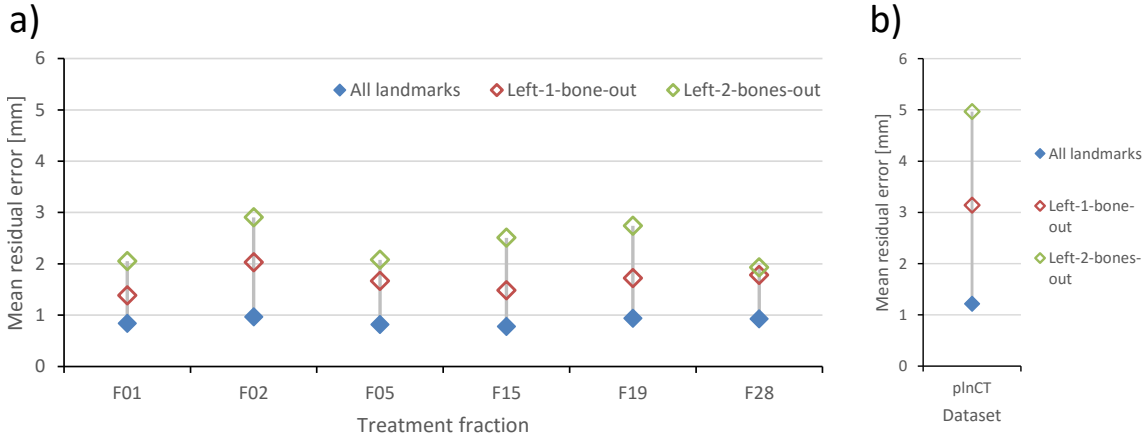
Figure 28: Resulting mean residual errors for a) all fractions of patient 1 and b) the planning CT of patient 2 for the leave-one-bone-out experiment (red) and leave-two-bones-out experiment (green) are compared to the mean residual errors (blue) when all landmarks are used. Only the residual errors for the feature points on those bones, which did not receive landmarks as input, are taken into account for the calculation of the residual errors for the leave-N-bones-out experiments.

For patient 1, the mean accuracy measured on all passively transformed bones in the leave-one-bone-out experiment ranges from 1.38 mm for the posture in the 1st fraction to 2.03 mm for the posture in the 2nd fraction. Compared to the case with all landmarks as input, this represents an increase in the mean residual errors of 0.54 mm to 1.07 mm, respectively. For the leave-two-bones-out experiment, the mean residual errors are higher for all treatment fractions and range from 1.93 mm for the 28th fraction up to a maximum of 2.90 mm for the 2nd fraction. On the one hand it can be observed that the overall

accuracy gets worse the more bones get passively transformed, i.e. have no landmarks as input, and on the other hand, the variance of the accuracy over the treatment fractions increases. For patient 2, the passively transformed bones achieve a mean residual error of 3.14 mm for the leave-one-bone-out experiment, a mean accuracy of 4.97 mm for the leave-two-bones-out experiment, compared to the mean accuracy for the case with all landmarks of 1.22 mm.

Accuracy grouped by bones
Figure 29 shows the resulting mean accuracies over all fractions achieved by the passively transformed bones grouped by the individual bones for both patients. For comparison, the mean accuracies of the case when all landmarks are used as input are also shown. As described in section 3.1, mandible and sternum are split into several parts, which are considered separately here.

Comparing the leave-one-bone-out results to the case with all landmarks, a few larger absolute differences in the mean accuracy per bone for patient 1 are found for the hyoid bone, both humeri and the scapulae with values of up to 4.09 mm. Having no landmarks defined for those bones results in mean residual errors of 4.98 mm for the hyoid bone, 3.89 mm and 3.21 mm for both humeri, 3.03 mm and 2.03 mm for the pair of scapulae. For the leave-two-bones-out experiment, overall larger residual errors are observed. Especially the accuracies of the left clavicle (Clavicle_L), one of the split parts of the mandible (Mandible_s2), the 3rd and 4th cervical vertebrae and the 6th and 7th thoracic vertebrae are decreased compared to the leave-one-bone-out experiment. The maximum of the mean residual errors can be found for the hyoid bone with 5.31 mm for the leave-two-bones-out experiment. Overall, it can be observed that the bones located far outboard in the kinematic tree like the skull, hyoid bone, humeri, mandible and 6th thoracic vertebra (Vertebra_T6) all come with relatively large residual errors when compared to the case where all landmarks are used as input. Regarding the accuracy in the area of the spinal column, it can be observed that leaving out individual cervical vertebrae has a stronger impact on the accuracy than leaving out thoracic vertebrae.

For patient 2, a similar magnitude of residual errors can be observed for most of the bones, compared to patient 1. The exceptions are both clavicles, both humeri and both scapulae, of which all exhibit markedly higher residual errors for the leave-one-bone-out experiment as well as for the leave-two-bones-out experiment. The largest of the mean residual errors can be found for the left and right humeri in the leave-one-bone-out experiment of 36.64 mm and 31.91 mm and in the leave-two-bones-out experiment of 41.12 mm and 35.69 mm, respectively. A considerable increase in the mean residual errors when leaving out the landmarks on pairs of two connected bones instead of only one bone can be observed in the left and right clavicles with values of 12.28 mm and 9.29 mm, the left and right scapulae with 17.59 mm and 7.56 mm and in the 4th and 5th vertebrae with 3.76 mm and 2.80 mm.
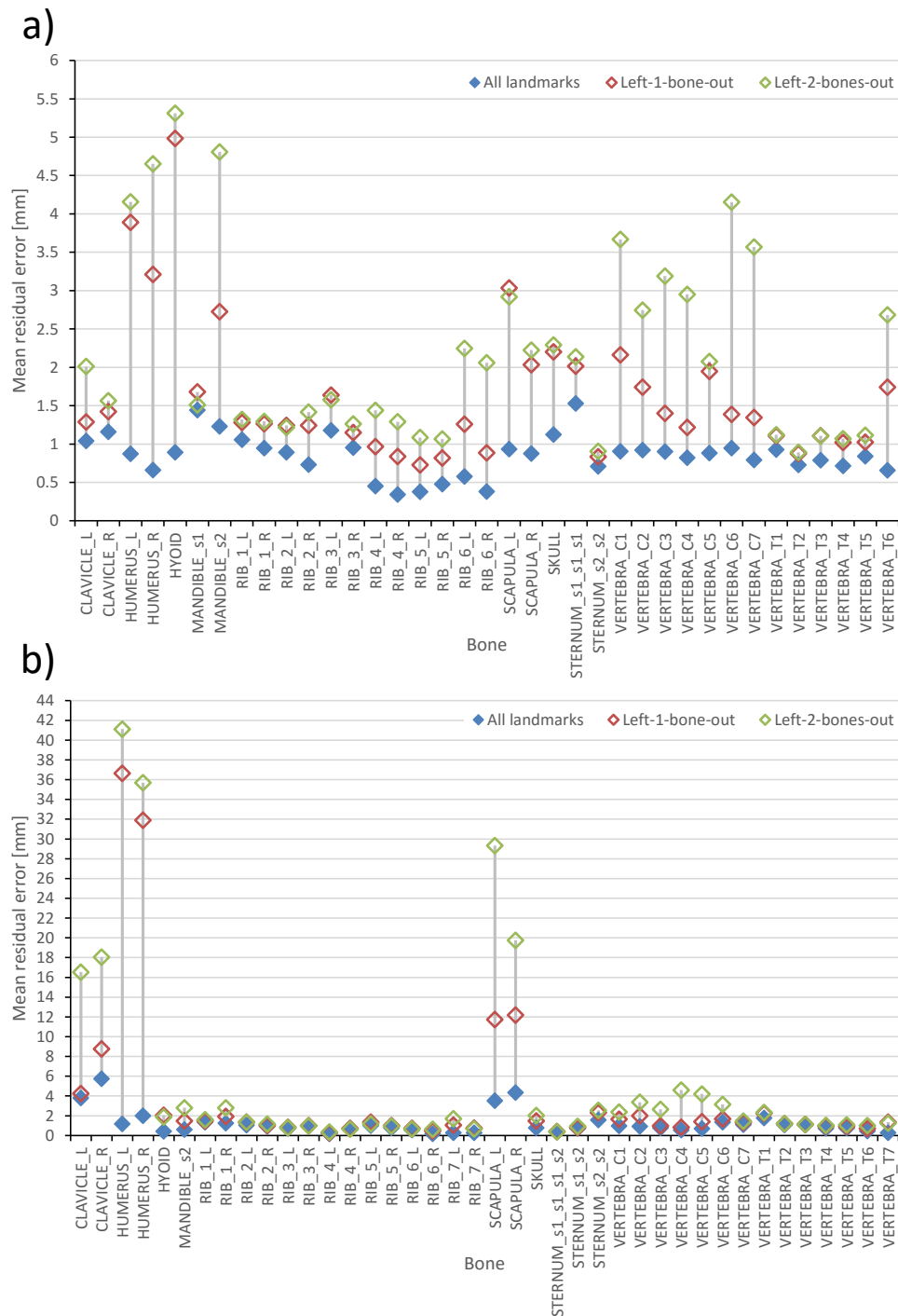
Figure 29: Achieved mean residual errors on the passively transformed bones during posture mimicking for the leave-one-bone-out experiment (red) and the leave-two-bones-out experiment (green) compared to the experiment with all landmarks (blue) are shown for a) patient 1 and b) patient 2. For patient 1, the residual errors are averaged over all examined treatment fractions. Multiple occurrences of the mandible and sternum are dedicated to the split parts of those bones, required during the construction of the kinematic model, and are labelled accordingly.

3.2.4.2 Wrong landmarks experiment

This part of the evaluation focuses on the robustness of the kinematic model when a subset of the input landmarks on the bones for the kinematic model provide wrong positions, which are in conflict with the observer-defined corresponding feature points used as reference. Based on the reference features obtained from one exemplary observer (observer 1), additional wrong landmarks were added to some of the bones. The impact of those wrong landmarks on the overall accuracy achieved by the kinematic model in reproducing the skeletal postures of both patients is quantified. For patient 1, the first treatment fraction was chosen as exemplary. The process of this wrong landmark evaluation is illustrated in Figure 30.
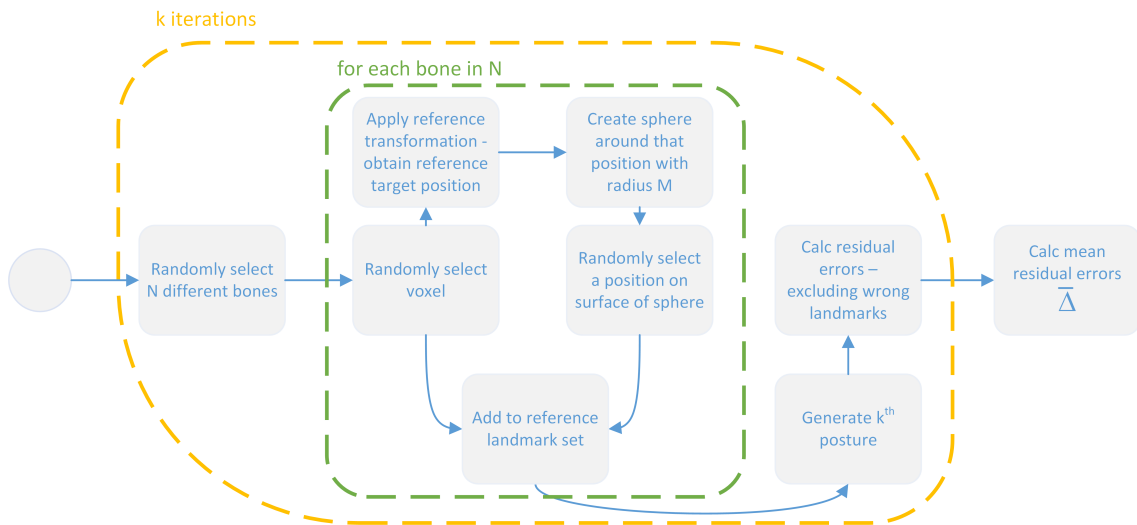
Figure 30: Illustration of the wrong landmark evaluation procedure. Iteratively, randomly selected wrong landmarks are positioned on the bones and are used together with the reference observer-defined landmark set as input for the kinematic model. The impact of those wrong landmarks on the achieved accuracy measured for the other bones is then quantified.

First, a number of N distinct bones of the skeleton are randomly selected, where N equals the number of wrong landmarks used in this experiment. For each of those bones, one voxel contained in the delineated volume of the bone is randomly selected to serve as the position of the wrong feature point on the reference anatomy. The reference transformation, obtained from exclusively using all landmarks of the observers as input for the model, for the particular bone is applied to the selected voxel. As a result, the reference target position of that voxel is obtained. Around this specific position, a sphere of radius M is created. All points belonging to the surface of that sphere deviate from the reference target position with a fixed value of M. One point is sampled uniformly from the surface of that sphere according to the method proposed by Marsaglia (1972) to represent the corresponding position of the wrong target feature. Together with the previously selected voxel position on the bone as the reference feature, a wrong landmark is created and added to the set of all landmarks. Having added all N wrong landmarks, the combined set of landmarks is then used as input for the kinematic model, resulting in a generated posture of the skeleton of the patient. Residual errors are only calculated for the reference landmarks obtained by the observers and do not include the wrong

landmarks. The whole process is repeated K times and the resulting residual errors of each iteration are averaged in order to obtain mean residual errors reflecting the impact of having N wrong landmarks distributed on the skeleton, of which the wrong corresponding features on the fractions deviate from the observer-defined position with a value of M. All randomly selected bones and voxels as described above are sampled from distinct uniform distributions. Those bones which do not already have any observer-defined landmarks were excluded from the evaluation.

A total of five experiments with different parametrizations are performed. The number of iterations K is set to $K = 500$ for each case. In three experiments, a constant violation value, i.e. the deviation of the position of the wrong corresponding feature point to the observer-defined reference target position, of $M = 5$ mm is used, while a different number of wrong landmarks $N = 1$, $N = 3$ and $N = 5$ was used. For the remaining two experiments, N is consistently set to $N = 5$, while M is set to $M = 10$ mm and $M = 15$ mm, respectively. The impact of the wrong landmarks on the accuracy of the reproduced postures of patient 1 and patient 2 compared to exclusively using the reference landmarks obtained from the observers as input for the kinematic model is quantified. Accordingly, the resulting differences of the achieved residual errors are calculated. This is done by subtracting the residual errors as a result of using only the reference landmarks from the residual errors of the experiments when the additional wrong landmarks are included. Hence, differences with a positive sign indicate an increase in the residual errors, thus a deterioration of the accuracy as a result of the included wrong landmarks. Accordingly, differences with a negative sign mean lesser residual errors or an improved accuracy. Figure 31 shows the distribution of the resulting overall mean differences, i.e. the mean difference measured for all the bones of the skeleton of a patient, over all K iterations for the five experiments.
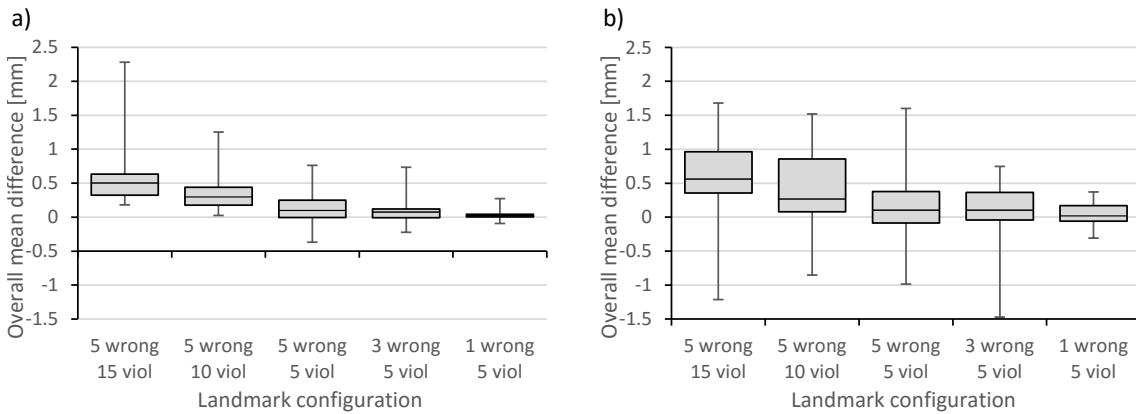
Figure 31: Boxplot showing the mean differences in residual errors achieved by the kinematic model using exclusively the observer-defined landmarks subtracted from the results obtained from the experiment with additional wrong landmarks. The mean differences are averaged over all used feature points and all bones for a) patient 1 and b) patient 2. Different landmark configurations consisting of a varying number of wrong landmarks used as well as different violation values are used.

Under a consistent violation value M of 5 mm for the wrong landmarks, an increase in the number of wrong landmarks N results for both patients in an increase of the differences, which means an increase in the mean residual errors. Similarly, an increase

in the violation value from 5 mm to 10 mm to 15 mm for five wrong landmarks in all cases leads to increased overall mean residual errors. For both patients, differences with a negative sign indicate that for some of the 500 iterations, the wrong landmarks result in a decrease of the mean residual errors of the posture.

Between the one, three and five wrong landmarks for patient 1, the median of the mean differences in the overall residual errors varies from 0.02 mm to 0.10 mm. Using different violation values results in a median difference in overall residual errors ranging from 0.10 mm to 0.50 mm. A maximum overall difference of 2.28 mm can be observed for the experiment with five wrong landmarks and a violation value of 15 mm. For the same configuration, 95% of all generated postures result in an increase of the mean residual error for the whole posture of ≤ 1.32 mm. The IQRs increase from the configuration of one to three to five wrong landmarks from 0.04 mm to 0.13 mm to 0.26 mm, respectively. Regarding the violation value of 5 mm, 10 mm and 15 mm, the IQRs marginally increase from 0.26 mm to 0.26 mm to 0.31 mm.

For patient 2 with large anatomical changes present, the increase in the number of wrong landmarks results in median differences ranging from 0.02 mm to 0.10 mm. The increase in the violation value results in differences ranging from 0.10 mm to 0.56 mm. A maximum deterioration of the accuracy of 1.68 mm is observed for five wrong landmarks and a violation value of 15 mm. In 95% of the cases, mean residual errors are not increased by more than 1.40 mm. IQRs of 0.22 mm, 0.40 mm and 0.46 mm are observed for one, three and five wrong landmarks. For violation values of 5 mm, 10 mm and 15 mm, the IQRs equal to 0.46 mm, 0.78 mm and 0.61 mm, respectively.

Impact of the number of wrong landmarks
The impact of the number of wrong landmarks N involved in reproducing the postures is shown in Figure 32 on a per-bone basis for both patients over a total of 500 generated postures.
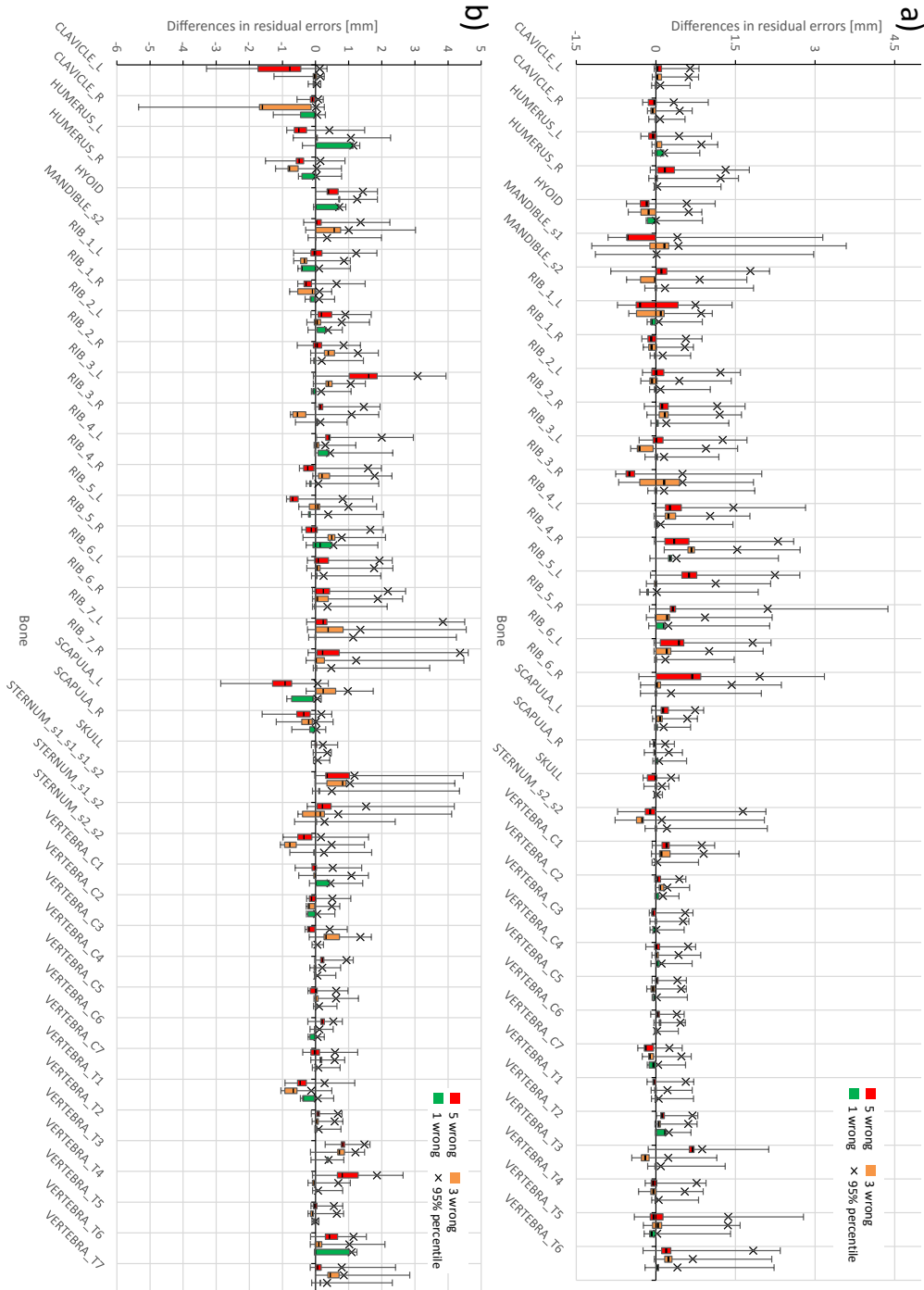
Figure 32: Differences in the residual errors achieved by the kinematic model as a result of additionally including a different number of wrong landmarks as input compared to only using the observer-defined reference landmark set. The differences are shown for the wrong landmark configurations with one (green), three (orange) and five (red) wrong landmarks with a consistent violation value of 5 mm for each bone involved over 500 generated postures for a) patient 1 averaged over all fractions and b) patient 2.

For patient 1, overall, small increases in the residual errors when including wrong landmarks compared to using only the reference landmarks obtained from the observers are shown across all the bones for most of the postures generated. Among each configuration of one, three and five wrong landmarks with a fixed violation value of 5 mm, the third quartile of the differences per bone does not exceed 0.84 mm. That means no considerable impact on the accuracy of the kinematic model can be observed for a majority of the generated postures. The spread of the distributions of the differences measured for each bone varies depending on the specific bone. While the cervical vertebrae show small variations of the differences, the ribs show a larger sensitivity to including additional wrong landmarks on any bone of the skeleton. The right 5th rib shows the largest maximum increase of the residual errors of 4.37 mm. Variation in the number of wrong landmarks does not result in considerable differences on the residual errors of the bones. The mean IQRs for one, three and five wrong landmarks equals to 0.05 mm, 0.16 mm and 0.21 mm. A maximum 95% percentile of 2.30 mm is found for the right 4th rib with five wrong landmarks included. Mean 95% percentiles across all bones equal to 0.12 mm, 0.69 mm and 0.98 mm for one, three and five wrong landmarks.

Similar characteristics are observed for patient 2. For 75% of the generated postures, the residual errors of the individual bones do not increase more than 1.86 mm. The spread of the distributions of the differences in the residual errors measured for every bone is also dependent on the specific bone. In accordance with the results for patient 1, a larger spread is observed for the ribs, especially the 7th ribs, and the sternum while the spread for the cervical vertebrae remains relatively small. The largest increase in the residual errors is found for the right 7th rib with a value of 4.61 mm. A maximum 95% percentile of 4.36 mm can be found for the same rib with five wrong landmarks, whereas the mean 95% percentile across all bones equals to 1.11 mm, 0.79 mm and 0.28 mm for five, three and one wrong landmarks, respectively. Mean IQRs of 0.20 mm, 0.30 mm and 0.33 mm can be found for one, three and five wrong landmarks. However for both patients, some of the postures also yield smaller residual errors than without the additional wrong landmarks, finding a maximum increase of the accuracy in the right clavicle of 5.34 mm for one out of the 500 generated postures.

Impact of the violation value
Variation of the violation value M of the wrong landmarks affecting the accuracy measured on the different bones is illustrated in Figure 33 for both patients over a total of 500 generated postures.
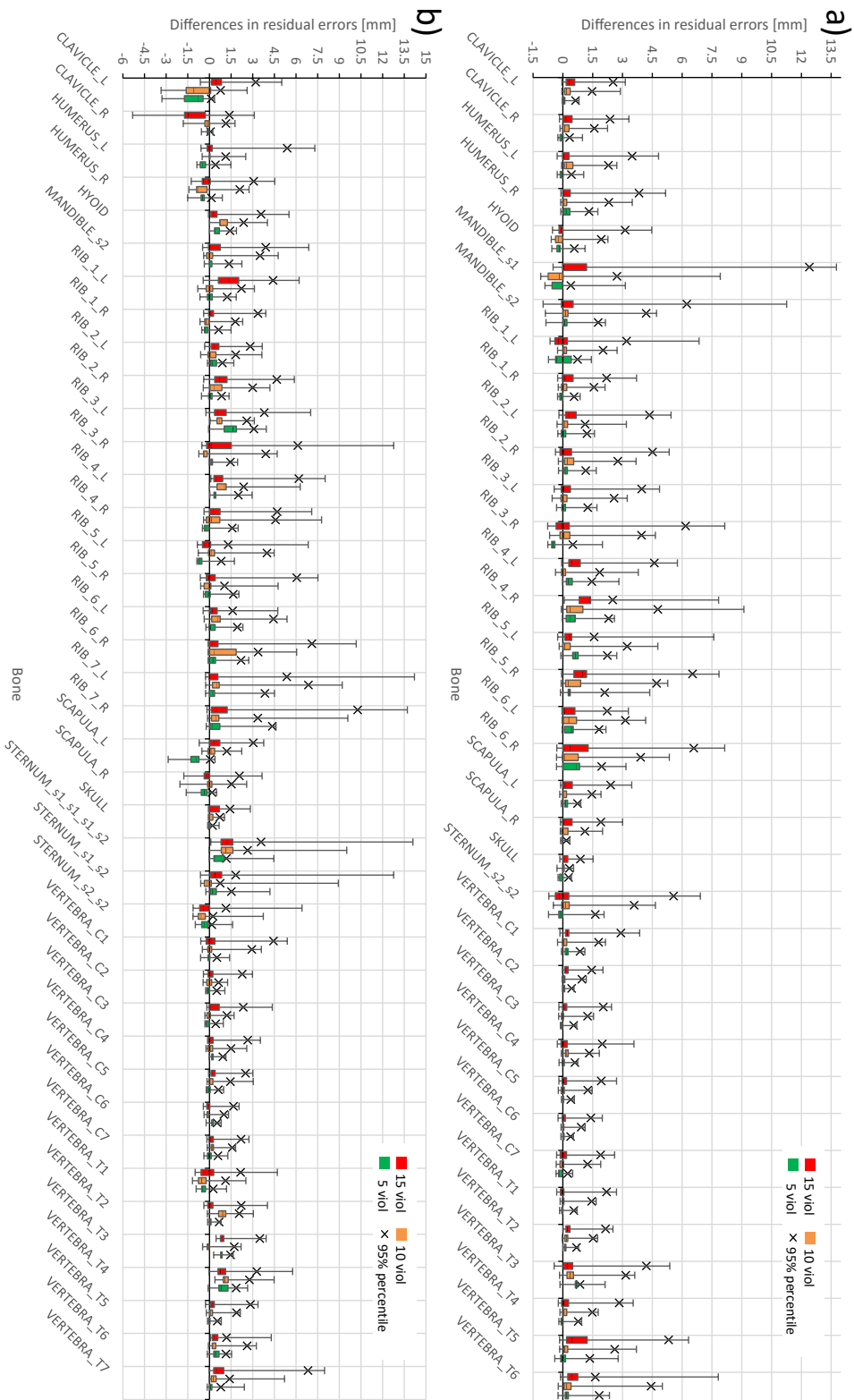
Figure 33: Differences in the residual errors achieved by the kinematic model as a result of using a varying violation value of 5 mm (green), 10 mm (orange) and 15 mm (red) of five wrong landmarks as input for the kinematic model compared to using only the observer-defined reference landmarks. The distribution of the differences are shown for each bone over a total of 500 generated postures for a) patient 1 averaged over all fractions and b) patient 2.

Variation of the violation value for patient 1 leads to small changes in the residual errors per bone for most of the generated postures. As a result of increasing the violation values from 5 mm to 10 mm to 15 mm, the widths of the distributions of the differences per bone increase as well. The third quartile for each bone in each of the three configurations does not exceed 1.40 mm. That means, that even including wrong landmarks, which deviate with a value of up to 15 mm from the true target position, a relatively small impact on the residual errors of the bones is observed. The maximum change in the residual errors can be observed for the first split part of the mandible (Mandible_s1) with a value of 13.77 mm for the configuration of using five wrong landmarks with a violation value of 15 mm. Especially the cervical spinal area shows small spreads of the distributions of the differences in the residual errors. Larger spreads are found for the mandible, the ribs and the sternum. The mean IQRs range from 0.21 mm to 0.32 mm to 0.47 mm for violation values of 5 mm, 10 mm and 15 mm. The average 95% percentiles range from 0.98 mm to 2.28 mm to 3.48 mm, respectively. A maximum 95% percentile of 12.41 mm can be found for a split part of the mandible (Mandible_s1) with five wrong landmarks deviating with a value of 15 mm. The evaluation for patient 2 reveals similar results. The third quartile for each bone in each configuration does not exceed 2.02 mm. The maximum difference in the residual errors can be found for the left 7th rib with a value of 14.2 mm. Spreads in the distributions of the differences show similar characteristics as for patient 1. The differences for the mandible are not as peculiar as for the mandible in patient 1. The mean IQRs equal to 0.33 mm, 0.48 mm and 0.63 mm for violation values of 5 mm, 10 mm and 15 mm. The average 95% percentiles equal to 1.11 mm, 2.18 mm and 3.54 mm, respectively. The largest 95% percentile among the bones is found with 10.26 mm for the right 7th rib, in the experiment with five wrong landmarks and a violation value of 15 mm.

3.3   Posture generation

The implementation of a plan-of-the-day concept relies on a priorly generated plan library in order to cover most commonly occurring anatomical variations for a specific area (see section 2.1.4.4). In this context, the developed biomechanical model can be used to forward simulate different postures of the patient (Teske et al. 2017b). As a reference, the anatomy of the patient at the time of treatment planning is extracted as the 3D static anatomy and further articulated based on kinematics as described in section 3.1. Based on that, different postures of the same patient are simulated as follows: Arbitrary transformations of the individual bones can be induced either by interactive manipulation or by importing predefined pairs of corresponding feature points. For the interactive control, a graphical user interface was designed to enable the user to directly alter the positions and orientations of any bone directly in a 3D rendering scene, as shown in Figure 34. Furthermore, an efficient DVF visualization technique (Meis et al. 2017) allows for the immediate visual extent of the generated posture.

For each interactively altered transformation of a bone, the input of the user is internally mapped to pairs consisting of a marker position and an observation position (see section 2.8) on the bone, which was the target of interaction. Those points fully describe the change in position and orientation of the bone. Further, in a L-BFGS optimization method provided by *Simbody*, the best possible fit of the articulated skeleton to the set of these input points is found. By inverse kinematics calculation, the angles of all the joints defined in the kinematic model and thus the transformations of the remaining bones are obtained in an interactive time frame. It is up to the user to decide how many bones
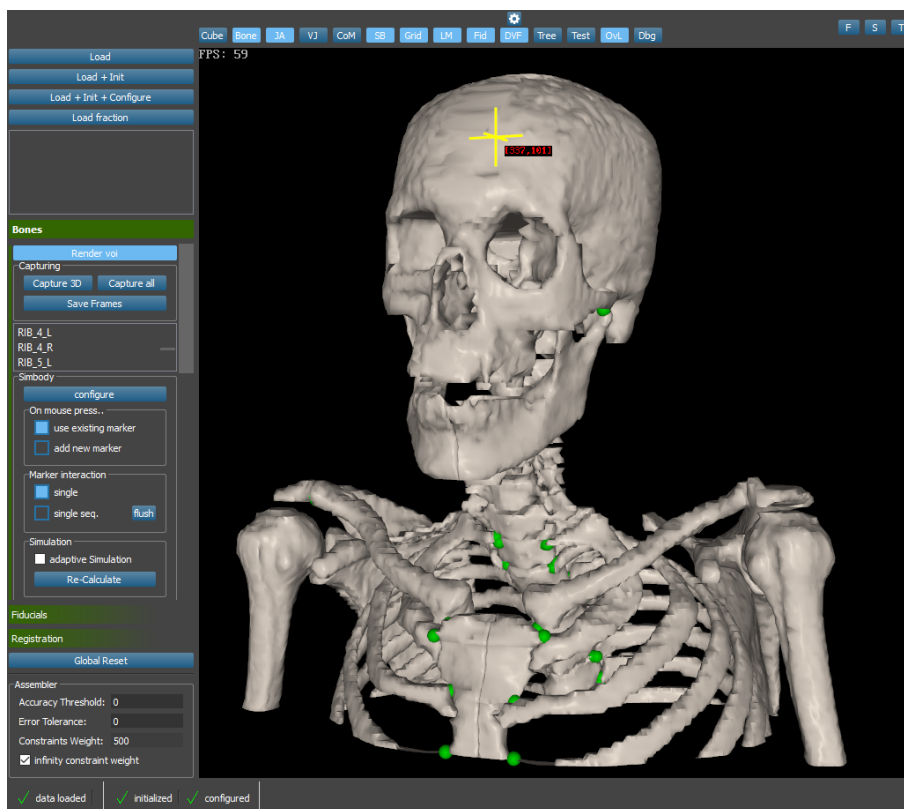
Figure 34: Snapshot taken from the graphical user interface of the designed application, providing the functionality to interactively forward-simulate various postures of a loaded patient. The 3D rendering scene represents the current skeletal anatomy of exemplary patient 1, and the currently used joint positions as green spheres. The yellow cross-hair indicates the current position of the computer mouse, which defines the point of interaction with the represented anatomy. By clicking and dragging, the bones are interactively transformed while the transformations of all other bones are calculated on-the-fly via inverse kinematics. The different settings for the posture simulation and further functionalities can be found on the left side of the snapshot.

should receive an alteration of their transformations to control the overall posture of the skeleton. The input points can also consist of spatially coincident points in order to pin down a specific bone, meaning this bone should neither be actively transformed nor should passively adopt a transformation by motion propagation of other bones across the joints.

After the calculation of the final transformed skeletal posture of the patient, the resulting transformations of the bones then serve as input for the soft tissue model in order to propagate the translations and rotations into the soft tissue. The combined DVF, resulting from the kinematic model and the soft tissue model, is used to sample artificial images. Resulting DVFs are inverted and re-sampled according to the methods described in 2.9.1. The existence of images representing the modelled posture is a prerequisite for the generation of a plan library in the plan-of-the-day concept. The feasibility of forward-simulating various postures of different magnitudes of motion and a varying number of bones involved in different anatomical regions is demonstrated by the following examples.

The developed biomechanical model is used to generate different postures of the patient, representing commonly observed anatomical variations in the anatomy during the course of radiotherapy. In this context, different postures of head and neck cancer patient 1 are simulated. Resulting postures, DVFs and the re-sampled images in an image fusion technique are shown in Figure 35. After construction of the kinematic model based on the anatomy in the planning CT, interactive manipulation is used to induce small anatomical changes in the skeletal posture within the range of typically observed variations in radiotherapy.

All three simulated postures represent typical variations of the skeletal anatomy during radiotherapy. The transformations of the individual bones reveal the potential of the kinematic model to induce physically meaningful local deformations, which propagate into the soft tissue. Even the combination of complex deformations in the shoulder area, involving mainly scapulae, humeri and clavicles with head rotations or other local deformations are of a visually good quality. As all bones remain rigid and the deformation is regularized by the permissible range of motion of the joints, only a few input feature points are required for the kinematic model to generate various postures.

Beyond the simulation of small anatomical changes, the biomechanical model is also capable to represent major changes in the posture. For example a patient who is positioned in an arms-up posture for treatment may not be capable of adhering to the same position for the whole treatment course due to his health condition or due to the patient's discomfort. For such cases, having already calculated arms-down treatment plans available as an alternative treatment position may be of benefit. The generation of an arms-down posture based on a reference anatomy in an arms-up position is simulated using the image data of head and neck cancer patient 2 as described by Teske et al. (2017a). In this case, a total of 15 landmarks obtained from one exemplary expert observer, distributed with three each on the skull, scapulae and humeri are used as input for the kinematic model (see Figure 36). Using these landmarks as input, the arms-up skeleton, on which the kinematic model is constructed, is transformed to fit the corresponding arms-down target feature points. Figure 37 shows the resulting transformations of the bones, the DVF and the image fusion of the re-sampled image of the transformed anatomy.

Even for very large anatomical changes occurring in the arms-up to arms-down posture simulation, the skeletal configuration seems meaningful without observing obviously wrong bone positions or orientations. As expected, the DVF indicates the largest changes in the most distal parts of the humeri, decreasing in medial direction as characterized by the rotation in the glenohumeral joints. Scapulae experience an upward rotation tangential to their spatial boundaries shared by the ribcage. The image fusion in the third panel of Figure 37 highlights the large magnitude of the anatomical changes in the shoulder area, while the deformations in the cranio-spinal region remain less distinct.
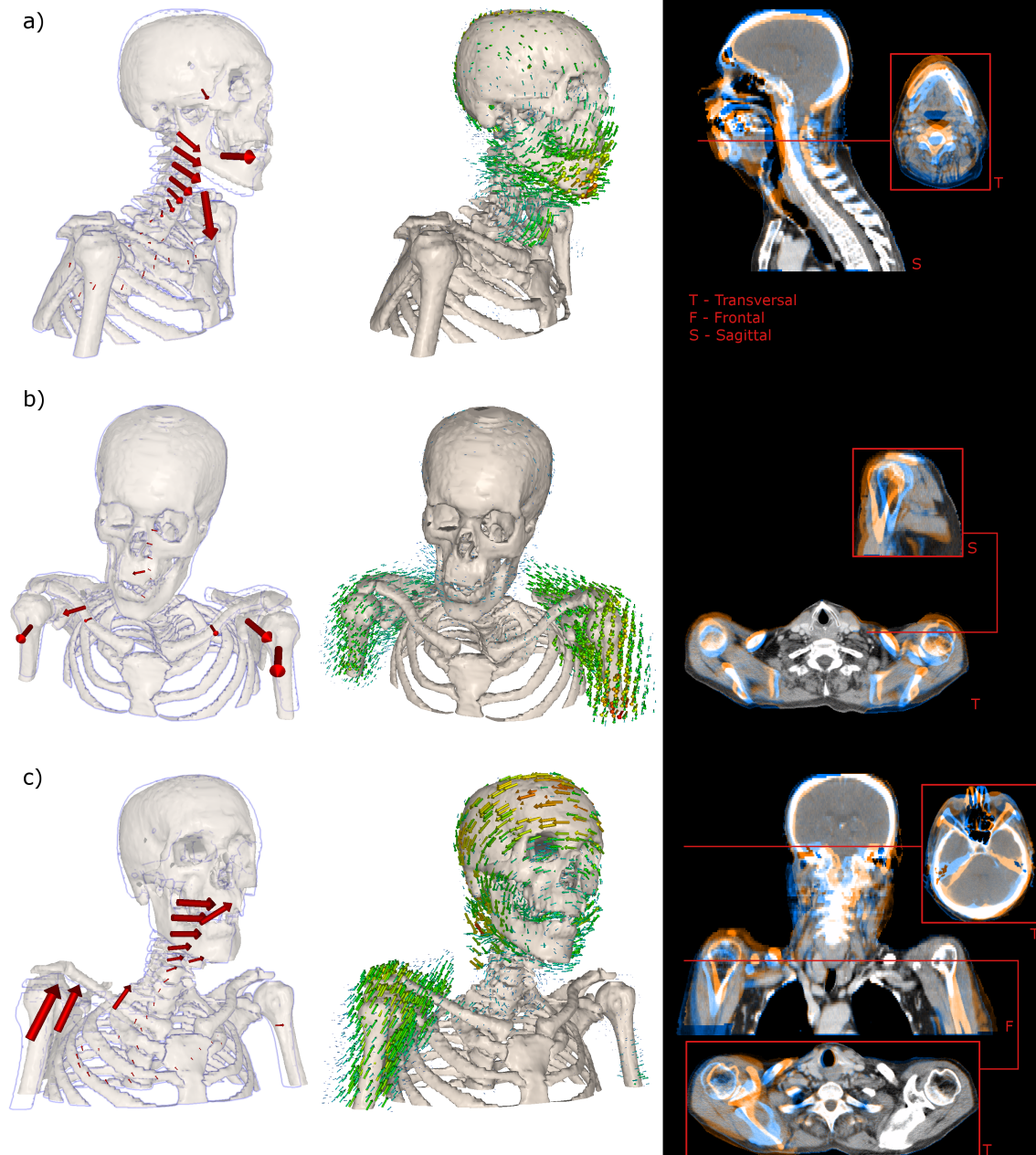
Figure 35: Illustration of three different forward-simulated postures with the kinematic model and the subsequently propagated soft tissue. Simulated postures encompass a) a stretch in the neck area with a slight rotation of the head about the left-right axis, b) protraction of both shoulders and c) lift of the right shoulder combined with a rotated skull about the cranio-caudal and anterior-posterior axes. The first column shows the outline of the reference skeleton in blue, the translations of the involved bones (red arrows, scaled by a factor of 4 for better clarity), and the resulting simulated posture. In the second column, the corresponding DVF of the skeletal transformations and the soft tissue deformations is shown. The third column shows exemplary slices of the re-sampled images of the transformed anatomy (orange) and the original image (blue) as an overlay.
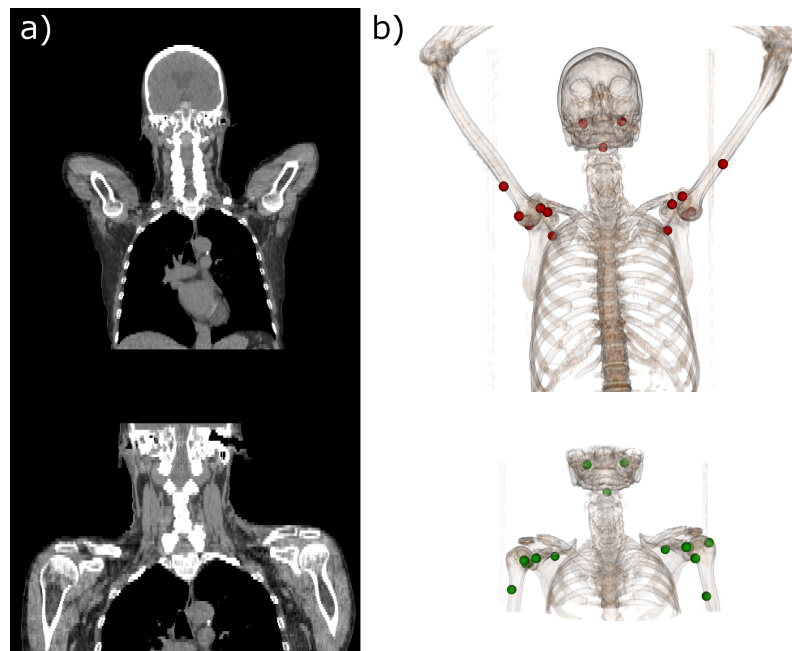
Figure 36: Illustration of the a) large arms-up arms-down posture change in exemplary frontal image slices and b) the distribution of the 15 landmarks in a volume rendering visualization, used as input for the kinematic model to forward-simulate the arms-down posture based on the arms-up anatomy. All landmarks consist of pairs of reference feature points on the arms-up anatomy (red spheres) and corresponding target feature points (green spheres).
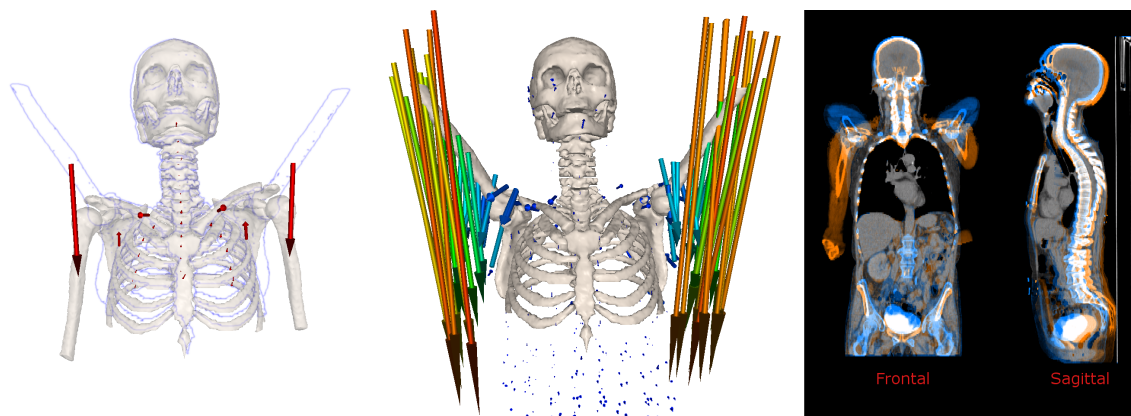
Figure 37: Illustration of the arms-up to arms-down posture simulation using 15 pre-defined landmarks. The first panel shows the initial skeletal anatomy as a blue outline and the simulated arms-down posture. Actual translations of the involved bones are shown as red arrows. The DVF in the second panel visualizes the induced transformations of the bones and the surrounding soft tissue by arrows, sized and coloured according to the magnitude of the anatomical change. Resulting re-sampled images of the generated arms-down in orange and the initial arms-up posture in blue are shown as an overlay for an exemplary frontal and sagittal slice.

In the given scenario with pairs of only 15 manually defined corresponding feature points distributed on the skull, humeri and scapulae, the accuracy of the match as the mean of the residual errors between the corresponding feature points after transformation is assessed. Resulting mean residual errors as well as the error range on those actively transformed bones, i.e. with landmarks as input, are summarized in Table 3.

Table 3: Achieved residual errors averaged per bone and the range of the residual errors per bone as a result of the arms-down posture generation using 15 manually defined landmarks, of which three are located on each of the bones.

Bone	**average error [mm]**	**error range [mm]**
Skull	0.6	0.43 - 0.86
Scapula L	1.17	0.84 - 1.74
Scapula R	1.84	1.06 - 3.14
Humerus L	1.08	0.53 - 1.63
Humerus R	1.78	1.45 - 1.99

An impression is given on how the final posture would look like when common intensity-based DIR methods supporting a feature point guided registration are used to represent such a large anatomical change with the same input of only 15 landmarks as shown in Figure 36 as for the kinematic model. Two widely used DIR methods were selected as exemplary for this task, the thin-plate-spine based *Landwarp* method of *Plastimatch* and the demons based *Anaconda* method of *Raystation* (see section 2.4). It has to be noted that both methods are used in their default configuration and the input landmarks used may not reflect the optimal conditions for these methods. Figure 38 illustrates the postures as a result of the transformations using the same input.

a) reference   b) kinematics-based   c) thin-plate-spline   d) demons
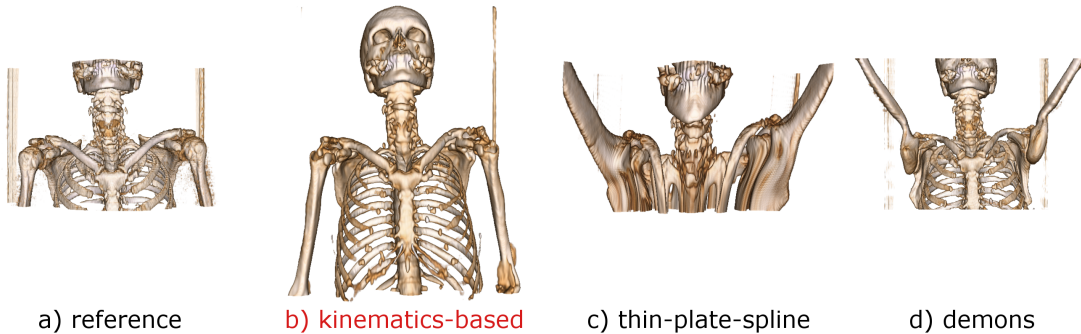
Figure 38: Illustration of the resulting postures using different exemplary transformation models with the same input of 15 landmarks distributed on skull, scapulae and humeri to guide the transformation from an arms-up anatomy to the arms-down anatomy. Volume rendering of the postures are shown for a) the reference arms-down posture as acquired from the original treatment planning image scan, b) the posture generated by the kinematics-based model, c) the posture obtained with a thin-plate-spline based transformation model (*Landwarp*) and d) the posture achieved after registration with a demons-based transformation model (*Anaconda*).

The generated postures resulting from the kinematics-based transformation is most similar to the reference arms-down anatomy. Although the landmarks were used to guide the transformation, both used exemplary intensity-based transformation models did not

succeed to transform the humeri into an arms-down position. Especially for the thin-plate-spline based method, considerable deformations within the bones occur. In order to achieve physically meaningful transformations as for the posture resulting from the kinematics-based model, the number of input landmarks potentially has to be much higher.

Beyond the inter-fractional anatomical changes in the posture of the patient, also intra-fractional motion plays an important role in ART. Figure 39 illustrates a modelled elevation of the ribcage, approximating breathing induced changes in the anatomy.
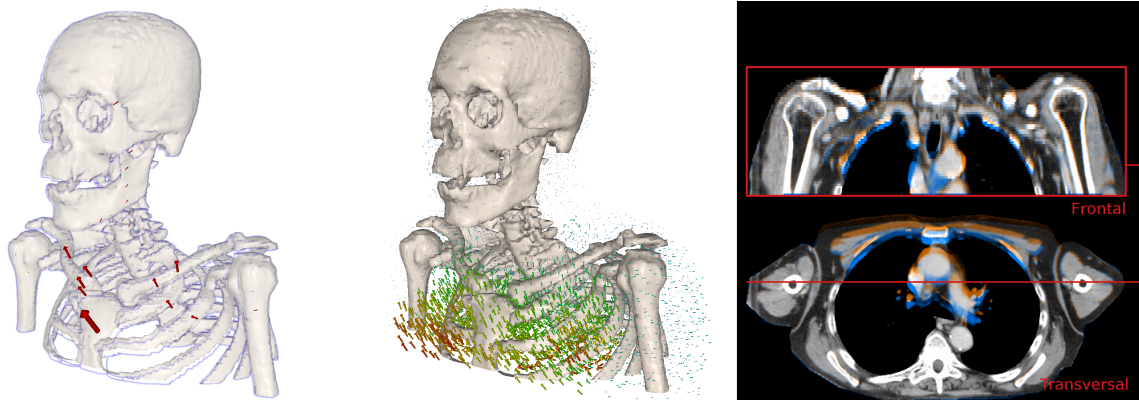
Figure 39: Illustration of a forward-simulated ribcage elevation based on the kinematic model, as involved in breathing motion. The left panel shows the outline of the original skeletal posture in an expiration state (blue lines), the simulated skeletal posture after inspiration and the according translations of the bones (red arrows, scaled by a factor of 4 for reasons of clarity). The panel in the middle shows the DVF of the regions where anatomical changes in the bones and soft tissue occur, seized and coloured according to the magnitude. The panel on the right shown exemplary frontal and transversal slices of the re-sampled images of the anatomy in the inspiration state (orange) and initial expiration state (blue) as overlay.

The ribcage elevation was achieved by interactively pulling the sternum towards an anterior-cranial direction, while the humeri and the spinal column were actively pinned down in order to inhibit a propagation of the motion into these areas. This way, a local elevation of the ribcage is achieved.

3.4 Biomechanics based registration approach

The adaptation of the treatment plan to compensate for anatomical variations of the patient before each treatment fraction relies on the accurate assessment of the deformations occurred, within a reasonable amount of time. In previous section 3.2, the performance of the kinematic model in reproducing different postures of the patients over the course of treatment was evaluated. Since the assessment of deformations within the patients anatomy is a time critical step, the iterative process of finding the correct transformations is preferred to be automated. As part of the investigation on the feasibility of using the developed kinematic skeleton model as a transformation model in such an automated registration context, the kinematic model is embedded into a custom registration pipeline. Furthermore, its achieved registration accuracy is assessed and accompanying benefits and limitations are investigated.

3.4.1 Composition

The biomechanics based registration method consists of the kinematic model to describe anatomical changes in the posture of the patients between treatment planning and treatment fractions. An image-based similarity metric is implemented to automatically assess the quality of the reproduced postures, compared to the anatomy in the fraction images. In combination with an optimizer, the parameters for controlling the postures of the modelled skeleton are iteratively adapted in order to find the best possible fit of the articulated skeleton to the anatomy of the patient in the fraction images. The soft-tissue adaptation with the tissue specific chainmail-based deformation model is performed as soon as the final skeletal posture is found.

3.4.1.1 Kinematics based transformation model

As described in section 3.1, the kinematic model is constructed based on the reference anatomy extracted from the image scans acquired with the planning modality. In order to enable an alteration of the transformations of the bones, the desired position and orientation of each bone is directly characterized by three parameters for the translation $T = [t_x, t_y, t_z]$ and three for the rotation $R = [r_x, r_y, r_z]$, respectively. These parameters are mapped to pairs of three linearly independent control points, which are internally treated as pairs of markers and observations, as described in section 2.8. Besides the parameters for T and R, the position of the rotation centre can be chosen to be either coincident with the centre of mass of the bone or coincident with the position of any joint, which is directly connected to that bone. The location of the rotation centre coincident with a joint for example allows for a straightforward description of rotations directly around the joints without the need for additional translational components as compensation. Table 4 summarizes which transformation parameters are optimized and which rotation centre is applied per bone group.

Table 4: Optimization parameters with bone-specific values used in the kinematics-based registration approach. For the transformation parameters per bone, either translation (T), rotation (R) or both (TR) can be subject to optimization. The rotation centre is selected to be located coincident with either the centre of mass of the bone (C) or the rotation centre of the joint connected to the child bone (J_c) or connected to the parent bone (J_p). Simplex initialization values for the transformation parameters of the bones are randomly sampled from the given ranges.

Parameters	Skull	Scapulae	Vertebrae	Sternum	Humeri	Ribs	Mandible	Clavicles	Hyoid bone
Transformation	TR	TR	TR	TR	R	R	R	R	TR
Rotation centre	C	C	C	C	J_c	J_c	J_c	J_p	C
Init range T (mm)	±3.0	±10.0	±3.0	±5.0	–	–	–	–	±5.0
Init range R (°deg)	±0.9	±3.0	±0.9	±1.5	±5.0	±3.0	±3.0	±3.0	±1.5

3.4.1.2 Simplex-downhill based optimizer

For the optimization of the transformation parameters T and R of the kinematic skeleton model, a prototype for an optimization algorithm supporting multiple parameters is developed. While the implementation of the optimizer is based on the widely used simplex downhill algorithm (see section 2.5.1), several adjustments and extensions are made. In accordance to the original simplex algorithm, the optimization of multiple parameters is realized by minimization of the objective function and is divided into several simplex vertices. Here, each simplex vertex represents a different configuration of parameters T and R for the same bone.

For the initialization, each simplex vertex adopts the current transformation of the bone plus a random offset. This offset is randomly sampled from a uniform distribution of a predefined range, for example representing the range of typical anatomical variations occurring for that bone. There is an option to exclude one of the simplex vertices from adopting an additional offset. This way, a good initialization can be provided for example in case a bone is already pre-registered. Concrete initialization ranges for T and R are summarized in Table 4. After initialization of the simplex, the simplex downhill optimization process is run through. Used simplex coefficients are derived from Nelder and Mead (1965) and are summarized in Table 5.

Table 5: Simplex coefficients used for in the kinematics-based registration approach - as proposed by Nelder and Mead (1965).

Simplex coefficient	value
reflect	1.0
expand	2.0
contract	0.5
compress	0.5

As an extension, the kinematic model is embedded into this optimization process in order to regularize the transformations. At every step a change to the transformation parameters is made by the simplex, the same set of parameters is then transferred to the kinematic model. After conversion to pairs of control points, it is used as input to model the anatomical changes. In a feedback step, the actually achieved transformations as a result of the kinematic modelling are converted back and replace the original optimization parameters, which were initially used as input. Additionally, the objective value achieved for the transformed anatomy in the kinematic model is calculated according to the similarity metric and the resulting value is assigned to the corresponding simplex vertex.

The simplex downhill algorithm features a heuristic search method to optimize multiple parameters of nonlinear problems. In its original implementation, the algorithm is susceptible to converging in local minima within the solution space of the objective function. The existence of local minima strongly depends on the registration context, in particular different shapes of the bones, different image modalities and their corresponding intensity distributions and the used similarity metric. In order to prevent the optimizer to get stuck in a local minimum of the objective function, disturbance steps are integrated as an extension to the classical simplex downhill algorithm. The disturbance is realized by randomly sampling disturb values from a uniform distribution with a limited range and by adding these values to the current values of the parameters. In each disturbance step,

the range of the disturb value Δ is determined as

$$\Delta \in [1, 1 + (3 * (d_{ineff} + 1))],$$

with d_{ineff} denoting the number of previous ineffective disturbance steps. A previous disturbance step is considered ineffective as soon as the relative improvement regarding the objective value between the best simplex vertex in the current disturbance step and the best simplex vertex in the previous disturbance step is smaller than a given threshold. This threshold is empirically determined and consistently set to 1% for all the bones. For an increasing number of ineffective disturbance steps, the possible range of the disturb values Δ increases accordingly in order to take into account larger gaps between potential local minima in the solution space to increase the sampling area. A disturb value $\Delta = 1$ directly relates to 1 mm for translations. Whereas for rotations, the value is multiplied by a rotation dampening factor in order to mitigate this effect for rotations. Depending on the registration scenario and the ratio of present translations and rotations, a smaller or larger rotation dampening factor might be useful and can be parametrized. In most scenarios, a fixed value of 0.3 is set for the rotation dampening factor as default, resulting in 0.3 degrees rotational disturbance for $\Delta = 1$ mm translational disturb value. To avoid losing track of the previously achieved optimization progress, the disturbance step is not applied to the simplex vertex yielding the best objective value.

Regularization through the embedded kinematic model is achieved on the one hand by the underlying physical kinematic equations and by pinning down the previously optimized bones on the other hand. The more bones are pinned down at the same time in the kinematic model, the stronger the effect of regularisation on the transformations of the bones is. Such regularisation effects can evoke a deadlock in the optimization process. As soon as the kinematic model is no longer able to transform a bone to any extent due to a strong regularisation, the identical transformation parameters as in the previous optimization step are returned to the simplex algorithm, which would result in a loop within the optimization workflow. To cope with the issue, a mechanism to detect such deadlocks is implemented.

As soon as the optimizer reaches the compress step in its internal workflow (see section 2.5.1), a disturbance of the simplex vertices is considered. The moment to trigger a disturbance of the simplex vertices is determined according to two criteria. As a first condition, a disturbance should be considered when the objective value of the best simplex vertex does not change by a certain degree over the last N iterations. For that, the mean change of the objective value of the individually best simplex vertex is calculated over the previous $N = 5$ iterations and normalized to the volume of the optimized bone, i.e. its number of voxels. The disturbance condition is met when this value is smaller than a specified threshold. For the second condition, the simplex area is used as an indicator in order to detect whether the optimization process is stuck due to the kinematic model being too restrictive. This could happen for example if the optimizer subsequently compresses the simplex to narrow down the search space, which is reflected by compressed parameters for the transformations of the bones. At some point, the best fit of the kinematic model is found. In fact further compress steps by the optimizer change the parameters, however the best parameters returned by the kinematic model do not change any more. In order to detect such behaviour, the difference in the simplex area before the fit of the kinematic model and after the feedback of the parameters from the kinematic model is calculated in every compress step. Continuously for the last 5 compress steps, the standard deviation over the simplex area differences is calculated, which serves as an indicator to detect a

stuck optimization. If the standard deviation is smaller than an empirically determined threshold, the second condition to trigger a disturbance will be met. As soon as both, the first and the second conditions are met, a disturbance of the parameter configuration of the simplex vertices is triggered. The used values as disturbance conditions are summarized in Table 6.

Table 6: Disturbance parameters and empirically determined thresholds defined in the kinematics-based registration approach to trigger a disturbance step in the optimization process. Disturbance steps are triggered as soon as the values for both criteria are smaller than the specified thresholds. The disturbance criteria consist of the mean change in the objective value of the best simplex vertex over the last 5 iterations normalized to the volume of the optimized bone and the standard deviation over the differences of the simplex area over the last 5 compress steps.

Disturbance parameter	threshold
normalized mean change obj. val.	-0.00015
stdev. simplex area differences	0.5

The detection of the optimizer converging to a potential local minimum in the solution space is realized by keeping track of the changes of the simplex area over the last few iterations of the optimization process as well as by observing the changes in the achieved objective value over time. The whole optimization process for one bone is repeated until certain convergence criteria are met. Besides a predefined maximum number of iterations, the occurrence of a sequence of constant objective values for a specified number of iterations indicate the final convergence of the algorithm. A maximum number of successive ineffective disturbances is defined as an additional convergence criterion. Values for the convergence criteria are summarized in Table 7.

Table 7: Convergence parameters used in the kinematics-based registration approach and their empirically defined thresholds. Convergence of the optimization is indicated if at least one of the given thresholds for these three parameters is exceeded. Convergence parameters involve a global iteration limit, the maximum length of the sequence of constant objective values for the best simplex vertex and the maximum number of disturbances turned out as ineffective.

Convergence parameter	threshold
global iteration limit	5000
max sequence constant obj. val.	100
max ineff. disturbances	5

Figure 40 shows an exemplary optimization curve for the right scapula of patient 1 for the registration to the 2nd treatment fraction. The effects of the disturbance mechanism and the convergence criteria are shown. During the optimization of the transformation parameters of the right scapula, the disturbance mechanism was triggered six times. First occurrence is observed in iteration 99, in which a convergence to a local minima was detected. The disturbance of the transformation parameters for all simplex vertices except the best one achieved the escape of the local minimum and an entailing improvement of the objective values for the following iterations. The second local minimum was found in iteration 198, which was also escaped by the disturbance mechanism. For the last four
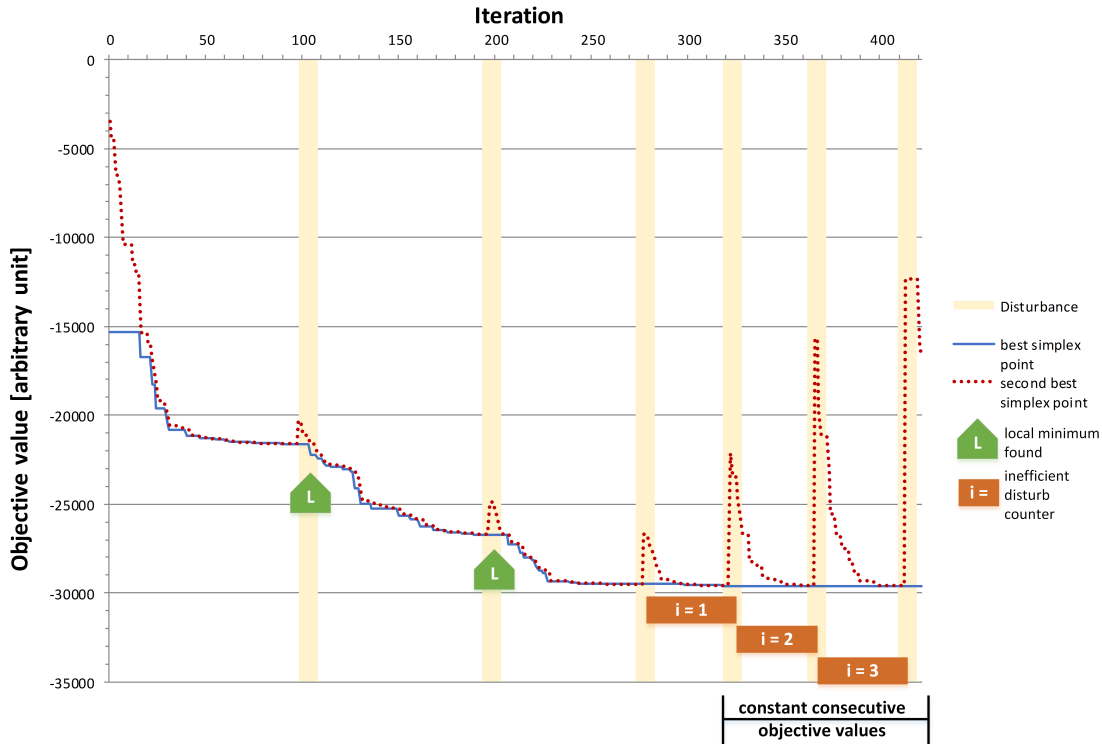
Figure 40: Optimization curve for an exemplary iterative fit of the right scapula of patient 1 to the anatomy in the image scan of the 2nd treatment fraction with the kinematics-based registration procedure. The optimization goal is to iteratively minimize the objective value for the given bone. Over the iterations, the objective values of the best simplex vertex, i.e. that configuration of the transformation parameters of the scapula yielding the best similarity value, is continuously getting smaller. As annotated, a total of six disturbance steps are triggered with two local minima found. Peaks in the objective value shown in the curve of the second best simplex vertex indicate the parameter changes associated with the disturbances. Convergence is reached as soon as either the maximum number of consecutive constant objective values is reached or the maximum number of ineffective disturbance steps is exceeded. Ineffective disturbance steps do not entail reasonable improvements in the objective value, as shown for the last disturbance steps.

disturbance steps in the iterations 278, 323, 367 and 414, the disturbance mechanism could not lead to an improved objective value and thus convergence to the global minimum is indicated. Together with the maximum number of iterations showing a consecutive constant objective value for the best simplex vertex over the last 100 iterations, global convergence is assumed and the optimization process is stopped.

3.4.1.3 Hierarchical optimization scheme

For the task of mimicking posture change of the whole skeleton, a hierarchical optimization approach is used. In order to optimize multiple bones, several dedicated simplex optimization processes are run successively. While each simplex optimizes the transformation of exactly one bone at a time, the same kinematic model is shared by all simplex

optimizers. That means for every previously optimized bone, its resulting transformation is stored as a state in the kinematic model and is considered for the following optimization processes. For the kinematic model, this is realized by pinning down all previously optimized bones in their previously achieved transformation to avoid further alterations to these parameters in subsequent optimizations. Since the bones are connected by joints within the kinematic model, their transformations are propagated across the skeleton. This is made use of by actively optimizing only some of the bones, while the remaining ones adopt their transformation by the propagation within the kinematic model. The choice of which bones actually are actively optimized in which order depends on the registration context.

For example it is beneficial to start with the optimization of the transformation parameters of the skull, when a stereotactic frame attached to a thermoplastic mask is used for patient positioning in radiotherapy. In this case, the skull is assumed to be already in a position and orientation at or near the optimum and the optimization of the potentially remaining differences is a straightforward task. Additionally, when the skull is selected as the root element of the kinematic tree, its transformation resulting from the optimization directly propagates to all other bones in a rigid manner.

For the task of fitting the skeletal posture of a patient in the reference image to the anatomy in the images taken immediately before the treatment sessions, the registration procedure is performed in two stages. First, only a small fraction of the bones distributed over the skeleton is optimized in order to obtain a rough fit of the overall skeleton. This way, a meaningful initialization for the remaining bones can be achieved. Based on the roughly aligned anatomy, in the second stage, the optimization of additional bones is performed. In order to exploit the property of the kinematic model to be able to propagate transformations of individual bones across the joints, not every single bone was actively optimized. The positions and orientations of already optimized bones are taken into account for subsequent optimizations. As described in Figure 41, the following bones were optimized in the given order for obtaining a rough fit of the skeleton.

The skull was chosen to be the initial bone for optimization since for this patient, a stereotactic frame was used for positioning before treatment. As the skull also represents the root element of the kinematic tree, changes to its position and orientation during optimization result in rigid transforms of the whole skeleton and allows for the initial alignment of the skeleton. For the next bones, the left and right scapulae are optimized to approximate the anatomical changes in the shoulder area of the patient. Both bones have a relatively large volume, expressed in a characteristic shape and thus can be easily fitted into the images. Subsequently, the spine is aligned by the optimization of every second vertebra in caudal direction, starting from the 1st thoracic vertebra until the last vertebra, which is covered in the FoV of both, the reference and the fraction images. The chosen cranio-caudal direction is chosen to obtain a better initialization for the individual vertebrae since the skull as the most cranial bone is already optimized. Each subsequent optimization of a more caudally located vertebra serves as a pre-initialization of the next vertebrae in the same direction. Finally, the sternum is optimized in order to approximate the posture in the anterior thoracic area.

As shown in Figure 41, the refinement of the fit of the posture involves the optimization of the more distal bones as well as some of the bones adjacent to already optimized ones. First, the transformations of the left and right humeri are optimized in order to approximate the variations in the posture of the arms. The optimization of the 1st to the 6th ribs on both sides aims at compensating for induced breathing motion affecting the ribcage. Before optimizing the ribs, the cervical vertebrae and the remaining not yet

optimized thoracic vertebrae are pinned down by adding pairs of coincident control points to enforce an identity transformation for those bones. The next optimization targets the mandible to adapt to changes in the jaw position. The rotation of the left and right clavicles are subsequently optimized. As a last bone for the refinement of the fit of the posture, the hyoid bone is optimized to correct for swallowing induced motion.
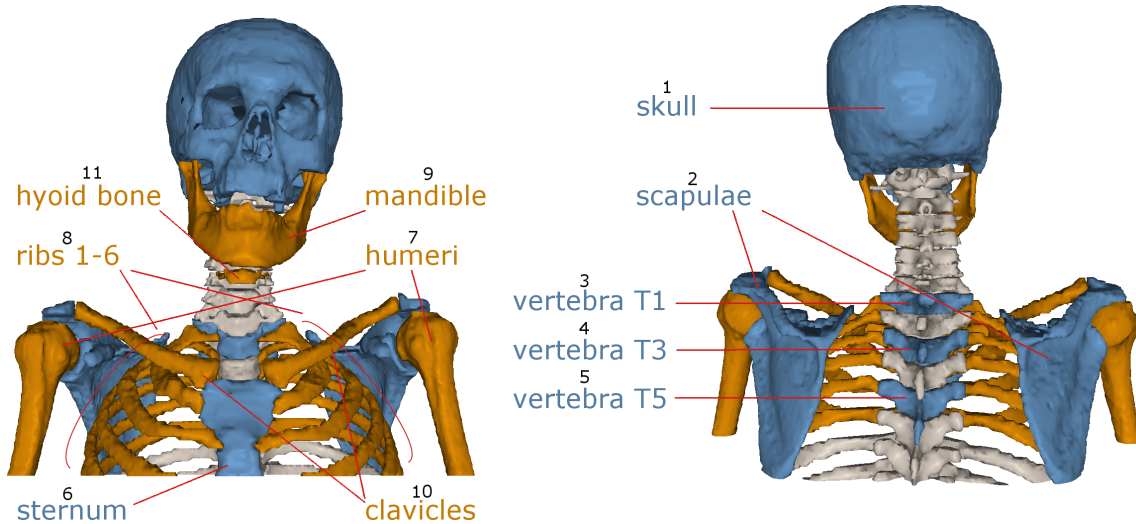
Figure 41: Bones selected as candidates for an active optimization in the hierarchical kinematics-based registration approach, exemplary for patient 1. While the bones involved in the rough fit of the skeleton are highlighted and annotated in blue color, the bones for the subsequent refinement of the fit are highlighted in orange color. The optimization order is given according to the enumeration.

3.4.1.4 Overlap based similarity metric

In every iteration during the optimization process, the kinematic model receives the transformation parameters as input from the simplex optimizer in order to transform the bones. After transformation, an image-based quantification of the similarity of the transformed anatomy to the anatomy in the target fraction image is used to quantify the goodness of the fit. For that purpose, a threshold is applied to the intensity values of both, the reference image the kinematic model is based on and the target fraction image in order to extract merely the bony tissue. To do so, only voxels with intensity values in the range of $[120, 2000]$ Hounsfield units (HU) are considered. Intensity information for all other voxels is discarded. Figure 42 illustrates the resulting image after applying this band-pass filter, exemplary for the planning CT of patient 1.

It is observed that the chosen range of 120 to 2000 HU extracts most parts of the skeletal anatomy of the patient. For bones like the skull or the humeri, only the dense cortical bone tissue is extracted. Besides the bones, imaging artefacts as shown in the 3D volume rendering are also included in the resulting images. After transforming a bone with the kinematic model, the same transformation is applied to each voxel, which is included in the thresholded image as well as part of the delineation of the given bone. Every transformed voxel, which is coincident in position with any voxel of the thresholded fraction image, is denoted as an overlapping voxel. The total number of overlapping voxels between the transformed anatomy from the reference image and the anatomy in

Figure 42: Resulting image scan after application of a band-pass filter on the planning CT for patient 1 to extract the bony tissue. The first three panels show the included bony anatomy in white in exemplary frontal, transversal and sagittal image slices and the last panel shows a 3D volume rendering of the resulting image scan.

the fraction image is used to quantify the similarity of both anatomical configurations. The more voxels overlap, the better the fit of the transformed bones is assumed. During the optimization process, the number of overlapping voxels is maximized. To comply with the minimization of the objective function in the simplex downhill optimizer, a negative sign is applied to the number of voxels to represent a minimization problem.

3.4.2 Evaluation

The achieved accuracy of the developed automated kinematics-based registration approach is assessed for the image data of patient 1 and patient 2. The automated registration is performed for the 1st, 2nd, 5th, 15th, 19th and 28th treatment fractions of patient 1, representing typical anatomical variations occurring during the course of radiotherapy. Furthermore, the large arms-up arms-down posture change of patient 2 is registered. After optimization of the skeletal anatomy, the soft tissue model is triggered to propagate the transformations of the bones into the soft tissue. In contrast to the accuracy assessment in section 3.2.3.1, the observer-defined sets of landmarks are not used as an input to guide the transformation process, but are solely used to evaluate the accuracy of the automated registration method by means of calculating the TRE as the mean of the residual errors. For this evaluation, the landmark positions of one exemplary observer (observer 1) are used.

3.4.2.1 Registration of small anatomical variations

Exemplary for the 2nd treatment fraction of patient 1, the original configuration of the anatomy is shown as an overlay in Figure 43. Furthermore, results of the the two-staged registration process are demonstrated accordingly. The registration process consist of the intermediate rough registration of the skull, scapulae, vertebrae and sternum and proceeds with the fine registration, including the humeri, ribs, mandible, clavicles and the hyoid bone. Window-level setting for the visualization is adjusted to focus on the bony tissue.

The image overlay showing the original state of the anatomy in the planning CT and the fraction CT reveals anatomical variations occurring for nearly all the bones of the skeleton covered in the common FoV. The transversal and frontal slices show a protraction of the shoulders, a slight rotation of the right humerus and an elevated left shoulder.
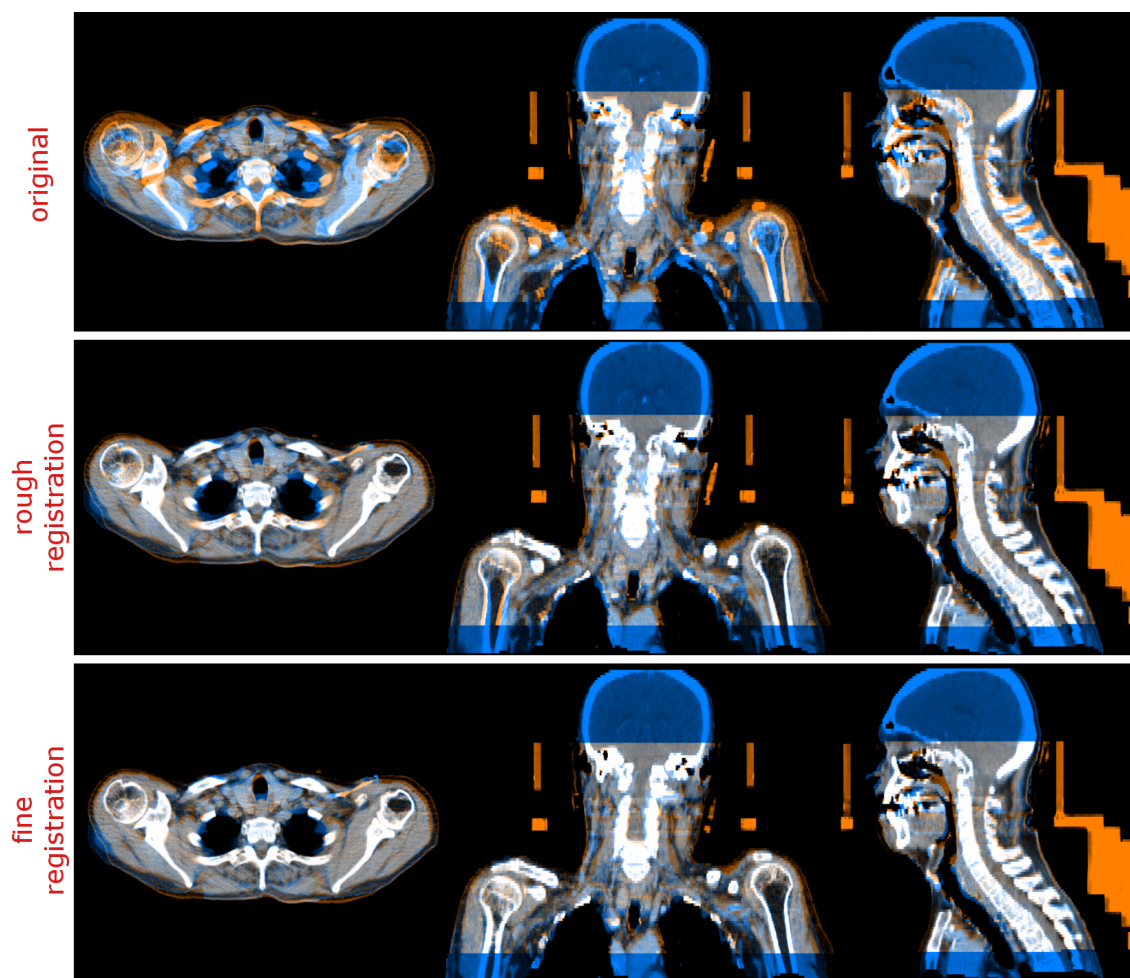
Figure 43: Visual demonstration of the achieved registration results using the automated kinematics-based registration approach for the exemplary 2nd fraction of patient 1 with the focus on the bony tissue. All panels show exemplary slices in transversal, frontal and sagittal view of the fraction image (orange) and the re-sampled image based on the current state of the kinematics-based model (blue) as overlay. The top panel shows the original state of the anatomy (blue), as extracted from the planning image. The transformed anatomy as a result of the rough registration is shown in the middle panel. The bottom panel shows the overlay of the final result after the fine registration. As the stereotactic head frame and the treatment couch are not part of the kinematic model, they do not exist in the re-sampled images.

Furthermore, variations in the positions of the ribs can be observed. In the sagittal slice, variations in skull, mandible, sternum and the vertebrae are clearly visible. After rough registration, the actively optimized bones show a visually good agreement and a reasonable fit of the skeletal posture is achieved. Remaining variations are visible for the ribs, the hyoid bone and the right humerus. The fine registration further improves the fit of the aforementioned areas containing the remaining variations. A slight offset of the hyoid bone still persists.

Using the observer-defined landmarks as a reference to quantify the accuracy in terms of the TRE, the residual errors after registration are summarized in Figure 44 on a per-

bone basis for the 2nd treatment fraction of patient 1. Achieved accuracy is measured on the transformed anatomy after the rough registration and after the fine registration.
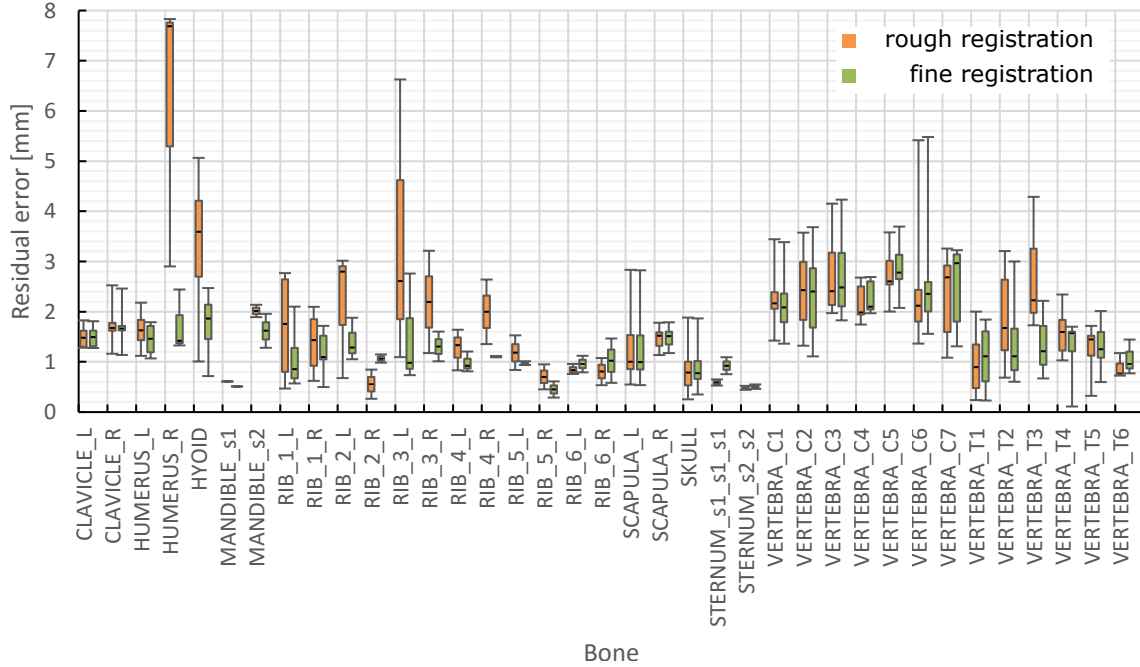
Figure 44: Achieved registration accuracy of the automated kinematics-based registration approach in terms of the residual errors on the observer-defined landmarks for the exemplary 2nd fraction of patient 1 for the two-staged registration process. Distributions of the residual errors per bone are shown for the results of rough (orange) and fine (green) registration. No distinction was made between actively optimized bones and bones, receiving their transformations through motion propagation in the kinematic model.

Regarding the resulting accuracy achieved after the rough registration of the skeletal posture, the medians of the residual errors of the actively optimized bones of skull, scapulae, 1st, 3rd and 5th thoracic vertebrae and sternum range from 0.48 mm for the sternum (Sternum_s2_s2) up to 2.23 mm for the 3rd thoracic vertebra. Large median residual errors are found for the right humerus, the hyoid bone and the 2nd and 3rd left ribs with values of 7.69 mm, 3.59 mm, 2.80 mm and 2.61 mm, respectively. Accordingly, high IQRs of 2.46 mm, 1.51 mm, 1.17 mm and 2.77 mm are reported. Those bones with the large residual errors and high IQRs were not actively optimized during the rough registration process. The results of the fine registration, additionally including the active optimization of both humeri, ribs, mandible, both clavicles and the hyoid bone, show considerable improvements of the accuracy for the right humerus, the hyoid bone, most of the ribs and the 2nd and 3rd thoracic vertebrae. The median residual error of the right humerus decreased to 1.42 mm, the hyoid bone to 1.86 mm, the 2nd thoracic vertebra to 1.11 mm and the 3rd thoracic vertebra to 1.21 mm. The mean improvement of the accuracy for the ribs equals to 0.51 mm. The largest remaining residual errors are found in the area of the cervical spine, with medians ranging from 2.09 mm for the 1st cervical vertebra to 2.96 mm for the 7th cervical vertebra. Except for the cervical vertebrae, which were not included in the set of actively optimized bones, the resulting TREs are clearly smaller than 2.0 mm.

With the same underlying optimization procedure, the achieved accuracy of the regis-

tration for the remaining 1st, 5th, 15th, 19th and 28th treatment fractions of patient 1 are assessed. Final results achieved after the two-staged registration process are summarized in Figure 45. Similar registration accuracy is shown across all examined treatment
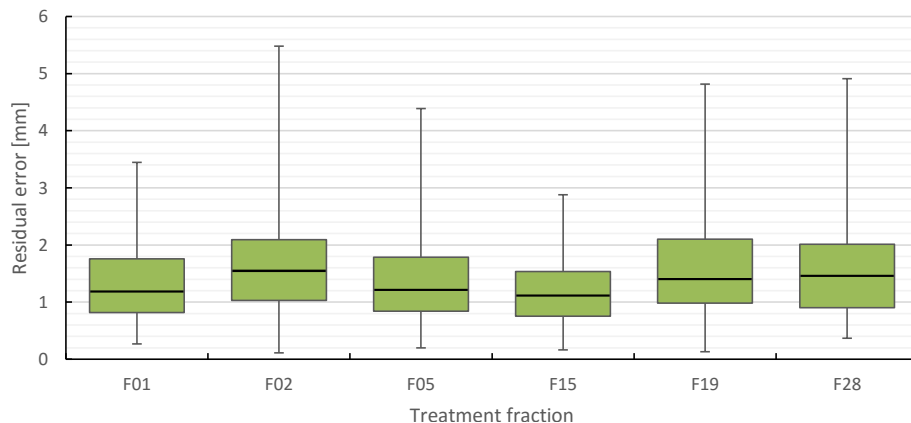
Figure 45: Distribution of the residual errors remaining after the two-staged registration process (rough registration and fine registration) with the kinematics-based registration approach for exemplary six treatment fractions of patient 1. Residual errors are assessed with the help of sets of observer-defined landmarks.

fractions. Achieved TREs range from 1.19 mm for the 15th fraction to 1.65 mm for the 2nd treatment fraction. IQRs range from 0.78 mm for the 15th fraction to 1.21 mm for the 19th fraction.

Resulting residual errors per bone across all six treatment fractions are shown in Figure 46. The medians of the mean residual errors range from 0.81 mm for the sternum (Sternum_s2_s2) to 2.26 mm for the 3rd cervical vertebra. Overall, a slightly decreased accuracy is observed for the cervical vertebrae, which were not part of the active optimization. This is in agreement with the findings in section 3.2.4.1.
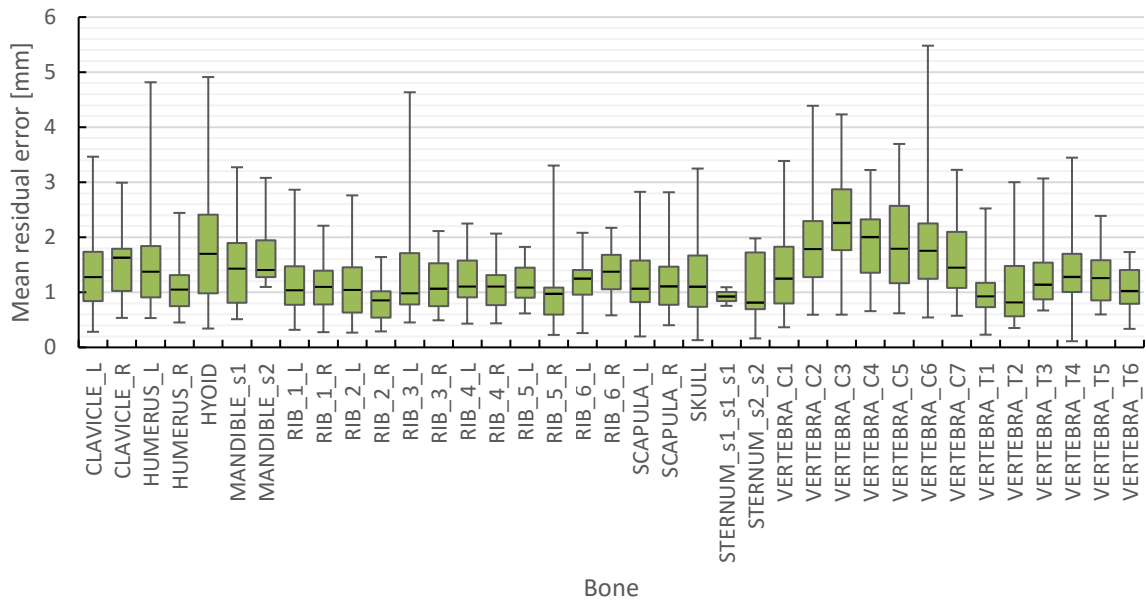
Figure 46: Distribution of the residual errors after registration with the automated kinematics-based registration approach, clustered per individual bone and averaged over exemplary six treatment fractions of patient 1 using the landmark set of one exemplary observer as reference.

Optimization of 6 DoF intervertebral joints

According to the hierarchical optimization scheme described in section 3.4.1.3, the set of actively optimized bones used for the automated kinematics-based registration approach does not involve any bone of the cervical spine. Including some or all of the cervical vertebrae into the optimization process did not yield better results in terms of the achieved accuracy. In contrast, adding for example the 2nd, 4th and 6th cervical vertebrae in the given order as optimization goals, the accuracy of adjacent cervical vertebrae is considerably deteriorated, potentially as a result of a too strong regularization through the used joint parametrizations. The passively optimized vertebrae in-between act as a compensation for potentially inadequate joint positions or types regarding their motion freedom.

In this experiment, the cervical vertebrae are included as actively optimized bones, but unlike using ball-and-socket joints, free joints having 6 DoF were used as intervertebral joints in this area. These joint allow for 3 rotational DoF and 3 translational DoF. This way, also translations can be taken into account, which further compensates for poorly positioned rotation centres of those joints. Analogous to the fine registration procedure of the whole skeletal posture for the exemplary 2nd fraction of patient 1, the same kinematics-based registration is performed with additionally optimizing all cervical vertebrae in the order from the 1st to the 7th just before the optimization of the 1st thoracic vertebra. After registration, the final posture of the transformed cervical spine is shown in Figure 47, along with the translational parts of the transformations at the intervertebral joints.

Translational offsets in the rotation centres of the intervertebral joints in the cervical spinal area account for 0.28 mm between the 2nd and 3rd cervical vertebrae to 1.39 mm for the joint between the 1st and 2nd cervical vertebrae, with a mean of 0.87 mm. The translational offsets found indicate deficiencies in either the used ball-and-socket joint types or an unfavourable approximation of the joint positions.
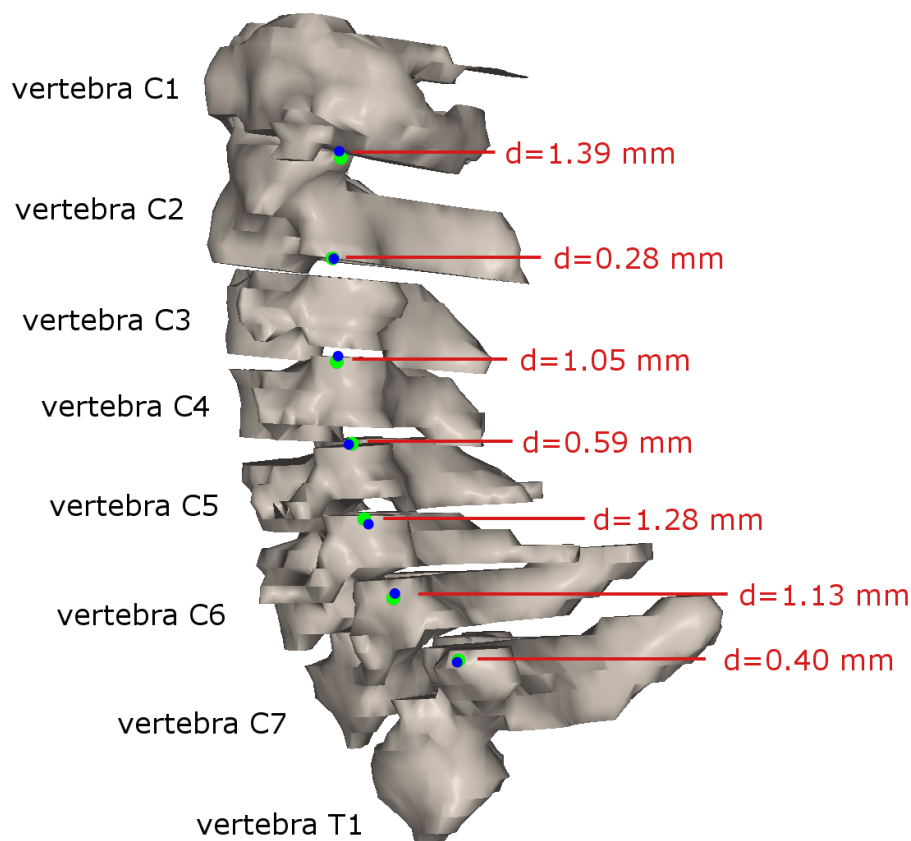
Figure 47: Transformed cervical spine of patient 1 for the exemplary 2nd treatment fraction after registration involving active optimization of all cervical vertebrae while using 6 DoF intervertebral joints in the cervical area. The green and blue spheres illustrate the translational offsets at the joint rotation centres as a result of the registration. The magnitude of the final translational offsets per intervertebral joint are annotated in red.

The resulting accuracy in the cervical spinal area achieved in this experiment is compared to the previous results using ball-and-socket intervertebral joints. Achieved residual errors per bone are shown in Figure 48 for the exemplary 2nd fraction of patient 1. It has to be noted that the cervical vertebrae are not part of the actively optimized bones in the case when ball-and-socket joints are used. The additional consideration of translational DoF for the intervertebral joints in the cervical spinal area does not lead to a deterioration of the accuracy of the fit when the cervical vertebrae are actively optimized. Besides that, the resulting residual errors are considerably lower compared to the use of ball-and-socket intervertebral joints. The median accuracy of the transformations for every cervical vertebra was improved in the range of 0.72 mm up to 2.18 mm. With the optimization of the 6 DoF joints, the median residual errors of the cervical vertebrae are all set below 1.44 mm.
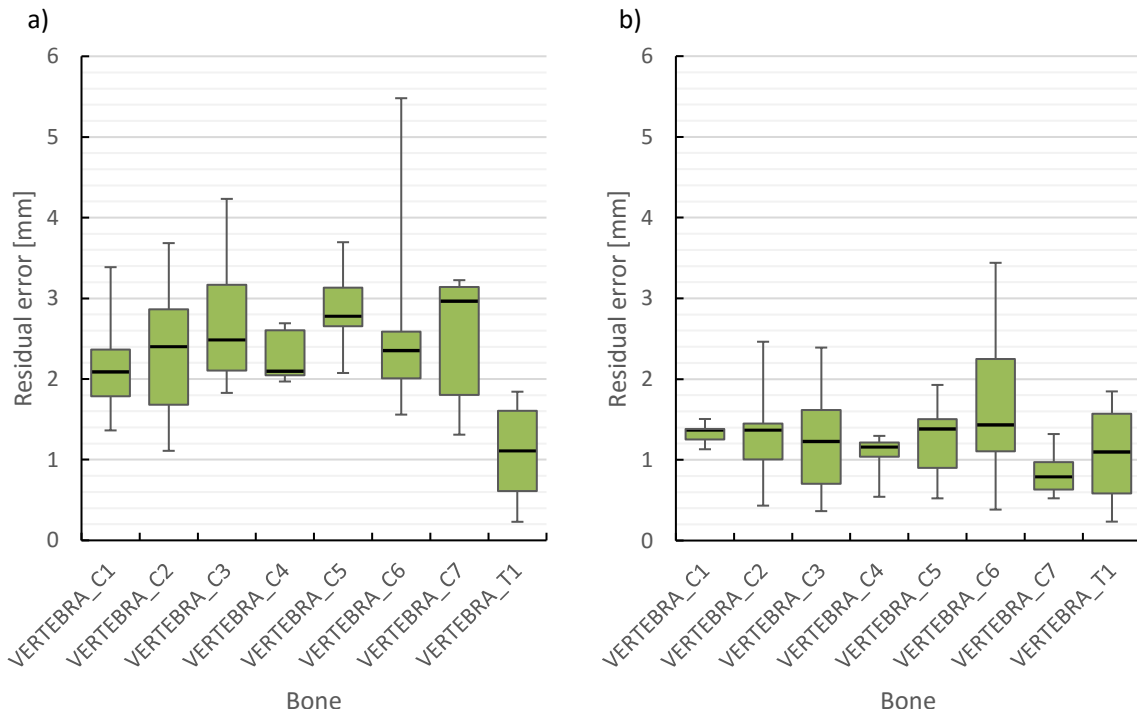
Figure 48: Comparison of the residual errors in the cervical vertebrae after registration with the kinematics-based registration approach for the exemplary 2nd treatment fraction of patient 1. In a) 3 DoF rotational intervertebral joints in the cervical spinal area are used without actively optimizing the cervical vertebrae and in b) 6 DoF translational and rotational joints are used in conjunction with an active optimization of all cervical vertebrae. Residual errors on manually identified landmarks of one exemplary observer are reported.

Computation time

The computation time required to calculate new postures with the kinematic model constructed on the basis of the anatomy of patient 1 accounts for approximately 40 ms, measured on a consumer desktop computer with an i7-2600 3.4 GHz processor, as described by Teske et al. (2017b). Hereby, a considerable amount of roughly 75% of the computation time is consumed by the calculations involved with the kinematic constraints defined for the sternum and mandible.

As embedded into the registration pipeline, many new postures need to be sampled during the iterative optimization process for every bone. In its current implementation, the total time needed for the proposed kinematics-based registration approach accounts for approximately 35 minutes per skeletal registration of the whole head and neck area of patient 1 in case all physiological joints are modelled by ball-and-socket 3 DoF joints. Under the same conditions, the registration with 6 DoF joints replacing the ball-and-socket intervertebral joints in the cervical spinal area takes a bit longer with approximately 40 minutes per fraction, which is an increase by a factor of 1.1. It has to be noted that this estimated time applies for the registration under the use of the optimization scheme as described in section 3.4.1.3 and the underlying parametrization of the optimizer regarding disturbance and convergence criteria. For the given scenario of registering the typical anatomical changes occurring in patient 1 during radiotherapy, the optimization process

for each bone converged on average in ≈ 400 iterations. During optimization of one bone, 4 postures for the optimization of only rotational DoF and 7 postures for the optimization of translational and rotational DoF for each iteration step are calculated. According to the optimization scheme involving 25 bones as shown in Table 4, a total of ≈ 50000 postures are calculated during the overall optimization process. The implementation of the optimizer is neither optimized for performance nor parallelization of modern computer hardware is considered. Moreover, rather strong convergence criteria are imposed, leading to an extended optimization time.

3.4.2.2 Registration of large arms-up arms-down posture changes

The optimization scheme chosen for the automated kinematics-based registration for patient 2 involving the large arms-up arms-down motion slightly deviates from the one presented in Figure 41, which is used for patient 1. Following the active optimization of the skull and both scapulae, the sternum was given priority over the thoracic vertebrae and is optimized next in order to achieve a better initial alignment of the spine. Obtaining a good initial alignment of the vertebrae is beneficial to avoid mismatches caused due to their high similarity in shape and size. The optimization order of the remaining bones was maintained. In addition, the process of fitting both humeri, which are the bones affected the most during the arms-up arms-down motion between the PET-CT image as reference and the CT image used for radiotherapy, as part of the fine registration are supported by adding the following initialization step prior the actual optimization. In a brute-force matching approach, the number of overlapping voxels as the quantification of the goodness of the fit of the humeri for different orientations about the anterior-posterior axis representing abduction and adduction movements are assessed for different glenohumeral joint angles θ with $0° < \theta < 180°$ for the left and $0° > \theta > -180°$ for the right humerus in steps of $2°$. The orientation of the humerus, in which the highest similarity was achieved, i.e. the maximum number of overlapping voxels, is taken as the initial orientation for the following simplex optimization routine.

Figure 49 summarizes the achieved accuracy after the fine registration stage of the automated kinematics-based registration approach for patient 2. Resulting residual errors were calculated on the observer-defined landmarks of one exemplary observer (observer 1). Overall, stronger variations in the residual errors throughout the individual bones compared to the results of patient 1 are observed. In particular, large residual errors occur with medians of 44.68 mm for the left humerus, 8.75 mm for the right clavicle and 7.74 mm for the left scapula. Bones in the shoulder area are generally less accurately registered than the other bones, which is connected to the large anatomical changes involved in this area for this patient. Besides the shoulder area, the largest residual errors arise for the cervical vertebrae, which is in accordance to the results of patient 1 and may indicate an inadequate joint parametrization in this area.
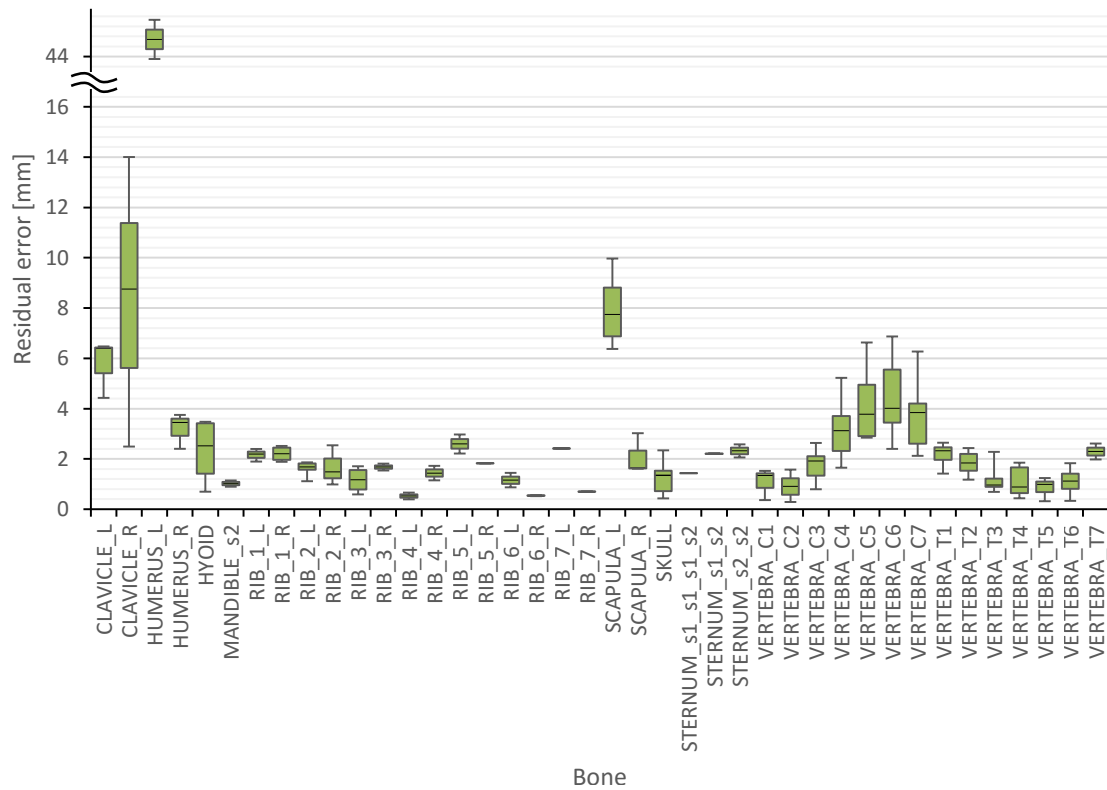
Figure 49: Residual errors per bone after the automated kinematics-based registration of the arms-up to the arms-down anatomy of patient 2. Observer-obtained landmarks distributed over the skeleton were used to calculate the residual errors.

Optimization of 6 DoF acromioclavicular joints

The large residual errors involving the connected bones of humeri, scapulae and clavicles are further investigated regarding the role of the modelled joints, which connect those bones. As a potential source of error, the ball-and-socket joints are replaced with free 6 DoF joints located at the same position, but in contrast also allow for translations around three axes. Due to the fact that the scapulae are the first bones in the underlying optimization scheme, the acromioclavicular joints connecting clavicles and scapulae are chosen to be replaced with the 6 DoF joints. As a consequence, the scapulae, humeri and clavicles are re-optimized with the new joints.

Resulting residual errors per bone are shown in Figure 50. Achieved residual errors within the shoulder area are markedly decreased compared to the results with ball-and-socket joints in Figure 49. The 6 DoF acromioclavicular joints decrease the median residual errors of the transformations of the left humerus, the right clavicle and the left scapula by factors of 11.2, 4.0 and 3.2, respectively. The highest remaining median error is observed for the left clavicle with 4.86 mm. With the 6 DoF acromioclavicular joints, the overall mean accuracy of the registration of the large arms-up to arms-down posture accounts for 2.13 mm.
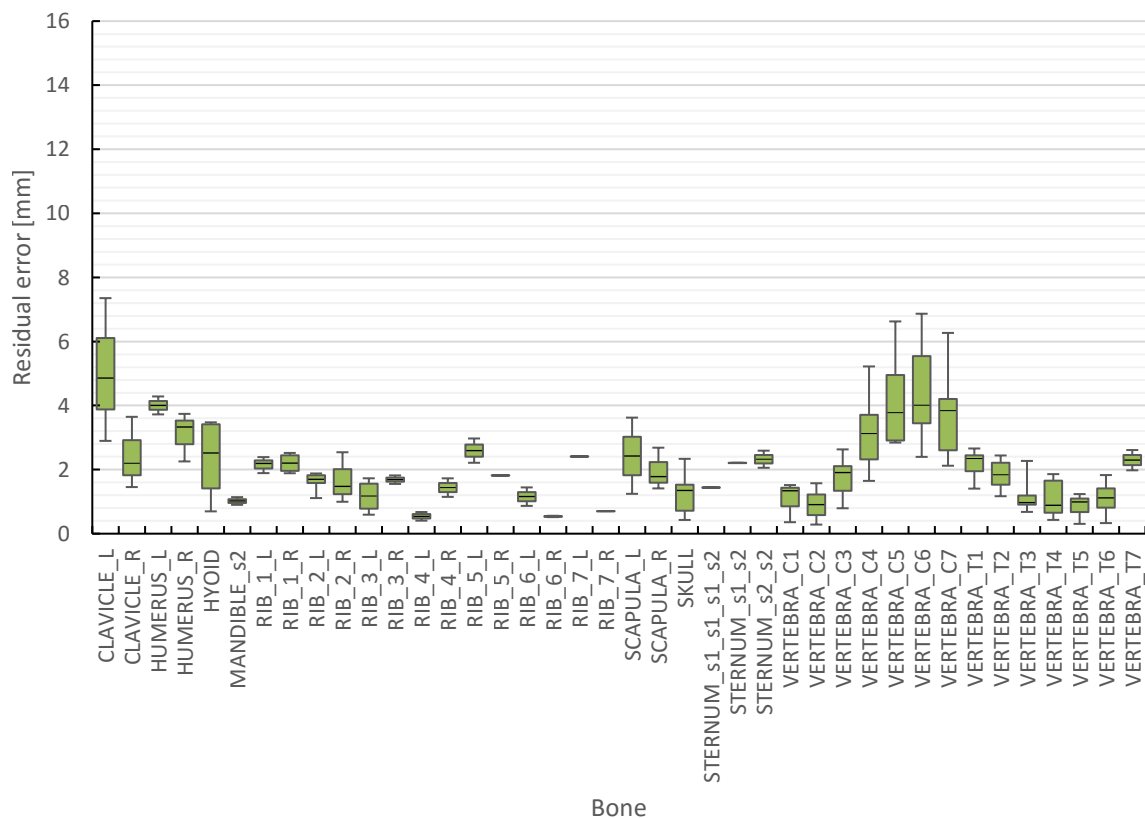
Figure 50: Achieved residual errors of the kinematics-based registration approach for the large arms-up to arms-down posture change of patient 2, using 6 DoF acromioclavicular joints between scapulae and clavicles. Residual errors are calculated based on the observer-defined landmarks distributed over the skeleton of patient 2.

The translational motion at the acromioclavicular joints is summarized in Table 8.

Table 8: Translational offsets for the 6 DoF acromioclavicular joints after kinematics-based registration.

6 DoF joint	translational offset [mm]
left acromioclavicular joint	7.47
right acromioclavicular joint	9.72

The effect of using 6 DoF acromioclavicular joints during the optimization process is demonstrated in Figure 51. A visual comparison is shown for the resulting skeletal postures of the kinematic model after registration with 3 DoF acromioclavicular joints and with 6 DoF acromioclavicular joints, respectively. An overlay of the re-sampled images from the transformed anatomy and the original arms-down posture is shown.

| Transversal right | Frontal | Transversal left |
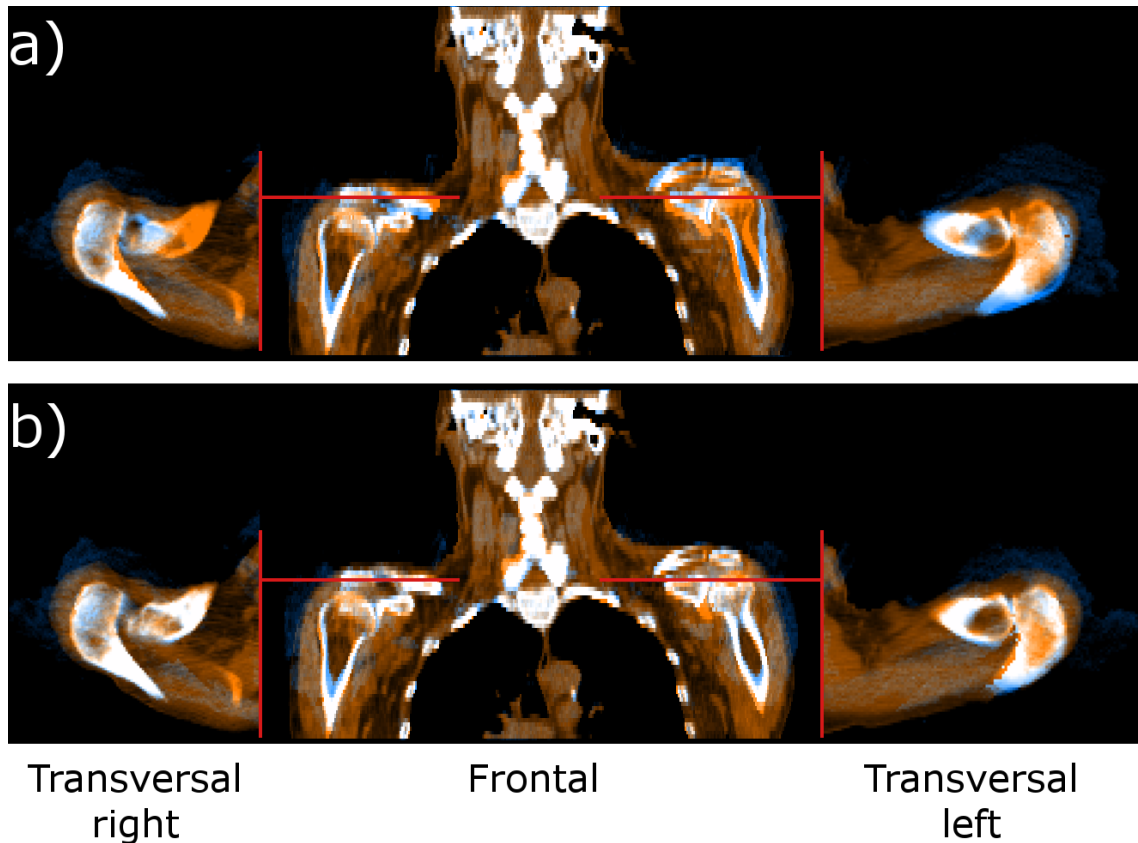
Figure 51: Comparison of the visual registration quality of the automated kinematics-based registration of the large arms-up to the arms-down posture between the use of a) ball-and-socket 3 DoF and b) free 6 DoF acromioclavicular joints during the optimization procedure. As overlay, the original arms-down CT image (orange) and the transformed and re-sampled image as a result of the registration (blue) is shown with a focus on the bony anatomy and a spatial focus on the acromioclavicular joints. The red lines indicate the locations of the image slices taken for both transversal views in the panels on the left and right. The panel in the middle shows an exemplary frontal slice.

The visual matching quality of the scapulae and the clavicles in Figure 50a for the ball-and-socket joints indicates deficiencies in the whole shoulder area. Especially for the left side, large mismatches are found after registration. The use of 6 DoF joints in Figure 50b however shows an improved visual matching quality in said areas, showing no major mismatches between the original arms-down CT image and the re-sampled one. Figure 52 demonstrates the resulting skeletal fit of the postures after the automated registration process with 6 DoF acromioclavicular joints. An overall reasonable visual agreement of the bones is found for the transformed anatomy after registration to the reference. Minor remaining differences can be observed in the area of the humeri and the cervical vertebrae.
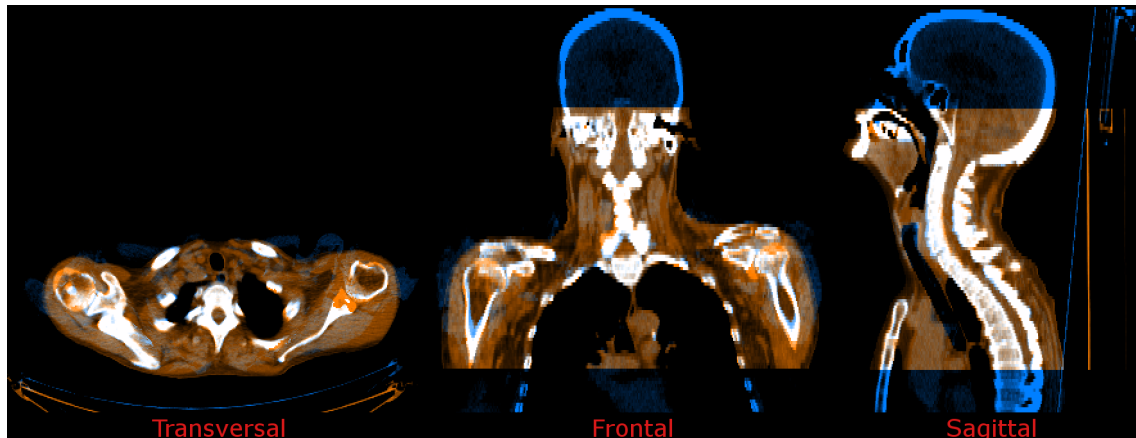
Figure 52: Image overlay of the re-sampled image scan of the transformed skeletal posture (blue) after the automated kinematics-based registration and the original image scan in arms-down posture (orange) as reference. Exemplary transversal, frontal and sagittal image slices are shown, capturing the most challenging regions.

Image artefacts can be seen in the transversal slice, which is most likely related to the interpolation and re-sampling step of the large motion involved during the arms-up to arms-down posture change. The use of the kinematic model for the skeletal anatomy allows for the complement of missing information, for example due to a limited FoV of the images, as shown for the smaller arms-down CT image as reference. Hereby, the connected bones receive potentially meaningful initializations.

Chapter 4

Discussion

The common aim of adaptive treatment concepts in radiotherapy is to take into account anatomical changes occurring during the course of treatment. Especially changes in the skeletal posture of the patient at different treatment fractions induce deformations in the anatomy and eventually lead to a deteriorated dose application. While conventional DIR methods represent a tool to assess these deformations based on image intensities, their different implementations show discrepant results (Brock 2010) and potentially lead to unrealistic deformations, which are not physically meaningful.

Beyond taking into account changes in the geometry of organs, the current trend towards using biomechanical models also enables the consideration of different tissue properties. The introduction of tissue characteristics like the rigidity of bones, direction-dependent elasticity of muscles or growth and shrinkage of soft tissue promises a more robust assessment of anatomically correct deformations. However, current state-of-the-art biomechanical models are limited to specific organs and typically are computationally expensive. That means for a clinical environment that the results of a deformation model dedicated to a single organ would require complex coupling to other deformation models in order to cover the whole area of interest for the assessment of the anatomical changes, which needs to be achieved within short time while the patient still is lying on the treatment table.

In this contribution, a novel biomechanical model was developed to enable a fast and physically meaningful deformation assessment for the whole head and neck area. It is based on a kinematic model in order to account for skeletal changes, which are then propagated into the surrounding soft tissue. Incorporating this biomechanical model, a novel automated kinematics-based registration approach was realized. Beyond its application in registration of typical inter-fractional variations during radiotherapy, its scope of application was broadened towards mimicking even large-ranged motions, such as a challenging arms-up arms-down posture change, which is a typical problem when incorporating diagnostic pre- or post-treatment images into radiotherapy treatment planning.

4.1   Construction of the kinematic model

The developed kinematic model is based on a generic model, specifying the dependencies between separate bones and their joints, which is then tailored to the individual patient anatomy represented in medical images and eventually enriched by a kinematic motion behaviour (see section 3.1). This segregation allows for the description of the assembled

skeleton model independent from the anatomy of a specific patient, for example the spe-
cification of a standard set of bones to include for a given anatomical area of interest as
well as a standard parametrization for each joint. To be detached from the individual
patient anatomy also enables an easy extensibility of the kinematic model to other body
regions. For example a kinematic model developed for the head and neck area focusing on
the thoracic region can be extended to the upper limbs or the pelvis by simply including
the topological information about relevant bones and joints for the given regions without
the need of detailed knowledge about the individual geometry. Moreover, specific areas
of interest such as the complex shoulder girdle can be refined to the level of detail which
is needed for a given scenario. For example the provision of a simplified model of the
shoulder or a more sophisticated one can be realized without the necessity of repeating
the model assembly procedure for every different patient. It has to be noted that for
every additionally included anatomical region, the use of kinematic constraints needs to
be considered in order to break potentially arising kinematic loops. In analogy to the
kinematic constraints utilized for the sternum and the mandible in the head and neck area
(see section 3.1.4), other bones such as the lowermost sternal ribs would need to be split
in parts, to which the false ribs, i.e. not directly attached to the sternum, connect.

After having specified the assembly of the skeleton of interest, it is mapped onto
the individual anatomy of the patient. This is done by delineating and extracting the
geometry of the bones from the reference image. Because bones are typically not part of
the delineation process in radiotherapy, for this work, their geometry was obtained through
thorough manual segmentation of each separate bone. This process took approximately
200 minutes for the complete anatomy of a head and neck cancer patient. While simple
approaches to automate the delineation process such as a thresholding based on image
intensities lack the achievement of an separate delineation per bone, statistical shape
models promise to overcome this issue. Still, they currently only exist for a limited number
of bones and are not yet widely available to the research community (Sarkalkan et al. 2014).
Recently published atlas-based methods implementing an articulated registration approach
for the whole skeleton show promising results towards achieving reliable delineations of
sufficient quality for the whole skeleton (Fu et al. 2017, Yip et al. 2014).

Implemented joints grant mobility to the delineated and extracted static geometry
of the skeleton and thus represent those parts of the kinematic system, which have a
major impact on the achievable biofidelity, e.g. to what degree the model is able to
anthropomorphically represent anatomical changes. In particular for the assessment of
anatomical variations in the head and neck area, the complex interplay between various
bones and joints resulting in individual skeletal postures needs to be adequately taken into
account. Due to the fact that head and neck tumors very often are located in proximity to
many OARs (Feng and Eisbruch 2007), the accurate assessment of the geometric internal
organ configuration is increasingly important to enable a precisely targeted treatment.
Therefore, in the developed kinematic head and neck model, all major synovial joints were
included in order to be able to represent the high anatomical flexibility in this area (see
section 3.1.3). A few of the minor synovial joints like the facet joints between the two
articular processes of two adjacent vertebrae were not explicitly modelled. It is assumed
that their role to limit the rotational motion of the spine has a dwindling small impact on
the model accuracy, given the fact that spinal rotation is kept very small when the patient
is positioned in a horizontal position for radiotherapy treatment.

Since the exact positions of rotation centres of the physiological joints are very hard to
identify in planning CTs even under manual assessment, these positions were proposed to

be approximated based on the geometry of the adjacent connected bones. Broken down to a purely geometrical approach, this process has shown to be suited for an easy automation, given that the bones are already delineated for the construction of the kinematic model. It has to be noted that the validity of such an approximation depends on the quality of the delineations of the bones, especially in the area adjacent to the joint position, and presumably provides positions slightly deviating from the exact anatomical positions of the joints. It was shown that for some linked bones like the scapula and humerus or the vertebrae, a simple nearest neighbour based positioning approach for the connecting joint results in inadequate joint locations, as visually assessed (see Figure 14). The use of more sophisticated positioning approaches for such dedicated joints results in more reasonable joint positions and potentially provides a higher robustness against variations in the geometry of the bones as a result of manual delineation. While only minor improvements regarding the achieved accuracy of the kinematic model were seen in the thoracic region for both patients when using the sophisticated positioning approach, a considerable increase in the accuracy is observed for the shoulder area, comprising the scapulae, humeri and clavicles (see section 3.2.3.2). This holds particularly true for patient 2, where large shoulder motions are involved in the arms-up arms-down change. Achieved improvements in the accuracy and potential benefits regarding the robustness motivate the use of the sophisticated positioning approach for the joints in the shoulder area.

Wu et al. (2002, 2005) recommend the use of standardized joint coordinate systems in order to simplify the comparability of reported results originating from different biomechanical models that have implemented their own joint mechanics. The authors motivate the use of commonly defined landmarks on the bones for determining local Cartesian coordinate systems of the bones, based on which standardized joint coordinate systems can be derived. While this seems most useful for example in gait studies, in which the reported joint angles infer the health condition of the patient, there is an extended effort required in manually determining those bony landmarks in a clinical scenario. Additionally, the typical CT image scan used for radiotherapy planning is limited in its FoV, meaning that several bones might not be fully covered and thus some landmarks needed for setting up the joint coordinate system might be out of field. For the purpose of assessing anatomical changes however, reported joint angles only represent a purely intermediate result. Especially when using ball and socket joints with unconstrained rotations around the three axes, the definition of the joint coordinate system does not have an impact on the resulting modelled motion. For the given reasons, the use of standardized joint coordinate systems were not considered for the developed kinematic model in this work. In contrast to the calculation of joint positions based on the geometry of the bones, localization of their rotation centres from multiple image scans acquired of the patient in different postures, i.e. having different joint angles, is an alternative approach. Regarding the additional effort that would be required as well as the need to acquire multiple images of the same patient at the time of treatment planning, such an approach is currently not feasible for radiotherapy.

In this work, all included joints in the head and neck region except the hyoid joint were modelled as ball and socket joints as a first approximation due to the fact that the motion at the joints in the human body is predominantly of rotational nature. Moreover, typically rather small ranges of inter-fractional motion of the skeleton are expected after the positioning of the patient (see section 2.1.4.1). Ball and socket joints in the head and neck area have been used in various biomechanical models for the glenohumeral joint (Holzbaur et al. 2005), acromioclavicular joint (Laitenberger et al. 2015, Seth et al. 2016)),

sternoclavicular joint (Garner and Pandy 1999) and intervertebral joint (Monheit and Badler 1991, du Bois d'Aische et al. 2007). Although the use of 6 DoF joints instead of 3 DoF ball and socket joints in this study has shown to slightly improve the resulting mean accuracy within a sub-millimeter range for typically occurring inter-fractional variations during radiotherapy, the increase in the computation time by a factor of ≈ 7.8 needs to be carefully considered depending on the application context (see section 3.2.3.3).

However for larger motions involved, 6 DoF joints have shown a clear benefit for the use in the shoulder area for patient 2 undergoing the arms-up arms-down motion. The reasons could be found either in a yet insufficient positioning of the ball and socket joints belonging to the shoulder girdle or in having additional translational motion components within at least one of the corresponding joints. For example Sahara et al. (2006) report on translational components for the distal end of the clavicles, i.e. at the acromioclavicular joints, in anterior-posterior direction of $(-1.9 \pm 1.3$ mm$)$ at $90°$ abduction and $(1.6 \pm 2.7$ mm$)$ at maximum abduction and in superior-inferior direction of $(0.9 \pm 1.9$ mm$)$. As being limited to images of only one patient in arms-up and arms-down posture, further studies need to be carried out focusing on the motion behaviour of the joints in the shoulder area. Despite the small patient cohort examined in this study, results indicate that a refinement of the joint parametrizations in this area is needed in order to achieve an accurate modelling of very large posture changes of the shoulder complex.

Besides the shoulder area, Wu et al. (2002) reported that also the intervertebral joints involve translational motion components, which should be taken into account to compensate for compression or elongation effects of the intervertebral disks (Monheit and Badler 1991). For the image data used in this work, translational motion was especially observed for the intervertebral joints belonging to the cervical spine when using 6 DoF joints during the kinematics-based registration approach (see Figure 47). The translational motion happening at the rotations centres of the intervertebral joints could also be a limitation of the currently used positioning approach. It seems worth to evaluate in future studies if a relocation of the rotation centre towards the centroid of the respective intervertebral disk would yield a better approximation of the joint's true anatomical position. In the current state of the model based registration approach utilizing rotational joints, the cervical vertebrae should not be subject to active optimization. Better results were achieved when those bones adopt their transformation passively through motion propagation along the kinematic chain.

The present study clearly shows that the use of 6 DoF intervertebral joints comes at the cost of an increased computational effort, which would adversely affect the application of the kinematic model in the time-critical radiotherapy context. With 35 minutes, the total time needed to register the whole skeleton in the head and neck area is still too high to consider for online ART, but there is potential to drastically reduce the computation time of the extended simplex downhill based optimizer by exploiting the parallelization capability of modern hardware. Additionally, in order to provide a reasonably low computation time of the kinematic model, the amount of free parameters should be reduced to only considering rotational motion about the three body axes for the intervertebral joints and the atlanto-occipital joint for small motions involved. This effectively reduces the total DoF of the kinematic model. Taking patient 1 with intervertebral joints modelled up to the 6th thoracic vertebra as an example, the DoF are reduced by 39, which in turn results in a speed up factor of > 1.5. This is particular beneficial for the kinematics-based registration approach, in which numerous new postures with the kinematic model need to be calculated for every iteration during the optimization process. By using ball and

socket joints in favour of a faster computation time, the generation of new postures can be performed on an interactive level ($\approx$ 40 ms per posture) while the achievable mean accuracy remains on a high level of within 1 mm. Further potential to reduce the computation time is found for joints like the left and right temporomandibular joints, which both are actually only articulating in one DoF since their rotation angles are synchronized through the connection to the same bones. Here, one DoF hinge joints would by capable to represent the whole range of motion, however associated with the need of additional input of a priori knowledge about the correct axis of rotation.

The use of a kinematic approach to model the articulation of the human skeletal anatomy is widely used in the field of orthopaedics or rehabilitation (Bandara et al. 2017, Kainz et al. 2016). In the context of radiotherapy however, kinematic models had been rarely adopted for modelling deformations in the human anatomy. Vidal and Villard (2016) use a kinematically inspired model for simulating the ribcage motion according to a sinusoidal function. Furthermore, du Bois d'Aische et al. (2007) have developed an articulated model of the spinal column, which is coupled to a finite element elastic model. The model is limited to the vertebral column, while the articulation is realized by rotational motion at the intervertebral joints. As represented by recent literature, biomechanical deformation models for the use in radiotherapy mostly are realized by FEMs based models (Al-Mayah et al. 2010, Zhong et al. 2010) or spring mass models (Neylon et al. 2014). While FEM based models in general are capable of offering highly detailed biomechanical simulations, a trade-off between complexity and computational cost has to be considered. FEM based models used in radiotherapy often rely on a reduced patient geometry (Zhong et al. 2010) with the need of extensive tissue segmentation and a time consuming mesh generation step. For the purpose of modelling the articulation between the bones of the human anatomy, a kinematic approach potentially is much more efficient in calculating different skeletal postures by limiting the computations needed to those arising at the joints in the system under the assumption that bones are considered to remain rigid during transformation.

In contrast to models based on kinematics, dynamic models additionally consider mass properties of rigid bodies and forces, acting on them. Transferring this concept to the human skeleton would mean to take into account forces originating from muscles, which attached to the bones, induce articulation. Although this could enable a more detailed modelling even of the whole musculoskeletal system, current medical applications are limited to specific body sites, for example the upper extremities (Holzbaur et al. 2005). Such an approach would require additional information, for example about force-generating parameters for each included muscle, muscle attachment sites or muscle tendon paths of the individual patient, which need to be extracted from image data and from additional experimental data. Obtaining all these information in an automated way is currently most likely not yet possible. Together with a higher calculation time to process the additional information, dynamic models have the potential to offer more detailed motion modelling, certainly at a markedly higher cost. Due to that, the use of a dynamic model was not considered in this work.

4.2 Mimicking anatomical posture changes

The kinematic model was evaluated based on landmarks, manually defined by multiple observers and distributed on the bones in the head and neck area. High effort was put into defining a large number of distinctive landmarks, covering most of the bones in order

to increase the validity of the verification for the overall accuracy of the kinematic model to reproduce different postures (Brock et al. 2017). This is especially worthwhile for the evaluation of a highly flexible model in which every bone adopts an individual transformation. It is important to mention that the evaluation only applies to points located on or within the bones under the assumption that bones are considered as rigid parts and is not valid for points outside of the skeletal anatomy. As seen in Figure 16, many landmarks are distributed on the bones. However, due to the lack of prominent anatomical features on a few bones like the ribs, less landmarks could be found there than for the other bones. It has to be considered that the landmarks on the ribs are focused on a small area near the costovertebral joints, which means that small deviations in the landmark positions could induce large changes to the transformation of the bone. Overall, a good quality of the defined landmarks across all bones is indicated by the achieved low interobserver variability of $[0.42, 0.38, 0.67]^T$ mm (see section 3.2.2). Small differences in the variability across x, y and z direction can be observed, which is most likely due to a higher slice distance in z compared to x and y. The established set of manually defined landmarks serves as a reference of high quality for the evaluation of the developed kinematic model. Using this set of manually defined landmarks as a reference, the accuracy of the kinematic model in reproducing different postures was assessed for anatomical variations in the range of typical inter-fractional changes in radiotherapy for patient 1, as well as for very large anatomical changes, exemplary shown for patient 2 with an arms-up arms-down posture change (see section 3.2.3.1). For the former, it was shown that the developed kinematic model is capable of accurately mimicking anatomical postures within the range of 0.97 mm, which is only marginally higher than the mean interobserver variation of 0.88 mm. Among the different bones, only very small variations in the accuracy could be found. For patient 2 with the large arms-up arms-down motion however, higher residual errors for the scapulae, clavicles and humeri were observed. Because those bones are directly involved in the arms-up arms-down motion, it seems reasonable to assume that under the effect of large motion, the parametrization of the corresponding joints is not optimal. While the sophisticated positioning methods for the glenohumeral joint as well as for the acromioclavicular joint have shown considerable improvements in terms of the achieved accuracy for those bones compared to the simple nearest neighbour based approach (see Figure 24), it was shown that there is the potential to increase the accuracy even further when replacing the ball and socket joints by 6 DoF joints (see Figures 24b and 26b). This highlights the limitations of the currently used approximation of ball and socket joints in terms of positioning of the rotation centre and the omission of translational components in the joints corresponding to the shoulder area, in case very large anatomical changes are present.

While the approximation of the glenohumeral joints as ball and socket joints is shared by several publications (Garner and Pandy 1999, Veeger 2000, Holzbaur et al. 2005), no commonly prevailing joint type for modelling the sternoclavicular joint connecting the clavicle to the sternum and the acromioclavicular joint can be found in current literature. Both joints are considerably involved in the arm elevation motion (Teece et al. 2008, Ludewig et al. 2009). Besides their approximation with ball and socket joints, especially for the acromioclavicular joint, additional translational motion at the joint is indicated (Sahara et al. 2006, DePalma 1963, Charbonnier et al. 2014). Missing translational motion at the acromioclavicular joints was also found to be a limiting factor for the kinematic model based registration approach for the arms-up arms-down posture, where noticeably better results could be achieved with 6 DoF acromioclavicular joints with associated trans-

lations at the joints of ≈ 8 mm (see section 3.4.2.2). Due to the increase in computation time associated with the use of unconstrained 6 DoF joints, the implementation of more sophisticated joint parametrizations with less than 6 DoF or constrained ranges of motion could potentially lead to a good trade-off between computation time and accuracy when reproducing very large arms-up arms-down postures.

It has to be mentioned that the assessed accuracy only applies to the bony tissue and does not directly correspond to the accuracy within the soft tissue. Nevertheless, the accuracy measured on the bones is very important in order to provide a meaningful initialization for the soft tissue model and thus is considered as a weak indicator for the quality of the soft tissue deformation. While conventional intensity-based transformation models will achieve a similar accuracy when fitting the same observer defined landmarks, this most likely comes at the expense of unrealistic deformations within the whole anatomy, disregarding actual tissue properties. The benefit of having a kinematic model becomes particularly apparent for the case of registering large posture changes (see section 3.3). With the input of only a few landmarks, even the large posture change of the arms-up to the arms-down anatomy can be reproduced in an anthropomorphic manner with the benefit of preserving the rigidity within the bones. Actual skeletal deformations only occur at the position of the joints, by which an anatomically reasonable deformation behaviour is promised. Compared to the widely used intensity based transformation models, a kinematic model for the skeletal anatomy enables the anthropomorphic representation of such large posture changes in the first place.

Moreover, the kinematic model allows for the propagation of motion of individual bones across the attached joints. That means, those bones, which do not receive direct input landmarks will adopt a transformation according to kinematic rules, propagated from the adjacent bones across the joints throughout the kinematic chain. Differences in the achieved accuracy for the passively articulated bones were observed (see section 3.2.4.1). While the clavicles for example can be pretty accurately positioned via their neighbouring bones, higher errors were found for the humeri, hyoid bone and mandible. Since the latter represent leaf elements within the kinematic tree, i.e. they are the most outwards directed elements, which obtain a rigidly propagated transformation from their connected neighbouring bones. Therefore it is of particular importance to include these bones in the set of actively optimized bones for the kinematic model based registration approach.

Besides the bones representing leaf elements in the kinematic tree, two additional factors seem to play an important role to affect the accuracy of the passively articulated bones. On the one hand, only those bones undergoing larger anatomical variations can possibly manifest in larger errors and on the other hand, the quality of the approximation of the joint parametrization seems to correlate with the achievable accuracy. This can be seen in the results for the cervical spinal area, where larger errors can be observed compared to the adjacent thoracic area. As described previously, the approximation of the rotation centres of the intervertebral joints turned out to be not optimal. This effect is amplified by the fact that the cervical vertebrae contribute to a large portion to the total mobility of the spine. Moreover, although the scapulae do not represent leaf elements in the kinematic model, they are associated with relatively large errors when receiving no direct input in form of landmarks. Here, the approximation of the acromioclavicular joints attached to the scapulae as ball and socket joints were found to be non-optimal (see section 3.4.2.2). With occurring translations of ≈ 8 mm at the acromioclavicular joints for the arms-up arms-down posture change combined with the given spatial proximity to the glenohumeral

joint, shared by the scapula, a disregard of translations in the implementation of the joint potentially leads to a deteriorated accuracy of the passively articulated scapula. With a mean accuracy of $\approx$ 1-2 mm for the passively articulated bones in case of typical anatomical variations occurring in the head and neck area during the course of radiotherapy, the accuracy is reasonable. For the kinematic model based registration approach, those bones which were left out are very well pre-positioned. Leaving out two adjacent bones further increases the residual errors to $\approx$ 2-3 mm, which should be carefully considered for the desired application. As expected, larger mean errors were observed for the large arms-up arms-down posture change. Overall, leaving out individual bones in the kinematic model comes with only minor increases in the residual errors, which most likely are the result of current approximations in the joint parametrizations. Taking conventional intensity-based transformation models as examples, the interpolation between input landmarks would lead to non-physical deformations within the bony tissue. The kinematic model however constrains these deformations to only allow for physical transformations even in areas without input landmarks while preserving the rigidity of the bones at any time.

The robustness of transformation models in assessing anatomical variations is crucial in the field of ART. Especially within the scope of online replanning scenarios, the use of current intensity-based DIR methods is infeasible due to their need for manual correction of the resulting transformations. Transformation models based on kinematics on the other hand promise to be more robust due to providing a physically based transformation behaviour and thus preventing the occurrence of unrealistic deformations within the bones and providing a meaningful initialization for the soft tissue deformation model. A typical challenge for landmark based registration approaches is the existence of wrong landmarks, which erroneously map a distinct point on one bone to a point on another bone instead of the same bone, in the other image. This can happen for example in the region of the spine, due to the given high anatomical similarity between some adjacent vertebrae, for either manually or automatically defined landmarks. In an evaluation study, the robustness of the developed kinematic model against such wrong input landmarks, varying in their number, magnitude of violation and affected bones, was evaluated (see section 3.2.4.2). Overall, the kinematic model has shown to maintain a high accuracy despite the existence of such wrong landmarks. Even for five wrong landmarks deviating from their reference position with a violation value of 15 mm, the model remains stable in most of the cases. An increase in the residual errors of approximately 1 mm, 2 mm and 3 mm has to be considered when five wrong landmarks with violation values of 5 mm, 10 mm and 15 mm are present. Wrong landmarks had a greater impact for bones with a smaller number of reference landmarks defined, for example on the ribs. Especially the lower ribs, which are not connected to the sternum due to the limited FoV of the image scan, increased errors were observed. Due to the fact that all landmarks are equally weighted in the developed kinematic model during matching, outlier landmarks only partially contribute to the final transformation. In case there are no landmarks other than the wrong ones defined on one bone, they are considered in their full weight, however always constrained by the overall mobility of the skeleton and the DoF of the adjacent joints.

It has to be noted that it is not the objective of the kinematic model to completely rule out wrong landmarks, rather than to reduce their impact on deformation behaviour as a whole while still providing a meaningful regularization for the transformation of single bones as well as for the whole skeleton. In this regard, the achieved results encourage the use of such a kinematic model for a meaningful regularization of the transformations of the bones in the presence of wrong landmarks. Further refinement of the joints, especially

a reduction of the total DoF as well as a limitation of the range of the rotation angles to match the physiological range of motion, bears the potential to further improve the robustness.

4.3   Automated kinematics-based registration approach

In a proof of concept study, the potential of the kinematic model in a typical registration scenario was demonstrated. For that, a new registration method was developed using the kinematic model as the transformation model together with a similarity metric and an optimization approach (see section 3.4.1). After registration of the skeleton, the soft tissue is adapted accordingly. The similarity metric as a measure of overlapping voxels was chosen in favour of commonly used metrics such as CC or MI. Based on the assumption that bones are rigid and represent distinct shapes, the number of overlapping voxels as a metric has shown to be a good indicator of the quality of the alignment of any two bones. Compared to a typical implementation of a normalized MI, the used metric showed a smoother solution space with considerably less local minima. On the downside, the overlap-based similarity metric is usually more dependent on a good quality of the delineation compared to intensity based methods. As an example, a delineation of a bone smaller than its actual anatomical boundary would induce ambiguity during the matching process since several transformations of that bone would lead to a perfect fit with the maximum number of voxels overlapping. In case delineations of the bones of reasonable quality can be provided, using the number of overlapping voxels as a similarity metric will result in less local minima and thus simplify the overall optimization process. With a simplex downhill approach, a straightforward and robust optimizer was chosen in order to demonstrate the feasibility of the kinematic model based registration approach. The extension of the optimizer in form of disturbance steps successfully contributes to avoiding local minima and achieving global convergence within a reasonable time.

In a hierarchical optimization scheme, pre-selected bones were optimized in a specific order (see section 3.4.1.3). Such an iterative approach was favoured over the optimization of the transformations of all bones simultaneously. Due to the fact that once a bone is successfully registered, the following bones achieve a reasonable pre-registration by propagation of the transformation through the kinematic chain. This effectively reduces the effort for the optimizer when subsequently registering these bones, leading to a faster convergence and an increased robustness. Because the simplex downhill approach in general is a rather simple approach with a moderate convergence speed, a local optimization of individual bones was preferred. As a drawback however, such an approach could be less stable due to the fact that the achievable registration quality of one bone strongly depends on the results of the previous bones. The presence of substantial imaging artifacts in a local area for example could tamper the registration result of one bone and thus lead to failing the registrations for the following bones. To overcome, affected bones could be left out for active optimization and are only articulated through passive transformation by the kinematic model. The study has shown that the optimization of a subset of the bones was enough in order to capture the rough posture of the skeleton represented in the images and thus achieves a meaningful pre-registration of the remaining bones. Followed by a refinement of the skeletal fit through subsequent optimization of additional bones, an accurate skeletal match could be achieved.

As shown in the leave-N-bones-out evaluation (see section 3.2.4.1), those bones representing leaf elements in the kinematic tree are not adequately transformed when only

receiving passive articulation through the joints. They were included in the set of actively optimized bones along with other bones. Among those are very characteristic bones like the scapulae, which are easy to register and other bones with a distance of at least two along the kinematic chain. It turned out that leaving a gap between the actively optimized bones plays an important role, since the impact of the approximation made for the joints on the overall registration result is considerably larger when actively optimizing two adjacent bones. For example after optimizing the 1st thoracic vertebra, a subsequent optimization of the 2nd thoracic vertebra around the position of the joint rotation centre could only achieve good results, if this joint very precisely represents the motion range of the actual anatomical joint. Else, the optimal solution can not be found by the optimizer. This issue is currently mitigated by leaving a gap between two adjacent bones in order to provide space for compensation of non-perfectly approximated joint parametrizations, which in turn also leads to a reduction of the overall registration time. The adverse effect of non-optimal joint approximations for the optimization was in particular observed for the intervertebral joints in the cervical spine. Dumas et al. (1993) pointed out that a majority of 58% of the rotational motion among all cervical vertebrae takes place at the intervertebral joint between the 1st and 2nd cervical vertebrae. This would render the 2nd cervical vertebra to be a good candidate for active optimization, while the other cervical vertebrae would be transformed according to passive articulation. However, due to the current approximation of the positions of the intervertebral joints, the active optimization of this bone did not result in adequate transformations of the cervical spine. Consequently, all cervical vertebrae were not part of the optimization and were only passively articulated through motion propagation within the kinematic model. Future work should focus on improving the approximation of the intervertebral joints, for example by taking into account the centroids of the vertebral bodies instead of the centroids of the whole vertebrae to shift the joint locations more towards the intervertebral disks. The same issue persists with the current approximation of the acromioclavicular joint as a ball and socket joint. For patient 2 with the large arms-up arms-down motion, the registration results showed that it was only possible to achieve an accurate registration of the shoulder area with the acromioclavicular joint allowing for additional translational offsets (see section 3.4.2.2). This puts emphasis on the importance to have a good approximation of the joints' motion range in case very large anatomical variations are present. For the patient undergoing typical inter-fractional changes during radiotherapy, no adverse effects of using 3 DoF acromioclavicular joints could be observed. In the thoracic area, every rib was taken into account for active optimization since their breathing induced motion was not completely compensated after optimization of the sternum and vertebral column. In the current state of the kinematic model, no direct linkage of the individual rib transformations such as through intercostal muscles is considered.

During the registration, the kinematic model inherently preserves the rigidity of the bones and effectively reduces the solution space for the optimization. With such a transformation model, a meaningful initialization for the soft tissue model is guaranteed. Resulting in a measured residual error on the bones of about 1.45 mm averaged over all examined fractions of patient 1, the kinematic model based registration provides an overall accurate assessment of the anatomical variations. Even for patient 2, a reasonable approximation of the posture despite the large variation involved in the arms-up arms-down motion could be achieved. It is important to mention that the achieved accuracy on the bones can not be assumed to be the same for the OARs or the irradiated target itself, since they are mostly located within the soft tissue. Future studies need to invest-

igate the role of the soft tissue model in propagating the skeletal transformations and its impact on the accuracy within those critical structures, relevant for radiotherapy. The overall calculation time needed to register the whole skeletal posture took approximately 35 minutes, which is considered too long for the use in an online adaptive scenario. While the kinematic model is able to calculate posture changes as fast as 40 ms, major potential to speed-up the calculation time can be seen in tweaking the current simplex downhill optimization. In future studies, efforts should be taken to improve the runtime of the registration procedure either by weakening the convergence criteria, making use of parallelization techniques or by replacing the optimizer with one following a more efficient optimization strategy that allows for a faster convergence.

Efforts to preserve the rigidity of the bony anatomy during DIR were made among various contributions in recent literature. Approaches extending conventional intensity-based registration algorithms by imposing additional local rigidity terms as a soft penalty (Greene et al. 2009) or a hard penalty (Kim et al. 2013, König et al. 2016) exist, as well as recent biomechanical models, enriched with rigid elements (Al-Mayah et al. 2010, Kim et al. 2016, Neylon et al. 2014). While selected bones of the head and neck area in the approaches of Al-Mayah et al. (2010) and Neylon et al. (2014) are included as separate, unconnected structures, Kim et al. (2013) went one step further and mechanically connect the skull, cervical vertebrae, and mandible within a FEM based approach in order to achieve a realistic posture generation. Kinematics based approaches are rarely found for registration tasks in radiotherapy. The feasibility of a registration approach based on kinematics is demonstrated by du Bois d'Aische et al. (2007) for the cranial area of the spinal column with the MI as the similarity metric and a linear elastic model for the soft tissue. Three DoF joints are manually positioned between the vertebrae and every individual vertebra is subsequently aligned with its representation in the images. In contrast, the kinematic model developed in this work is not limited to the cervical spine but extended to the whole head and neck area by involving all bones contributing to the skeletal posture of the patient in this region. Particularly with regard to proton therapy, an accurate assessment of the variations in the skeletal anatomy will become crucial. The automated approach to position the joints based on the geometry of the bones saves additional resources, which would need to be allocated otherwise for every joint and patient. Although it is necessary to further test the kinematic model on a larger patient cohort in the future, encouraging results regarding accuracy and robustness could be demonstrated in a proof of principle study.

4.4 Kinematic model in radiotherapy applications

Different radiotherapy applications impose different requirements on the transformation model. In its current state, the developed biomechanical model could be used for the generation of different anthropomorphic postures of a patient in a quality assurance scenario for the validation of the DIR methods, implemented in the current treatment planning systems. While simple physical phantoms are still in use to validate the accuracy of registration methods, digital phantoms provide a way to approximate anatomically correct deformations of the patient's anatomy. The current anatomy of a patient represented in an image can be artificially deformed for example with the software *InSimQA* (In-SimQA, Oncology Systems Limited, Shrewsbury, UK), by providing supporting points for the internal spline-based transformation model. Knowing that such a mathematical transformation model does not take into account different tissue types, unrealistic deformations

for example within the bony tissue cannot be excluded. Using a biomechanical model, as developed in this work, however guarantees a preservation of rigidity within the bones and additionally provides a more easy way to generate different postures of the patient by the underlying interconnected skeletal anatomy. Less user input is required in order to control the kinematic model to mimic different postures and the model based approach even enables the generation of very large posture changes of reasonable quality (Teske et al. 2017a). Current limitations are the requirement of delineations of the bones prior construction, as well as the strong focus on generated postures, merely induced by changes of the underlying skeleton. However, such a biomechanically driven approach represents the first step towards the approximation of anthropomorphic anatomical changes of a high level of biofidelity including soft tissue mechanics. Considering the potential benefits of such a biomechanical model, its use may help to speed up the dissemination of DIR into clinical applications. The possibility to generate different postures of the individual patient anatomy is also highly beneficial for the creation of a posture library in a plan-of-the-day approach. Besides the generation of realistic typical inter-fractional changes, additional cases could be covered, for example the consideration of alternative postures during irradiation. This could matter for example if the current health condition of a patient denies the positioning in an arms-up posture before and during treatment. Being considered in the plan library, backup plans with arms-down postures could be provided without the necessity to acquire additional images.

Future applications of the presented biomechanical based registration approach can also be found in conventional IGRT. As presented by Stoiber et al. (2014), DIR in general can be used to take into account tissue deformations in order to obtain an improved correction vector for the treatment couch during positioning. A biomechanical registration approach has the potential to further increase the reliability of the obtained correction vector by providing a more realistic deformation assessment. Since the DVF generated by the biomechanical model in this application only represents an intermediate result, which is immediately reduced to a single vector, the potential benefit is rather marginal for such application. A much higher benefit is expected in the context of ART, in which the full DVF is taken into account. Especially within the highly flexible head and neck area, frequently occurring skeletal changes induce deformations in the surrounding anatomy. The use of a biomechanical model can help to provide an anthropomorphic representation of the posture changes while taking into account the different tissue properties, such as the rigid transformation behaviour of bones. In contrast to conventional DIR methods showing deficiencies in regions with homogeneous intensity distributions (Juang et al. 2013, Kirby et al. 2011) in CT to CT or CT to cone-beam CT cases, a biomechanical based registration approach is able to provide a voxel-wise reasonable DVF to overcome this issue.

In an adaptive replanning scenario, biomechanical models promise to provide physically meaningful DVFs, which have the potential to improve the quality of contour propagation and dose mapping between the planning image and the fraction image. This could enable more accurate estimates for the delivered dose at every treatment fraction. Regarding the computation time required by the developed kinematic model based registration approach in its current state, rather offline replanning scenarios qualify as potential applications. In scenarios to adapt the treatment plan at every fraction while the patient remains on the treatment table, further improvements regarding a more efficient optimization are required. With the kinematic model, a fast and robust transformation model for the skeletal anatomy is provided. With the robustness becoming one of the key requirements for the automation of the plan adaptation process, the kinematic model is able to guarantee

physically meaningful transformations to a certain degree. Possible improvements such as imposing limitations on the rotation angles to only represent the physiological range of motion are expected to further improve the robustness and biofidelity of the model.

Following the current trend towards MRI guided radiotherapy, a biomechanical model of the patient anatomy further bears high potential, for example to assess and compensate for inhomogeneity in the magnetic field or to improve multi-modal registration. Beyond ART, the biomechanical model could also add value for retrospective outcome analyses. The fact that images often are acquired at multiple institutions with different treatment machines without sharing a common imaging protocol, large changes in the anatomy of the patient are to be expected. The capability of the developed biomechanical model to register even large posture changes in a reasonable way would help to reduce the manual workload and increase the rate of automation.

In the head and neck area, the complex interplay between different bones induce posture changes and thus lead to anatomical deformations within the whole region. Based on the assumption that it is the skeletal anatomy, which mainly contributes to anatomical variations, the idea of propagating skeletal transformations into the soft tissue is highly appropriate in this area. For other areas like in the abdomen, skeletal motion is not considered to be the main motion inducing source, apart from positional changes in the spine. Here, breathing motion or peristalsis should be considered as contributors to occurring deformations. Such information can currently only be used as an additional input for the kinematic model. Due to the low number of bones existing in the abdominal region, more emphasis is put on the soft tissue model in order to assess meaningful deformations, while the skeletal fit of the posture merely serves as a pre-registration and rough initialization for the soft tissue model.

Especially with regard to the high number of emerging proton therapy centres over the past years worldwide, state of the art high precision radiation treatment is technically feasible and becomes available for treatment of more and more tumor entities. The rise of the technically feasible precision is always associated with an increased demand for an improved assessment of anatomical variations throughout the treatment process in order to guarantee the highest benefit for the treatment of the patient. With the developed biomechanical model, the first step towards an accurate and robust in-silico deformation model of the patient anatomy was taken.

Chapter 5

Summary

In modern high precision radiotherapy, changes in the anatomy of the patient over the course of treatment pose a major challenge. An accurate assessment of occurring anatomical variations is the key requirement to enable an adaptation of the treatment plan for ensuring a highly precise treatment. Comparison of commonly used deformable image registration shows large discrepancies regarding the quality of anatomical alignment, benchmarked on a common data pool. One of the main reasons is found in widely used transformation models, insufficiently reflecting the actual deformation behaviour of the underlying tissue. Thus, especially in the highly heterogeneous head and neck area, which is characterized by many organs at risk being in proximity to the tumor as well as posture changes induced by the interplay of several bones, an accurate assessment of anatomical changes is essential for a successful adaptive radiotherapy. A physically meaningful transformation model offering a high biofidelity is required to provide an accurate anatomical alignment in such area. In this work, a novel biomechanical deformation model based on kinematics and multi-body physics for the whole head and neck area is introduced to guarantee the representation of physically meaningful transformations.

The developed kinematic model is individually tailored to each patient as it is based on the delineated bones extracted from the computer tomography scan. It encompasses all bones relevant for head and neck cancer treatment, including bones of the proximal upper extremities, the shoulder girdle, cranial region, the rib cage and the vertebral column. Moreover, the model is designed to be easily extendible to other body regions. All bones are connected by ball and socket joints, which are automatically localized based on their individual geometries. A kinematic graph maintains the hierarchy of the connected bones across the whole skeleton to enable the propagation of local transformations to other body regions by inverse kinematics. Accuracy, robustness and computational efficiency of the kinematic model were retrospectively evaluated on patient datasets representative for typical inter-fractional variations as well as separately acquired image scans with large arms-up to arms-down posture changes. Using landmarks defined by multiple observers as reference, the overall mean accuracy of the kinematic model in reproducing postures in the image scans was found to be around 1 millimetre, which is settled slightly above the inter-observer variation. In detail, the assessed accuracy revealed potential for improvement regarding the automated positioning of the intervertebral joints in the region of the cervical spine. Due to the complex shape of the vertebrae, a relocation of the joint rotation centres towards the line connecting the centres of the intervertebral disks seems beneficial. Moreover, the use of ball and socket joints for the acromioclavicular joints has shown to be insufficient for mimicking the large arms-up to arms-down posture change due to

the lack of representing translational offsets, observed in the image scans. The strong regularization of the permissible deformations in the skeletal anatomy leads to a higher robustness against conflicting input such as flawed or mixed-up anatomical feature points. Furthermore, such a physical-object-oriented transformation model requires even less input to describe meaningful deformations. With the total degrees of freedom of the kinematic head and neck model limited to those specified by the joints, the computation of new arbitrary skeletal postures is achieved within less than 50 milliseconds.

With such efficient computation on the one hand and the strong regularization of deformations on the other hand, the kinematic model seems suitable for its application in a registration approach. In addition, it was demonstrated how the kinematic model can be successfully embedded into a registration approach as a transformation model to enable the fully automatic extraction of anatomical variations from image scans. This was accomplished by coupling the model to an extended simplex downhill optimizer and an overlap based similarity metric. The anatomy of pre-selected bones is aligned following a hierarchical optimization scheme.

In conclusion, the novel developed kinematic model guarantees a deformation modelling of high biofidelity and efficiency, thus promising an assessment of anatomical changes without the need of an extensive visual inspection of the results as otherwise expected. To date, successful application of adaptive radiotherapy especially for tumors in regions characterized by a high anatomical flexibility is hampered by a lacking reliability of conventional deformation models. While associated uncertainties can be compensated at the cost of extended safety margins for photon therapy, prevailing range uncertainties when using particles currently impede the treatment of tumors in such areas. The dissemination of the proposed kinematic deformation model into the clinics provides a way to lay the foundation towards broadening the spectrum of patients eligible for treatment with particles, carried out at the increasing number of particle therapy centres worldwide.

Zusammenfassung

In der modernen Hochpräzisions-Strahlentherapie stellen Veränderungen in der Anatomie des Patienten während des Behandlungsverlaufs eine wesentliche Herausforderung dar. Die akkurate Quantifizierung von auftretenden anatomischen Veränderungen ist eine maßgebliche Voraussetzung für eine Adaptierung des Behandlungsplans zur Gewährleistung einer hochpräzisen Bestrahlung. Vergleichsstudien zu häufig benutzten elastischen Registrierungsverfahren auf einem gemeinsamen Datenpool zeigen deutliche Diskrepanzen bezüglich der erreichten anatomischen Übereinstimmung nach der Registrierung. Einer der Hauptgründe wird in den herkömmlich benutzten Transformationsmodellen gesehen, die das Deformationsverhalten von zugrunde liegenden Gewebetypen nur unzureichend widerspiegeln. Daher gilt besonders in der stark heterogenen Kopf-Hals Region, die durch viele Risikoorgane in unmittelbarer Umgebung der Tumore geprägt ist, und Verformungen der Patientenanatomie durch das Zusammenspiel vieler Knochen erfährt, dass eine genaue Erfassung der anatomischen Veränderungen essentiell ist für den Erfolg einer adaptiven Strahlentherapie. Es wird ein physikalisch sinnvolles Transformationsmodell von hoher biofidelity benötigt, um selbst in solchen Regionen eine akkurate Übereinstimmung der Anatomie zu erreichen. In dieser Arbeit wird ein neuartiges biomechanisches Deformationsmodell basierend auf Kinematik und Mehrkörperphysik für den gesamten Kopf-Hals Bereich vorgestellt, das die Abbildung physikalisch sinnvoller Transformationen garantiert.

Das entwickelte kinematische Modell kann auf jeden individuellen Patienten zugeschnitten werden, da es auf den Segmentierungen der Knochen, die aus der Computertomographie extrahiert werden, basiert. Es erstreckt sich über alle für die Behandlung von Kopf-Hals Tumoren relevanten Knochen, einschließlich derer in den proximalen oberen Extremitäten, des Schultergürtels, der kranialen Region, des Brustkorbs sowie der Wirbelsäule. Darüber hinaus ist das Modell so konzipiert worden, dass eine einfache Erweiterbarkeit auf andere Köperregionen jederzeit gegeben ist. Die Knochen sind über Kugelgelenke miteinander verbunden, welche über Informationen der individuellen Knochengeometrie automatisch lokalisiert werden können. Ein kinematischer Graph bildet die Hierarchie aller verbundenen Knochen im gesamten Skelett ab, um eine Propagation lokaler Transformationen in andere Körperregionen mittels inverser Kinematik zu ermöglichen. Genauigkeit, Robustheit und Berechnungsgeschwindigkeit wurden auf Patientendatensätzen retrospektiv evaluiert, die zum einen typische interfraktionelle Bewegungen aufweisen, als auch auf separat aufgenommenen Daten, die Änderungen in der Haltung eines Patienten, verursacht durch große Armbewegungen, abbilden. Im Vergleich zu manuell von mehreren Experten bestimmten Landmarken wurde die gesamt erreichte Genauigkeit des kinematischen Modells in der Nachahmung/Nachbildung der in den Bildaufnahmen enthaltenden unterschiedlichen Patientenhaltungen von ungefähr 1 Millimeter festgestellt, welche sich leicht über der interobserver-Variabilität ansiedelt. Im Einzelnen zeigte sich anhand der ermittelten Genauigkeit in Bezug auf die automatisierte Positionierung der

Zwischenwirbelgelenke im Gebiet der Wirbelsäule ein Verbesserungspotenzial. Aufgrund der komplexen Form der Wirbelkörper scheint eine Verschiebung der Rotationspunkte der Gelenke in Richtung der Linie, die die Bandscheiben untereinander verbindet, vorteilhaft. Darüber hinaus zeigte sich die Verwendung von Kugelgelenken zur Repräsentation der Schultereckgelenke aufgrund fehlender Translationsfreiheitsgrade als unzureichend bei der Nachahmung der durch große Armbewegungen verursachten Änderung der Patientenhaltung in den Bildaufnahmen. Die starke Regularisierung der zulässigen Deformationen in der skelettalen Anatomie führt zu einer gesteigerten Robustheit gegenüber widersprüchlichem Input in Form mangelbehafteter oder fälschlicherweise vertauschter Landmarken. Weitergehend benötigt solch ein objektorientiertes physikalisches Transformationsmodell sogar weniger Input zur Beschreibung sinnvoller Deformationen. Durch die Einschränkung des Modells auf die Freiheitsgrade der Gelenke wird eine Berechnungszeit von neuen beliebigen skelettalen Haltungen innerhalb von weniger als 50 Millisekunden erreicht.

Durch die einerseits effiziente Berechnung und der andererseits starken Regularisierung von Deformationen zeigt sich das kinematische Modell als geeignet, um in einem Registrierungskontext eingesetzt zu werden. Im Weiteren wurde gezeigt, wie das kinematische Modell als Transformationsmodell erfolgreich in einen Registrierungsansatz eingebettet werden kann, um so eine vollautomatisierte Extraktion der anatomischen Veränderungen aus den Bilddaten zu ermöglichen. Dies wurde durch die Ankopplung des Modells an einen erweiterten Simplex-Downhill Optimierer und einer Ähnlichkeitsmetrik basierend auf dem Maß der Überlappung erreicht. Ein hierarchisches Optimierungsschema wurde eingeführt.

Zusammenfassend garantiert das entwickelte neuartige kinematische Modell eine effiziente Deformationsmodellierung mit hoher biofidelity, die eine Quantifizierung anatomischer Veränderungen ohne eine aufwändige visuelle Kontrolle der Ergebnisse verspricht. Bislang ist die erfolgreiche Anwendung der adaptiven Strahlentherapie besonders bei Tumoren in bewegungsstarken Regionen durch die mangelhafte Zuverlässigkeit der herkömmlichen Deformationsmodelle stark eingeschränkt. Während die damit assoziierten Unsicherheiten durch erweiterte Sicherheitssäume in der Behandlung mit Photonen erkauft werden können, verhindern die bei Partikelbestrahlung vorherrschenden Reichweitenunsicherheiten die Behandlung von Tumoren in solchen Regionen. Die Translation des vorgestellten kinematischen Deformationsmodells in die klinische Anwendung stellt das Fundament dar, das Spektrum der für Partikelbestrahlung infrage kommenden Patienten zu vergrößern, die an den weltweit wachsenden Partikelstrahlzentren behandelt werden.

Bibliography

Ahn, P. H., Chen, C.-C., Ahn, A. I., Hong, L., Scripes, P. G., Shen, J., Lee, C.-C., Miller, E., Kalnicki, S., and Garg, M. K. (2011). **Adaptive Planning in Intensity-Modulated Radiation Therapy for Head and Neck Cancers: Single-Institution Experience and Clinical Implications**. Int J Radiat Oncol Biol Phys, *80(3)*, 677–685.

Al Mayah, A. (2018). **Biomechanics of Soft Tissues: Principles and Applications.** CRC Press, Boca Raton, Florida, USA.

Al-Mayah, A., Moseley, J., Hunter, S., and Brock, K. (2015). **Radiation Dose Response Simulation for Biomechanical-Based Deformable Image Registration of Head and Neck Cancer Treatment**. Phys Med Biol, *60(21)*, 8481–8489.

Al-Mayah, A., Moseley, J., Hunter, S., Velec, M., Chau, L., Breen, S., and Brock, K. (2010). **Biomechanical-Based Image Registration for Head and Neck Radiation Treatment**. Phys Med Biol, *55(21)*, 6491–6500.

Albertini, F., Bolsi, A., Lomax, A. J., Rutz, H. P., Timmerman, B., and Goitein, G. (2008). **Sensitivity of Intensity Modulated Proton Therapy Plans to Changes in Patient Weight**. Radiother Oncol, *86(2)*, 187–194.

Alvarez-Moret, J., Pohl, F., Koelbl, O., and Dobler, B. (2010). **Evaluation of Volumetric Modulated Arc Therapy (VMAT) with Oncentra MasterPlan® for the Treatment of Head and Neck Cancer**. Radiat Oncol, *5(1)*, 110.

Amelio, D., Winter, M., Habermehl, D., Jäkel, O., Debus, J., and Combs, S. E. (2013). **Analysis of Inter- and Intrafraction Accuracy of a Commercial Thermoplastic Mask System Used for Image-Guided Particle Radiation Therapy**. J Radiat Res, *54(Suppl 1)*, i69–i76.

Andronache, A., Cattin, P., and Székely, G. (2006). **Local Intensity Mapping for Hierarchical Non-Rigid Registration of Multi-Modal Images Using the Cross-Correlation Coefficient**. In: WBIR 2006: Biomedical Image Registration, volume 4057 of Lecture Notes in Computer Science, pages 26–33. Springer, Berlin, Heidelberg.

Bandara, D. S. V., Gopura, R. a. R. C., Hemapala, K. T. M. U., and Kiguchi, K. (2017). **Development of a Multi-DoF Transhumeral Robotic Arm Prosthesis**. Med Eng Phys, 48, 131–141.

Bartelheimer, K., Teske, H., Bendl, R., and Giske, K. (2017). **Tissue-Specific Transformation Model for CT-Images**. Current Directions in Biomedical Engineering, *3(2)*, 525–528.

Ben-Israel, A. and Greville, T. N. E. (2003). **Generalized Inverses Theory and Applications**. 2. Springer, New York.

Bendl, R., Hoess, A., and Schlegel, W. (1995). **Virtual Simulation in Radiotherapy Planning**. In: Computer Vision, Virtual Reality and Robotics in Medicine, volume 905 of Lecture Notes in Computer Science, pages 287–292. Springer, Berlin, Heidelberg.

Bert, C. and Durante, M. (2011). **Motion in Radiotherapy: Particle Therapy**. Phys Med Biol, *56(16)*, R113–144.

Bhatnagar, P., Subesinghe, M., Patel, C., Prestwich, R., and Scarsbrook, A. F. (2013). **Functional Imaging for Radiation Treatment Planning, Response Assessment, and Adaptive Therapy in Head and Neck Cancer**. Radiographics, *33(7)*, 1909–1929.

Boda-Heggemann, J., Knopf, A.-C., Simeonova-Chergou, A., Wertz, H., Stieler, F., Jahnke, A., Jahnke, L., Fleckenstein, J., Vogel, L., Arns, A., Blessing, M., Wenz, F., and Lohr, F. (2016). **Deep Inspiration Breath Hold—Based Radiation Therapy: A Clinical Review**. Int J Radiat Oncol Biol Phys, *94(3)*, 478–492.

Bookstein, F. L. (1989). **Principal Warps: Thin-Plate Splines and the Decomposition of Deformations**. IEEE Trans Pattern Anal Mach Intell, *11(6)*, 567–585.

Bortfeld, T., Jokivarsi, K., Goitein, M., Kung, J., and Jiang, S. B. (2002). **Effects of Intra-Fraction Motion on IMRT Dose Delivery: Statistical Analysis and Simulation**. Phys Med Biol, *47(13)*, 2203–2220.

Bosch, W. R., Straube, W. L., Matthews, J. W., and Purdy, J. A. (2015). **Data From Head-Neck_Cetuximab. The Cancer Imaging Archive**. DOI: 10.7937/K9/TCIA.2015.7AKGJUPZ.

Bouilhol, G., Ayadi, M., Rit, S., Thengumpallil, S., Schaerer, J., Vandemeulebroucke, J., Claude, L., and Sarrut, D. (2013). **Is Abdominal Compression Useful in Lung Stereotactic Body Radiation Therapy? A 4DCT and Dosimetric Lobe-Dependent Study**. Phys Med, *29(4)*, 333–340.

Brock, K. K. (2010). **Results of a Multi-Institution Deformable Registration Accuracy Study (MIDRAS)**. Int J Radiat Oncol Biol Phys, *76(2)*, 583–596.

Brock, K. K., Mutic, S., McNutt, T. R., Li, H., and Kessler, M. L. (2017). **Use of Image Registration and Fusion Algorithms and Techniques in Radiotherapy: Report of the AAPM Radiation Therapy Committee Task Group No. 132**. Med. Phys., *44(7)*, e43–e76.

Buss, S. R. (2004). **Introduction to Inverse Kinematics with Jacobian Transpose, Pseudoinverse and Damped Least Squares Methods**. Technical report, Department of Mathematics, University of California, San Diego.

Carabe-Fernandez, A., Dale, R. G., Hopewell, J. W., Jones, B., and Paganetti, H. (2010). **Fractionation Effects in Particle Radiotherapy: Implications for Hypo-Fractionation Regimes**. Phys Med Biol, *55(19)*, 5685–5700.

Carmo, A., Kleiner, A., da Costa, P. L., and Barros, R. (2012). **Three-Dimensional Kinematic Analysis of Upper and Lower Limb Motion during Gait of Post-Stroke Patients**. Braz J Med Biol Res, *45(6)*, 537–545.

Castillo, R., Castillo, E., Guerra, R., Johnson, V. E., McPhail, T., Garg, A. K., and Guerrero, T. (2009). **A Framework for Evaluation of Deformable Image Registration Spatial Accuracy Using Large Landmark Point Sets**. Phys Med Biol, *54(7)*, 1849–1870.

Chai, X., van Herk, M., Kamer, V. D., B, J., Hulshof, M. C. C. M., Remeijer, P., Lotz, H. T., and Bel, A. (2011). **Finite Element Based Bladder Modeling for Image-guided Radiotherapy of Bladder Cancer**. Med Phys, *38(1)*, 142–150.

Chao, E. Y. S. and Lim, J. (2013). **Virtual Interactive Musculoskeletal System (VIMS) in Orthopaedic Translational Research**. J Orthop Surg Res, *1(1)*, 25–40.

Charbonnier, C., Chagué, S., Kolo, F. C., Chow, J. C. K., and Lädermann, A. (2014). **A Patient-Specific Measurement Technique to Model Shoulder Joint Kinematics**. Orthop Traumatol Surg Res, *100(7)*, 715–719.

Chelouah, R. and Siarry, P. (2005). **A Hybrid Method Combining Continuous Tabu Search and Nelder–Mead Simplex Algorithms for the Global Optimization of Multiminima Functions**. Eur J Oper Res, *161(3)*, 636–654.

Chen, A. M., Daly, M. E., Cui, J., Mathai, M., Benedict, S., and Purdy, J. A. (2014a). **Clinical Outcomes among Patients with Head and Neck Cancer Treated by Intensity-Modulated Radiotherapy with and without Adaptive Replanning**. Head Neck, *36(11)*, 1541–1546.

Chen, A. M., Yu, Y., Daly, M. E., Farwell, D. G., Benedict, S. H., and Purdy, J. A. (2014b). **Long-term Experience with Reduced Planning Target Volume Margins and Intensity-modulated Radiotherapy with Daily Image-guidance for Head and Neck Cancer**. Head & Neck, *36(12)*, 1766–1772.

Chen, V. E., Gillespie, E. F., Manger, R. P., Skerritt, L. A., Tran, J. H., Proudfoot, J. A., Sherer, M. V., Einck, J. P., Mell, L. K., Moore, K. L., and Yashar, C. M. (2018). **The Impact of Daily Bladder Filling on Small Bowel Dose for Intensity Modulated Radiation Therapy for Cervical Cancer**. Med Dosim, *(in press)*.

Chen, W., Gemmel, A., and Rietzel, E. (2013). **A Patient-Specific Planning Target Volume Used in 'Plan of the Day' Adaptation for Interfractional Motion Mitigation**. J Radiat Res, *54(Suppl 1)*, i82–i90.

Clark, K., Vendt, B., Smith, K., Freymann, J., Kirby, J., Koppel, P., Moore, S., Phillips, S., Maffitt, D., Pringle, M., Tarbox, L., and Prior, F. (2013). **The Cancer Imaging Archive (TCIA): Maintaining and Operating a Public Information Repository**. J Digit Imaging, *26(6)*, 1045–1057.

Colvill, E., Booth, J., Nill, S., Fast, M., Bedford, J., Oelfke, U., Nakamura, M., Poulsen, P., Worm, E., Hansen, R., Ravkilde, T., Rydhög, J. S., Pommer, T., af Rosenschold, P. M., Lang, S., Guckenberger, M., Groh, C., Herrmann, C., Verellen, D., Poels, K.,

Wang, L., Hadsell, M., Sothmann, T., Blanck, O., and Keall, P. (2016). **A Dosimetric Comparison of Real-Time Adaptive and Non-Adaptive Radiotherapy: A Multi-Institutional Study Encompassing Robotic, Gimbaled, Multileaf Collimator and Couch Tracking**. Radiother Oncol, *119(1)*, 159–165.

Crum, W. R., Hartkens, T., and Hill, D. L. G. (2004). **Non-Rigid Image Registration: Theory and Practice**. Br J Radiol, *77(suppl_2)*, S140–S153.

Crum, W. R., Tanner, C., and Hawkes, D. J. (2005). **Anisotropic Multi-Scale Fluid Registration: Evaluation in Magnetic Resonance Breast Imaging**. Phys Med Biol, *50(21)*, 5153.

Dawson, L. A. and Sharpe, M. B. (2006). **Image-Guided Radiotherapy: Rationale, Benefits, and Limitations**. Lancet Oncol, *7(10)*, 848–858.

de Crevoisier, R., Kuban, D., and Lefkopoulos, D. (2006). **Image-Guided Radiotherapy by in-Room CT-Linear Accelerator Combination**. Cancer Radiother, *10(5)*, 245–251.

DePalma, A. F. (1963). **Surgical Anatomy of Acromioclavicular and Sternoclavicular Joints**. Surg Clin North Am, *43(6)*, 1541–1550.

Depauw, N., Batin, E., Daartz, J., Rosenfeld, A., Adams, J., Kooy, H., MacDonald, S., and Lu, H.-M. (2015). **A Novel Approach to Postmastectomy Radiation Therapy Using Scanned Proton Beams**. Int J Radiat Oncol Biol Phys, *91(2)*, 427–434.

Dey, T. K. and Zhao, W. (2004). **Approximate Medial Axis as a Voronoi Subcomplex**. Computer-Aided Design, *36(2)*, 195–202.

Dice, L. R. (1945). **Measures of the Amount of Ecologic Association Between Species**. Ecology, *26(3)*, 297–302.

Dirix, P. and Nuyts, S. (2010). **Evidence-Based Organ-Sparing Radiotherapy in Head and Neck Cancer**. Lancet Oncol, *11(1)*, 85–91.

du Bois d'Aische, A., De Craene, M., Geets, X., Grégoire, V., Macq, B., and Warfield, S. K. (2007). **Estimation of the Deformations Induced by Articulated Bodies: Registration of the Spinal Column**. Biomed Signal Process Control, *2(1)*, 16–24.

Dumas, J. L., Sainte Rose, M., Dreyfus, P., Goldlust, D., and Chevrel, J. P. (1993). **Rotation of the Cervical Spinal Column: A Computed Tomography in Vivo Study**. Surg Radiol Anat, *15(4)*, 333–339.

Egorov, V. I., Schastlivtsev, I. V., Prut, E. V., Baranov, A. O., and Turusov, R. A. (2002). **Mechanical Properties of the Human Gastrointestinal Tract**. J Biomech, *35(10)*, 1417–1425.

Ehrgott, M., Güler, Ç., Hamacher, H. W., and Shao, L. (2010). **Mathematical Optimization in Intensity Modulated Radiation Therapy**. Ann Oper Res, *175(1)*, 309–365.

Ehrhardt, J., Werner, R., Säring, D., Frenzel, T., Lu, W., Low, D., and Handels, H. (2007). **An Optical Flow Based Method for Improved Reconstruction of 4D CT Data Sets Acquired during Free Breathing**. Med Phys, *34(2)*, 711–721.

Eich, E. (1993). **Convergence Results for a Coordinate Projection Method Applied to Mechanical Systems with Algebraic Constraints**. SIAM J Numer Anal, *30(5)*, 1467–1482.

Featherstone, R. (2008). **Rigid Body Dynamics Algorithms**. Springer, New York.

Fedorov, A., Beichel, R., Kalpathy-Cramer, J., Finet, J., Fillion-Robin, J.-C., Pujol, S., Bauer, C., Jennings, D., Fennessy, F., Sonka, M., Buatti, J., Aylward, S., Miller, J. V., Pieper, S., and Kikinis, R. (2012). **3D Slicer as an Image Computing Platform for the Quantitative Imaging Network**. Magn Reson Imaging, *30(9)*, 1323–1341.

Feng, F. Y., Kim, H. M., Lyden, T. H., Haxer, M. J., Worden, F. P., Feng, M., Moyer, J. S., Prince, M. E., Carey, T. E., Wolf, G. T., Bradford, C. R., Chepeha, D. B., and Eisbruch, A. (2010). **Intensity-Modulated Chemoradiotherapy Aiming to Reduce Dysphagia in Patients With Oropharyngeal Cancer: Clinical and Functional Results**. J Clin Oncol, *28(16)*, 2732–2738.

Feng, M. and Eisbruch, A. (2007). **Future Issues in Highly Conformal Radiotherapy for Head and Neck Cancer**. J Clin Oncol, *25(8)*, 1009–1013.

Fitzpatrick, J. M. and West, J. B. (2001). **The Distribution of Target Registration Error in Rigid-Body Point-Based Registration**. IEEE Trans Med Imaging, *20(9)*, 917–927.

Fu, Y., Liu, S., Li, H. H., and Yang, D. (2017). **Automatic and Hierarchical Segmentation of the Human Skeleton in CT Images**. Physics in Medicine and Biology, *62(7)*, 2812–2833.

Garner, B. A. and Pandy, M. G. (1999). **A Kinematic Model of the Upper Limb Based on the Visible Human Project (VHP) Image Dataset**. Comput Methods Biomech Biomed Engin, *2(2)*, 107–124.

Gevaert, T., Verellen, D., Engels, B., Depuydt, T., Heuninckx, K., Tournel, K., Duchateau, M., Reynders, T., and Ridder, M. D. (2012a). **Clinical Evaluation of a Robotic 6-Degree of Freedom Treatment Couch for Frameless Radiosurgery**. Int J Radiat Oncol Biol Phys, *83(1)*, 467–474.

Gevaert, T., Verellen, D., Tournel, K., Linthout, N., Bral, S., Engels, B., Collen, C., Depuydt, T., Duchateau, M., Reynders, T., Storme, G., and Ridder, M. D. (2012b). **Setup Accuracy of the Novalis ExacTrac 6DOF System for Frameless Radiosurgery**. Int J Radiat Oncol Biol Phys, *82(5)*, 1627–1635.

Gibson, S. F. (1997). **3D Chainmail: A Fast Algorithm for Deforming Volumetric Objects**. In: Proceedings of the 1997 Symposium on Interactive 3D Graphics, I3D '97, pages 149–ff., New York, NY, USA. ACM.

Gilbeau, L., Octave-Prignot, M., Loncol, T., Renard, L., Scalliet, P., and Grégoire, V. (2001). **Comparison of Setup Accuracy of Three Different Thermoplastic Masks for the Treatment of Brain and Head and Neck Tumors**. Radiother Oncol, *58(2)*, 155–162.

Girard, M. and Maciejewski, A. A. (1985). **Computational Modeling for the Computer Animation of Legged Figures**. In: Proceedings of the 12th Annual Conference on Computer Graphics and Interactive Techniques, SIGGRAPH '85, pages 263–270, New York, NY, USA. ACM.

Góra, J., Kuess, P., Stock, M., Andrzejewski, P., Knäusl, B., Paskeviciute, B., Altorjai, G., and Georg, D. (2015). **ART for Head and Neck Patients: On the Difference between VMAT and IMPT**. Acta Oncol, *54(8)*, 1166–1174.

Gorthi, S., Duay, V., Bresson, X., Cuadra, M. B., Castro, F. J. S., Pollo, C., Allal, A. S., and Thiran, J.-P. (2011). **Active Deformation Fields: Dense Deformation Field Estimation for Atlas-Based Segmentation Using the Active Contour Framework**. Med Image Anal, *15(6)*, 787–800.

Greene, W., Chelikani, S., Purushothaman, K., Knisely, J., Chen, Z., Papademetris, X., Staib, L., and Duncan, J. (2009). **Constrained Non-Rigid Registration for Use in Image-Guided Adaptive Radiotherapy**. Med Image Anal, *13(5)*, 809–817.

Hafeez, S., McDonald, F., Lalondrelle, S., McNair, H., Warren-Oseni, K., Jones, K., Harris, V., Taylor, H., Khoo, V., Thomas, K., Hansen, V., Dearnaley, D., Horwich, A., and Huddart, R. (2017). **Clinical Outcomes of Image Guided Adaptive Hypofractionated Weekly Radiation Therapy for Bladder Cancer in Patients Unsuitable for Radical Treatment**. Int J Radiat Oncol Biol Phys, *98(1)*, 115–122.

Han, L., Dong, H., McClelland, J. R., Han, L., Hawkes, D. J., and Barratt, D. C. (2017). **A Hybrid Patient-Specific Biomechanical Model Based Image Registration Method for the Motion Estimation of Lungs**. Med Image Anal, 39, 87–100.

Hardcastle, N., Tomé, W. A., Cannon, D. M., Brouwer, C. L., Wittendorp, P. W., Dogan, N., Guckenberger, M., Allaire, S., Mallya, Y., Kumar, P., Oechsner, M., Richter, A., Song, S., Myers, M., Polat, B., and Bzdusek, K. (2012). **A Multi-Institution Evaluation of Deformable Image Registration Algorithms for Automatic Organ Delineation in Adaptive Head and Neck Radiotherapy**. Radiat Oncol, 7, 90.

Heijkoop, S. T., Langerak, T. R., Quint, S., Bondar, L., Mens, J. W. M., Heijmen, B. J. M., and Hoogeman, M. S. (2014). **Clinical Implementation of an Online Adaptive Plan-of-the-Day Protocol for Nonrigid Motion Management in Locally Advanced Cervical Cancer IMRT**. Int J Radiat Oncol Biol Phys, *90(3)*, 673–679.

Hill, D. L. G., Batchelor, P. G., Holden, M., and Hawkes, D. J. (2001). **Medical Image Registration**. Phys Med Biol, *46(3)*, R1–R45.

Hoffmann, L., Knap, M. M., Khalil, A. A., Lutz, C. M., and Møller, D. S. (2018). **The NARLAL2 Dose Escalation Trial: Dosimetric Implications of Inter-Fractional Changes in Organs at Risk**. Acta Oncol, *57(4)*, 473–479.

Holt, A., Van Gestel, D., Arends, M. P., Korevaar, E. W., Schuring, D., Kunze-Busch, M. C., Louwe, R. J., and van Vliet-Vroegindeweij, C. (2013). **Multi-Institutional Comparison of Volumetric Modulated Arc Therapy vs. Intensity-Modulated Radiation Therapy for Head-and-Neck Cancer: A Planning Study**. Radiat Oncol, 8, 26.

Holzbaur, K. R. S., Murray, W. M., and Delp, S. L. (2005). **A Model of the Upper Extremity for Simulating Musculoskeletal Surgery and Analyzing Neuromuscular Control**. Ann Biomed Eng, *33(6)*, 829–840.

Hsu, S.-H., Cao, Y., Huang, K., Feng, M., and Balter, J. M. (2013). **Investigation of a Method for Generating Synthetic CT Models from MRI Scans of the Head and Neck for Radiation Therapy**. Phys Med Biol, *58(23)*, 8419–8435.

Hu, Y., Zhou, Y.-K., Chen, Y.-X., and Zeng, Z.-C. (2017). **Magnitude and Influencing Factors of Respiration-Induced Liver Motion during Abdominal Compression in Patients with Intrahepatic Tumors**. Radiat Oncol, 12, 9.

International Commission on Radiation Units and Measurements (1993). **Prescribing, Recording, and Reporting Photon Beam Therapy**. Number 50 in ICRU report. International Commission on Radiation Units and Measurements, Bethesda, Md.

International Commission on Radiation Units and Measurements (1999). **Prescribing, Recording, and Reporting Photon Beam Therapy**. Number 62 in ICRU report. International Commission on Radiation Units and Measurements, Bethesda, Md.

Jain, A., Vaidehi, N., and Rodriguez, G. (1993). **A Fast Recursive Algorithm for Molecular Dynamics Simulation**. J Comput Phys, *106(2)*, 258–268.

Jensen, A. D., Nill, S., Huber, P. E., Bendl, R., Debus, J., and Münter, M. W. (2012a). **A Clinical Concept for Interfractional Adaptive Radiation Therapy in the Treatment of Head and Neck Cancer**. Int J Radiat Oncol Biol Phys, *82(2)*, 590–596.

Jensen, A. D., Winter, M., Kuhn, S. P., Debus, J., Nairz, O., and Münter, M. W. (2012b). **Robotic-Based Carbon Ion Therapy and Patient Positioning in 6 Degrees of Freedom: Setup Accuracy of Two Standard Immobilization Devices Used in Carbon Ion Therapy and IMRT**. Radiat Oncol, 7, 51.

Johansson, A., Karlsson, M., and Nyholm, T. (2011). **CT Substitute Derived from MRI Sequences with Ultrashort Echo Time**. Med Phys, 38, 2708–2714.

Joiner, M. C., Marples, B., Lambin, P., Short, S. C., and Turesson, I. (2001). **Low-Dose Hypersensitivity: Current Status and Possible Mechanisms**. Int J Radiat Oncol Biol Phys, *49(2)*, 379–389.

Juang, T., Das, S., Adamovics, J., Benning, R., and Oldham, M. (2013). **On the Need for Comprehensive Validation of Deformable Image Registration, Investigated With a Novel 3-Dimensional Deformable Dosimeter**. Int J Radiat Oncol Biol Phys, *87(2)*, 414–421.

Kainz, H., Modenese, L., Lloyd, D. G., Maine, S., Walsh, H. P. J., and Carty, C. P. (2016). **Joint Kinematic Calculation Based on Clinical Direct Kinematic versus Inverse Kinematic Gait Models**. J Biomech, *49(9)*, 1658–1669.

Kane, T. R., Likins, P. W., and Levinson, D. A. (1983). **Spacecraft Dynamics**. McGraw-Hill Book Company, New York, USA.

Kashani, R., Hub, M., Kessler, M. L., and Balter, J. M. (2007). **Technical Note: A Physical Phantom for Assessment of Accuracy of Deformable Alignment Algorithms**. Med Phys, *34(7)*, 2785–2788.

Kataria, T., Gupta, D., Goyal, S., Bisht, S. S., Basu, T., Abhishek, A., Narang, K., Banerjee, S., Nasreen, S., Sambasivam, S., and Dhyani, A. (2016). **Clinical Outcomes of Adaptive Radiotherapy in Head and Neck Cancers**. Br J Radiol, *89(1062)*, 20160085.

Keall, P. J., Kini, V. R., Vedam, S. S., and Mohan, R. (2002). **Potential Radiotherapy Improvements with Respiratory Gating**. Australas Phys Eng Sci Med, *25(1)*, 1–6.

Kessler, M. L. (2006). **Image Registration and Data Fusion in Radiation Therapy**. Br J Radiol, *79(special_issue_1)*, S99–S108.

Kim, J., Matuszak, M. M., Saitou, K., and Balter, J. M. (2013). **Distance-Preserving Rigidity Penalty on Deformable Image Registration of Multiple Skeletal Components in the Neck**. Med Phys, *40(12)*, 121907.

Kim, J., Saitou, K., Matuszak, M. M., and Balter, J. M. (2016). **A Finite Element Head and Neck Model as a Supportive Tool for Deformable Image Registration**. Int J Comput Assist Radiol Surg, *11(7)*, 1311–1317.

Kirby, N., Chuang, C., and Pouliot, J. (2011). **A Two-Dimensional Deformable Phantom for Quantitatively Verifying Deformation Algorithms: A 2D Phantom for Verifying Deformation Algorithms**. Med Phys, *38(8)*, 4583–4586.

Klein, S., Staring, M., Murphy, K., Viergever, M. A., and Pluim, J. P. W. (2010). **Elastix: A Toolbox for Intensity-Based Medical Image Registration**. IEEE Trans Med Imaging, *29(1)*, 196–205.

Klein, S., Staring, M., and Pluim, J. P. W. (2007). **Evaluation of Optimization Methods for Nonrigid Medical Image Registration Using Mutual Information and B-Splines**. IEEE Trans Image Process, *16(12)*, 2879–2890.

König, L., Derksen, A., Papenberg, N., and Haas, B. (2016). **Deformable Image Registration for Adaptive Radiotherapy with Guaranteed Local Rigidity Constraints**. Radiat Oncol, *11(1)*, 122.

Kontaxis, C., Bol, G. H., Kerkmeijer, L. G. W., Lagendijk, J. J. W., and Raaymakers, B. W. (2017). **Fast Online Replanning for Interfraction Rotation Correction in Prostate Radiotherapy**. Med Phys, *44(10)*, 5034–5042.

Kraaijenga, S., Oskam, I., van der Molen, L., Hamming, O., Hilgers, F., and van den Brekel, M. (2015). **Evaluation of Long Term (10-Years+) Dysphagia and Trismus in Patients Treated with Concurrent Chemo-Radiotherapy for Advanced Head and Neck Cancer**. Oral Oncol, *51(8)*, 787–794.

Kumagai, M., Hara, R., Mori, S., Yanagi, T., Asakura, H., Kishimoto, R., Kato, H., Yamada, S., Kandatsu, S., and Kamada, T. (2009). **Impact of Intrafractional Bowel Gas Movement on Carbon Ion Beam Dose Distribution in Pancreatic Radiotherapy**. Int J Radiat Oncol Biol Phys, *73(4)*, 1276–1281.

Laitenberger, M., Raison, M., Périé, D., and Begon, M. (2015). **Refinement of the Upper Limb Joint Kinematics and Dynamics Using a Subject-Specific Closed-Loop Forearm Model**. Multibody Syst Dyn, *33(4)*, 413–438.

Lambin, P., Marples, B., Fertil, B., Malaise, E. P., and Joiner, M. C. (1993). **Hypersensitivity of a Human Tumour Cell Line to Very Low Radiation Doses**. Int J Radiat Biol, *63(5)*, 639–650.

Lee, J., Carass, A., Jog, A., Zhao, C., and Prince, J. L. (2017). **Multi-Atlas-Based CT Synthesis from Conventional MRI with Patch-Based Refinement for MRI-Based Radiotherapy Planning**. Proc SPIE Int Soc Opt Eng, 10133.

Lee, S.-H., Sifakis, E., and Terzopoulos, D. (2009). **Comprehensive Biomechanical Modeling and Simulation of the Upper Body**. ACM Trans Graph, *28(4)*, 99.

Leeman, J. E., Romesser, P. B., Zhou, Y., McBride, S., Riaz, N., Sherman, E., Cohen, M. A., Cahlon, O., and Lee, N. (2017). **Proton Therapy for Head and Neck Cancer: Expanding the Therapeutic Window**. Lancet Oncol, *18(5)*, e254–e265.

Leibfarth, S., Mönnich, D., Welz, S., Siegel, C., Schwenzer, N., Schmidt, H., Zips, D., and Thorwarth, D. (2013). **A Strategy for Multimodal Deformable Image Registration to Integrate PET/MR into Radiotherapy Treatment Planning**. Acta Oncol, *52(7)*, 1353–1359.

Li, M., Miller, K., Joldes, G. R., Kikinis, R., and Wittek, A. (2016). **Biomechanical Model for Computing Deformations for Whole-body Image Registration: A Meshless Approach**. Int J Numer Method Biomed Eng, *32(12)*, e02771.

Li, Z. (2009). **Prescribing, Recording, and Reporting Proton-Beam Therapy**. Int J Radiat Biol, *73(5)*, 1602.

Lim-Reinders, S., Keller, B. M., Al-Ward, S., Sahgal, A., and Kim, A. (2017). **Online Adaptive Radiation Therapy**. Int J Radiat Oncol Biol Phys, *99(4)*, 994–1003.

Liu, D. C. and Nocedal, J. (1989). **On the Limited Memory BFGS Method for Large Scale Optimization**. Math Program, *45(1-3)*, 503–528.

Lo Nigro, C., Denaro, N., Merlotti, A., and Merlano, M. (2017). **Head and Neck Cancer: Improving Outcomes with a Multidisciplinary Approach**. Cancer Manag Res, 9, 363–371.

Lohr, F., Debus, J., Frank, C., Herfarth, K., Pastyr, O., Rhein, B., Bahner, M. L., Schlegel, W., and Wannenmacher, M. (1999). **Noninvasive Patient Fixation for Extracranial Stereotactic Radiotherapy**. International Journal of Radiation Oncology*Biology*Physics, *45(2)*, 521–527.

Lu, W., Chen, M.-L., Olivera, G. H., Ruchala, K. J., and Mackie, T. R. (2004). **Fast Free-Form Deformable Registration via Calculus of Variations**. Phys Med Biol, *49(14)*, 3067–3087.

Ludewig, P. M., Phadke, V., Braman, J. P., Hassett, D. R., Cieminski, C. J., and LaPrade, R. F. (2009). **Motion of the Shoulder Complex During Multiplanar Humeral Elevation:**. J Bone Joint Surg Am, *91(2)*, 378–389.

Luersen, M. A. and Le Riche, R. (2004). **Globalized Nelder–Mead Method for Engineering Optimization**. Comput Struct, *82(23)*, 2251–2260.

Macrini, D., Dickinson, S., Fleet, D., and Siddiqi, K. (2011). **Bone Graphs: Medial Shape Parsing and Abstraction**. Comput Vis Image Underst, *115(7)*, 1044–1061.

Maes, F., Collignon, A., Vandermeulen, D., Marchal, G., and Suetens, P. (1997). **Multimodality Image Registration by Maximization of Mutual Information**. IEEE Trans Med Imaging, *16(2)*, 187–198.

Maintz, J. B. and Viergever, M. A. (1998). **A Survey of Medical Image Registration**. Med Image Anal, *2(1)*, 1–36.

Mao, W., Rozario, T., Lu, W., Gu, X., Yan, Y., Jia, X., Sumer, B., and Schwartz, D. L. (2017). **Online Dosimetric Evaluation of Larynx SBRT: A Pilot Study to Assess the Necessity of Adaptive Replanning**. J Appl Clin Med Phys, *18(1)*, 157–163.

Mariappan, Y. K., Glaser, K. J., and Ehman, R. L. (2010). **MAGNETIC RESONANCE ELASTOGRAPHY: A REVIEW**. Clin Anat, *23(5)*, 497–511.

Marsaglia, G. (1972). **Choosing a Point from the Surface of a Sphere**. Annals of mathematical statistics, *43(2)*, 645–646.

Masarati, P. (2011). **Constraint Stabilization of Mechanical Systems in Ordinary Differential Equations Form**. Proceedings of the Institution of Mechanical Engineers, Part K: Journal of Multi-body Dynamics, *225(1)*, 12–33.

McGowan, S. E., Burnet, N. G., and Lomax, A. J. (2013). **Treatment Planning Optimisation in Proton Therapy**. Br J Radiol, *86(1021)*, 20120288.

Meijer, G. J., van der Toorn, P.-P., Bal, M., Schuring, D., Weterings, J., and de Wildt, M. (2012). **High Precision Bladder Cancer Irradiation by Integrating a Library Planning Procedure of 6 Prospectively Generated SIB IMRT Plans with Image Guidance Using Lipiodol Markers**. Radiother Oncol, *105(2)*, 174–179.

Meis, J., Teske, H., and Giske, K. (2017). **Abstract: Effiziente Visualisierung von Vektorfeldern in der Strahlentherapie**. In: Bildverarbeitung für die Medizin 2017, Informatik aktuell, pages 230–230. Springer Vieweg, Berlin, Heidelberg.

Meredith, M. and Maddock, S. (2004). **Real-Time Inverse Kinematics: The Return of the Jacobian**. Technical report, Technical Report No. CS-04-06, Department of Computer Science, University of Sheffield, United Kingdom.

Monheit, G. and Badler, N. I. (1991). **A Kinematic Model of the Human Spine and Torso**. IEEE Comput Graph Appl, *11(2)*, 29–38.

Mori, S., Wolfgang, J., Lu, H.-M., Schneider, R., Choi, N. C., and Chen, G. T. Y. (2008). **Quantitative Assessment of Range Fluctuations in Charged Particle Lung Irradiation**. Int J Radiat Oncol Biol Phys, *70(1)*, 253–261.

Moteabbed, M., Sharp, G. C., Wang, Y., Trofimov, A., Efstathiou, J. A., and Lu, H.-M. (2015). **Validation of a Deformable Image Registration Technique for Cone Beam CT-based Dose Verification**. Med Phys, *42(1)*, 196–205.

Mutic, S. and Dempsey, J. F. (2014). **The ViewRay System: Magnetic Resonance–Guided and Controlled Radiotherapy**. Semin Radiat Oncol, *24(3)*, 196–199.

Näf, M., Székely, G., Kikinis, R., Shenton, M. E., and Kübler, O. (1997). **3D Voronoi Skeletons and Their Usage for the Characterization and Recognition of 3D Organ Shape**. Comput Vis Image Underst, *66(2)*, 147–161.

Nealen, A., Müller, M., Keiser, R., Boxerman, E., and Carlson, M. (2006). **Physically Based Deformable Models in Computer Graphics**. Comput Graph Forum, *25(4)*, 809–836.

Nelder, J. A. and Mead, R. (1965). **A Simplex Method for Function Minimization**. Comput J, *7(4)*, 308–313.

Nevinny-Stickel, M., Sweeney, R. A., Bale, R. J., Posch, A., Auberger, T., and Lukas, P. (2004). **Reproducibility of Patient Positioning for Fractionated Extracranial Stereotactic Radiotherapy Using a Double-Vacuum Technique**. Strahlenther Onkol, *180(2)*, 117–122.

Neylon, J., Qi, X., Sheng, K., Staton, R., Pukala, J., Manon, R., Low, D. A., Kupelian, P., and Santhanam, A. (2014). **A GPU Based High-Resolution Multilevel Biomechanical Head and Neck Model for Validating Deformable Image Registration: High-Resolution Biomechanical Head and Neck Deformable Phantoms**. Med Phys, *42(1)*, 232–243.

Nocedal, J. and Wright, S. J. (1999). **Numerical Optimization**. Springer, New York, USA.

Nutting, C. M., Morden, J. P., Harrington, K. J., Urbano, T. G., Bhide, S. A., Clark, C., Miles, E. A., Miah, A. B., Newbold, K., Tanay, M., Adab, F., Jefferies, S. J., Scrase, C., Yap, B. K., A'Hern, R. P., Sydenham, M. A., Emson, M., and Hall, E. (2011). **Parotid-Sparing Intensity Modulated versus Conventional Radiotherapy in Head and Neck Cancer (PARSPORT): A Phase 3 Multicentre Randomised Controlled Trial**. Lancet Oncol, *12(2)*, 127–136.

Oelfke, U., Tücking, T., Nill, S., Seeber, A., Hesse, B., Huber, P., and Thilmann, C. (2006). **Linac-Integrated kV-Cone Beam CT: Technical Features and First Applications**. Med Dosim, *31(1)*, 62–70.

Oh, S. and Kim, S. (2017). **Deformable Image Registration in Radiation Therapy**. Radiation Oncology Journal, *35(2)*, 101–111.

Ostyn, M., Dwyer, T., Miller, M., King, P., Sacks, R., Cruikshank, R., Rosario, M., Martinez, D., Kim, S., and Yeo, W.-H. (2017). **An Electromechanical, Patient Positioning System for Head and Neck Radiotherapy**. Phys Med Biol, *62(18)*, 7520–7531.

Palágyi, K. and Kuba, A. (1997). **A Thinning Algorithm to Extract Medial Lines from 3D Medical Images**. In: Information Processing in Medical Imaging, Lecture Notes in Computer Science, pages 411–416. Springer, Berlin, Heidelberg.

Palma, D., Vollans, E., James, K., Nakano, S., Moiseenko, V., Shaffer, R., McKenzie, M., Morris, J., and Otto, K. (2008). **Volumetric Modulated Arc Therapy for Delivery of Prostate Radiotherapy: Comparison With Intensity-Modulated Radiotherapy and Three-Dimensional Conformal Radiotherapy**. Int J Radiat Oncol Biol Phys, *72(4)*, 996–1001.

Peng, C., Chen, G., Ahunbay, E., Wang, D., Lawton, C., and Li, X. A. (2011). **Validation of an Online Replanning Technique for Prostate Adaptive Radiotherapy**. Phys Med Biol, *56(12)*, 3659–3668.

Pluim, J. P. W., Antoine Maintz, J. B., and Viergever, M. A. (2000). **Interpolation Artefacts in Mutual Information-Based Image Registration**. Comput Vis Image Underst, *77(2)*, 211–232.

Polan, D. F., Feng, M., Lawrence, T. S., Haken, R. K. T., and Brock, K. K. (2017). **Implementing Radiation Dose-Volume Liver Response in Biomechanical Deformable Image Registration**. Int J Radiat Oncol Biol Phys, *99(4)*, 1004–1012.

Pollack, A. and Ahmed, M. M. (2011). **Hypofractionation: Scientific Concepts and Clinical Experiences**. LumiText Publishing, Ellicott City, Maryland, USA.

Press, W. H. and Teukolsky, S. A. (1991). **Simulated Annealing Optimization over Continuous Spaces**. Computers in Physics, *5(4)*, 426–429.

Pukala, J., Meeks, S. L., Staton, R. J., Bova, F. J., Mañon, R. R., and Langen, K. M. (2013). **A Virtual Phantom Library for the Quantification of Deformable Image Registration Uncertainties in Patients with Cancers of the Head and Neck: Virtual Phantoms for the Quantification of DIR Uncertainty**. Med Phys, *40(11)*, 111703.

Pyo, S. H., Lee, J., Park, S., Kim, K. W., Shin, Y. G., and Kim, B. (2013). **Physically Based Nonrigid Registration Using Smoothed Particle Hydrodynamics: Application to Hepatic Metastasis Volume-Preserving Registration**. IEEE Trans Biomed Eng, *60(9)*, 2530–2540.

Qin, A., Liang, J., Han, X., O'Connell, N., and Yan, D. (2018). **Technical Note: The Impact of Deformable Image Registration Methods on Dose Warping**. Med Phys, *45(3)*, 1287–1294.

Quadros, W. R., Owen, S. J., Brewer, M., and Shimada, K. (2004). **Finite Element Mesh Sizing for Surfaces Using Skeleton**. In: In 13th International Meshing Roundtable, Williamsburg, VA, 2004, Sandia National Laboratories, pages 389–400.

Rahami, H., Kaveh, A., Aslani, M., and Najian Asl, R. (2011). **A HYBRID MODIFIED GENETIC-NELDER MEAD SIMPLEX ALGORITHM FOR LARGE-SCALE TRUSS OPTIMIZATION**. International Journal of Optimization in Civil Engineering, *1(1)*, 29–46.

Ramkumar, A., Dolz, J., Kirisli, H. A., Adebahr, S., Schimek-Jasch, T., Nestle, U., Massoptier, L., Varga, E., Stappers, P. J., Niessen, W. J., and Song, Y. (2016). **User Interaction in Semi-Automatic Segmentation of Organs at Risk: A Case Study in Radiotherapy**. J Digit Imaging, *29(2)*, 264–277.

Rodríguez Aguilera, A., León Salas, A., Martín Perandrés, D., and Otaduy, M. A. (2015). **A Parallel Resampling Method for Interactive Deformation of Volumetric Models**. Comput Graph, 53, 147–155.

Romesser, P. B., Cahlon, O., Scher, E., Zhou, Y., Berry, S. L., Rybkin, A., Sine, K. M., Tang, S., Sherman, E. J., Wong, R., and Lee, N. Y. (2016). **Proton Beam Radiation Therapy Results in Significantly Reduced Toxicity Compared with Intensity-Modulated Radiation Therapy for Head and Neck Tumors That Require Ipsilateral Radiation**. Radiother Oncol, *118(2)*, 286–292.

Roy, S., Carass, A., Jog, A., Prince, J. L., and Lee, J. (2014). **MR to CT Registration of Brains Using Image Synthesis**. Proc SPIE Int Soc Opt Eng, 9034.

Sahara, W., Sugamoto, K., Murai, M., Tanaka, H., and Yoshikawa, H. (2006). **3D Kinematic Analysis of the Acromioclavicular Joint during Arm Abduction Using Vertically Open MRI**. J Orthop Res, *24(9)*, 1823–1831.

Saleh-Sayah, N. K., Weiss, E., Salguero, F. J., and Siebers, J. V. (2011). **A Distance to Dose Difference Tool for Estimating the Required Spatial Accuracy of a Displacement Vector Field**. Med Phys, *38(5)*, 2318–2323.

Samant, S. S., Xia, J., Muyan-Özçelik, P., and Owens, J. D. (2008). **High Performance Computing for Deformable Image Registration: Towards a New Paradigm in Adaptive Radiotherapy**. Med Phys, *35(8)*, 3546–3553.

Santivasi, W. L. and Xia, F. (2013). **Ionizing Radiation-Induced DNA Damage, Response, and Repair**. Antioxid Redox Signal, *21(2)*, 251–259.

Sarkalkan, N., Weinans, H., and Zadpoor, A. A. (2014). **Statistical Shape and Appearance Models of Bones**. Bone, 60, 129–140.

Sarrut, D. (2006). **Deformable Registration for Image-Guided Radiation Therapy**. Z Med Phys, *16(4)*, 285–297.

Sarrut, D., Boldea, V., Miguet, S., and Ginestet, C. (2006). **Simulation of Four-dimensional CT Images from Deformable Registration between Inhale and Exhale Breath-hold CT Scans**. Med Phys, *33(3)*, 605–617.

Schill, M. A., Gibson, S. F. F., Bender, H.-J., and Männer, R. (1998). **Biomechanical Simulation of the Vitreous Humor in the Eye Using an Enhanced Chain-Mail Algorithm**. In: Medical Image Computing and Computer-Assisted Intervention — MICCAI'98, Lecture Notes in Computer Science, pages 679–687. Springer, Berlin, Heidelberg.

Schwartz, D. L. and Dong, L. (2011). **Adaptive Radiation Therapy for Head and Neck Cancer?Can an Old Goal Evolve into a New Standard?** J Oncol, 2011, 1–13.

Schwartz, D. L., Garden, A. S., Shah, S. J., Chronowski, G., Sejpal, S., Rosenthal, D. I., Chen, Y., Zhang, Y., Zhang, L., Wong, P.-F., Garcia, J. A., Kian Ang, K., and Dong, L. (2013). **Adaptive Radiotherapy for Head and Neck Cancer—Dosimetric Results from a Prospective Clinical Trial**. Radiother Oncol, *106(1)*, 80–84.

Schwartz, D. L., Garden, A. S., Thomas, J., Chen, Y., Zhang, Y., Lewin, J., Chambers, M. S., and Dong, L. (2012). **Adaptive Radiotherapy for Head and Neck Cancer: Initial Clinical Outcomes from a Prospective Trial**. Int J Radiat Oncol Biol Phys, *83(3)*, 986–993.

Scorsetti, M., Bignardi, M., Clivio, A., Cozzi, L., Fogliata, A., Lattuada, P., Mancosu, P., Navarria, P., Nicolini, G., Urso, G., Vanetti, E., Vigorito, S., and Santoro, A. (2010). **Volumetric Modulation Arc Radiotherapy Compared With Static Gantry Intensity-Modulated Radiotherapy for Malignant Pleural Mesothelioma Tumor: A Feasibility Study**. Int J Radiat Oncol Biol Phys, *77(3)*, 942–949.

Segars, W. P., Bond, J., Frush, J., Hon, S., Eckersley, C., Williams, C. H., Feng, J., Tward, D. J., Ratnanather, J. T., Miller, M. I., Frush, D., and Samei, E. (2013). **Population of Anatomically Variable 4D XCAT Adult Phantoms for Imaging Research and Optimization**. Med Phys, *40(4)*, 043701.

Seppenwoolde, Y., Stock, M., Buschmann, M., Georg, D., Bauer-Novotny, K.-Y., Pötter, R., and Georg, P. (2016). **Impact of Organ Shape Variations on Margin Concepts for Cervix Cancer ART**. Radiother Oncol, *120(3)*, 526–531.

Seth, A., Matias, R., Veloso, A. P., and Delp, S. L. (2016). **A Biomechanical Model of the Scapulothoracic Joint to Accurately Capture Scapular Kinematics during Shoulder Movements**. PLoS One, *11(1)*, e0141028.

Seth, A., Sherman, M., Eastman, P., and Delp, S. (2010). **Minimal Formulation of Joint Motion for Biomechanisms**. Nonlinear Dyn, *62(1-2)*, 291–303.

Sharfo, A. W. M., Breedveld, S., Voet, P. W. J., Heijkoop, S. T., Mens, J.-W. M., Hoogeman, M. S., and Heijmen, B. J. M. (2016). **Validation of Fully Automated VMAT Plan Generation for Library-Based Plan-of-the-Day Cervical Cancer Radiotherapy**. PLoS One, *11(12)*, e0169202.

Sharp, G., LI, R., Wolfgang, J., Chen, G., Peroni, M., Spadea, M., Mori, S., Zhang, J., Shackleford, J., and Kandasamy, N. (2010). **Plastimatch - An Open Source Software Suite for Radiotherapy Image Processing**. In: Proceedings of the XVIth ICCR.

Sherman, M. A., Seth, A., and Delp, S. L. (2011). **Simbody: Multibody Dynamics for Biomedical Research**. Procedia IUTAM, 2, 241–261.

Shusharina, N. and Sharp, G. (2012). **Analytic Regularization for Landmark-Based Image Registration**. Phys Med Biol, *57(6)*, 1477–1498.

Sims, R., Isambert, A., Grégoire, V., Bidault, F., Fresco, L., Sage, J., Mills, J., Bourhis, J., Lefkopoulos, D., Commowick, O., Benkebil, M., and Malandain, G. (2009). **A Pre-Clinical Assessment of an Atlas-Based Automatic Segmentation Tool for the Head and Neck**. Radiother Oncol, *93(3)*, 474–478.

Sotiras, A., Davatzikos, C., and Paragios, N. (2013). **Deformable Medical Image Registration: A Survey**. IEEE Trans Med Imaging, *32(7)*, 1153–1190.

Steneker, M., Lomax, A., and Schneider, U. (2006). **Intensity Modulated Photon and Proton Therapy for the Treatment of Head and Neck Tumors**. Radiother Oncol, *80(2)*, 263–267.

Stewart, B. W., Wild, C., International Agency for Research on Cancer, and World Health Organization (2014). **World Cancer Report 2014**. International Agency for Research on Cancer, Lyon, France.

Stieler, F., Wolff, D., Schmid, H., Welzel, G., Wenz, F., and Lohr, F. (2011). **A Comparison of Several Modulated Radiotherapy Techniques for Head and Neck Cancer and Dosimetric Validation of VMAT**. Radiother Oncol, *101(3)*, 388–393.

Stoiber, E. M., Schwarz, M., Debus, J., Bendl, R., and Giske, K. (2014). **An Optimised IGRT Correction Vector Determined from a Displacement Vector Field: A Proof of Principle of a Decision-Making Aid for Re-Planning**. Acta Oncol, *53(1)*, 33–39.

Teece, R. M., Lunden, J. B., Lloyd, A. S., Kaiser, A. P., Cieminski, C. J., and Ludewig, P. M. (2008). **Three-Dimensional Acromioclavicular Joint Motions During Elevation of the Arm**. J Orthop Sports Phys Ther, *38(4)*, 181–190.

Teske, H., Bartelheimer, K., Bendl, R., Stoiber, E. M., and Giske, K. (2017a). **Handling Images of Patient Postures in Arms up and Arms down Position Using a Biomechanical Skeleton Model**. Current Directions in Biomedical Engineering, *3(2)*, 469–472.

Teske, H., Bartelheimer, K., Meis, J., Bendl, R., Stoiber, E. M., and Giske, K. (2017b). **Construction of a Biomechanical Head and Neck Motion Model as a Guide to Evaluation of Deformable Image Registration**. Phys Med Biol, *62(12)*, N271–N284.

Thames, H. D., Peters, L. T., Withers, H. R., and Fletcher, G. H. (1983). **Accelerated Fractionation vs Hyperfractionation: Rationales for Several Treatments per Day**. Int J Radiat Oncol Biol Phys, *9(2)*, 127–138.

Thieke, C., Malsch, U., Schlegel, W., Debus, J., Huber, P., Bendl, R., and Thilmann, C. (2006). **Kilovoltage CT Using a Linac-CT Scanner Combination**. Br J Radiol, *79(special_issue_1)*, S79–S86.

Tilly, D., Tilly, N., and Ahnesjö, A. (2013). **Dose Mapping Sensitivity to Deformable Registration Uncertainties in Fractionated Radiotherapy–applied to Prostate Proton Treatments**. BMC Med Phys, *13(1)*, 2.

Trofimov, A., Nguyen, P. L., Efstathiou, J. A., Wang, Y., Lu, H.-M., Engelsman, M., Merrick, S., Cheng, C.-W., Wong, J. R., and Zietman, A. L. (2011). **Interfractional Variations in the Set-up of Pelvic Bony Anatomy and Soft Tissue, and Their Implications on the Delivery of Proton Therapy for Localized Prostate Cancer**. Int J Radiat Oncol Biol Phys, *80(3)*, 928–937.

Unser, M. (1999). **Splines: A Perfect Fit for Signal and Image Processing**. IEEE Signal Process Mag, *16(6)*, 22–38.

van de Schoot, A. J. A. J., de Boer, P., Visser, J., Stalpers, L. J. A., Rasch, C. R. N., and Bel, A. (2017). **Dosimetric Advantages of a Clinical Daily Adaptive Plan Selection Strategy Compared with a Non-Adaptive Strategy in Cervical Cancer Radiation Therapy**. Acta Oncol, *56(5)*, 667–674.

van Herk, M. (2004). **Errors and Margins in Radiotherapy**. Semin Radiat Oncol, *14(1)*, 52–64.

van Herk, M., Remeijer, P., Rasch, C., and Lebesque, J. V. (2000). **The Probability of Correct Target Dosage: Dose-Population Histograms for Deriving Treatment Margins in Radiotherapy**. Int J Radiat Oncol Biol Phys, *47(4)*, 1121–1135.

van Kranen, S., Hamming-Vrieze, O., Wolf, A., Damen, E., van Herk, M., and Sonke, J.-J. (2016). **Head and Neck Margin Reduction With Adaptive Radiation Therapy: Robustness of Treatment Plans Against Anatomy Changes**. Int J Radiat Oncol Biol Phys, *96(3)*, 653–660.

van Kranen, S., van Beek, S., Rasch, C., van Herk, M., and Sonke, J.-J. (2009). **Setup Uncertainties of Anatomical Sub-Regions in Head-and-Neck Cancer Patients After Offline CBCT Guidance**. Int J Radiat Oncol Biol Phys, *73(5)*, 1566–1573.

Veeger, H. E. J. (2000). **The Position of the Rotation Center of the Glenohumeral Joint**. J Biomech, *33(12)*, 1711–1715.

Vidal, F. P. and Villard, P.-F. (2016). **Development and Validation of Real-Time Simulation of X-Ray Imaging with Respiratory Motion**. Comput Med Imaging Graph, 49, 1–15.

Vinod, S. K., Min, M., Jameson, M. G., and Holloway, L. C. (2016). **A Review of Interventions to Reduce Inter-observer Variability in Volume Delineation in Radiation Oncology**. J Med Imaging Radiat Oncol, *60(3)*, 393–406.

Wampler, C. W. (1986). **Manipulator Inverse Kinematic Solutions Based on Vector Formulations and Damped Least-Squares Methods**. IEEE Trans Syst Man Cybern, *16(1)*, 93–101.

Wang, J. and Tan, Y. (2013). **Efficient Euclidean Distance Transform Algorithm of Binary Images in Arbitrary Dimensions**. Pattern Recognit, *46(1)*, 230–242.

Wang, L. C. T. and Chen, C. C. (1991). **A Combined Optimization Method for Solving the Inverse Kinematics Problems of Mechanical Manipulators**. IEEE Trans Rob Autom, *7(4)*, 489–499.

Weistrand, O. and Svensson, S. (2014). **The ANACONDA Algorithm for Deformable Image Registration in Radiotherapy: ANACONDA for DIR**. Med Phys, *42(1)*, 40–53.

West, K., Russo, M., Brown, E., Barry, T., Hargrave, C., and Pryor, D. (2018). **Evaluation of Kidney Motion with and without a Pneumatic Abdominal Compression Belt: Considerations for Stereotactic Radiotherapy**. J Med Imaging Radiat Oncol, *62(1)*, 128–132.

Whitfield, G. A., Price, P., Price, G. J., and Moore, C. J. (2013). **Automated Delineation of Radiotherapy Volumes: Are We Going in the Right Direction?** Br J Radiol, *86(1021)*, 20110718.

Whitney, D. E. (1969). **Resolved Motion Rate Control of Manipulators and Human Prostheses**. IEEE Transactions on Man-Machine Systems, *10(2)*, 47–53.

Withers, H. R. (1993). **Hyperfractionation**. In: Current Topics in Clinical Radiobiology of Tumors, Medical Radiology, pages 45–50. Springer, Berlin, Heidelberg.

Witte, M. G., Sonke, J.-J., Siebers, J., Deasy, J. O., and van Herk, M. (2017). **Beyond the Margin Recipe: The Probability of Correct Target Dosage and Tumor Control in the Presence of a Dose Limiting Structure**. Phys Med Biol, *62(19)*, 7874–7888.

Wolovich, W. A. and Elliott, H. (1984). **A Computational Technique for Inverse Kinematics**. In: The 23rd IEEE Conference on Decision and Control, pages 1359–1363.

Wu, G., Siegler, S., Allard, P., Kirtley, C., Leardini, A., Rosenbaum, D., Whittle, M., D D'Lima, D., Cristofolini, L., Witte, H., and others (2002). **ISB Recommendation on Definitions of Joint Coordinate System of Various Joints for the Reporting of Human Joint Motion—part I: Ankle, Hip, and Spine**. J Biomech, *35(4)*, 543–548.

Wu, G., van der Helm, F. C., Veeger, H., Makhsous, M., Van Roy, P., Anglin, C., Nagels, J., Karduna, A. R., McQuade, K., Wang, X., Werner, F. W., and Buchholz, B. (2005). **ISB Recommendation on Definitions of Joint Coordinate Systems of Various Joints for the Reporting of Human Joint Motion—Part II: Shoulder, Elbow, Wrist and Hand**. J Biomech, *38(5)*, 981–992.

Wu, G., Yap, P.-T., Kim, M., and Shen, D. (2010). **TPS-HAMMER: Improving HAMMER Registration Algorithm by Soft Correspondence Matching and Thin-Plate Splines Based Deformation Interpolation**. NeuroImage, *49(3)*, 2225–2233.

Wu, Q., Chi, Y., Chen, P. Y., Krauss, D. J., Yan, D., and Martinez, A. (2009). **Adaptive Replanning Strategies Accounting for Shrinkage in Head and Neck IMRT**. Int J Radiat Oncol Biol Phys, *75(3)*, 924–932.

Wu, Q., Liang, J., and Yan, D. (2006). **Application of Dose Compensation in Image-Guided Radiotherapy of Prostate Cancer**. Phys Med Biol, *51(6)*, 1405–1419.

Xia, H. and Tucker, P. G. (2009a). **Distance Solutions for Medial Axis Transform**. In: Proceedings of the 18th International Meshing Roundtable, pages 247–265. Springer, Berlin, Heidelberg.

Xia, H. and Tucker, P. G. (2009b). **Finite Volume Distance Field and Its Application to Medial Axis Transforms**. Int J Numer Methods Eng, 82, 114–134.

Yan, D. (2008). **Developing Quality Assurance Processes for Image-Guided Adaptive Radiation Therapy**. Int J Radiat Oncol Biol Phys, *71(1, Supplement)*, S28–S32.

Yang, H., Hu, W., Wang, W., Chen, P., Ding, W., and Luo, W. (2013). **Replanning During Intensity Modulated Radiation Therapy Improved Quality of Life in Patients With Nasopharyngeal Carcinoma**. Int J Radiat Oncol Biol Phys, *85(1)*, e47–e54.

Yip, S., Chen, A. B., Aerts, H. J. W. L., and Berbeco, R. (2014). **Sensitivity Study of Voxel-Based PET Image Comparison to Image Registration Algorithms: Sensitivity of PET Image Comparison to Registration Algorithms**. Med Phys, *41(11)*, 111714.

Zhang, T., Chi, Y., Meldolesi, E., and Yan, D. (2007). **Automatic Delineation of On-Line Head-And-Neck Computed Tomography Images: Toward On-Line Adaptive Radiotherapy**. Int J Radiat Oncol Biol Phys, *68(2)*, 522–530.

Zhao, J. and Badler, N. I. (1994). **Inverse Kinematics Positioning Using Nonlinear Programming for Highly Articulated Figures**. ACM Trans Graph, *13(4)*, 313–336.

Zhong, H., Kim, J., and Chetty, I. J. (2010). **Analysis of Deformable Image Registration Accuracy Using Computational Modeling: FEM Simulation for Analysis of DIR Accuracy**. Med Phys, *37(3)*, 970–979.

Publications

Partial results of this dissertation were published in advance:

Peer reviewed journal publications

1. Teske, H., Bartelheimer, K., Meis, J., Bendl, R., Stoiber, E. M. and Giske, K. (2017). **Construction of a biomechanical head and neck motion model as a guide to evaluation of deformable image registration**. Phys Med Biol, *62(12)*, N271.

2. Teske, H., Bartelheimer, K., Bendl, R., Stoiber, E. M. and Giske, K. (2017). **Handling images of patient postures in arms up arms down positioning using a biomechanical skeleton model**. Current Directions in Biomedical Engineering, *3(2)*, 469-472.

3. Bartelheimer, Teske, H., Bendl, R. and Giske, K. (2017). **Tissue-specific transformation model for CT-images**. Current Directions in Biomedical Engineering, *3(2)*, 525-528.

Conference proceedings

4. Teske, H., Bartelheimer, K., Meis, J.,Stoiber, E. M., Bendl, R. and Giske, K. (2017). **Abstract: Articulated Head and Neck Patient Model for Adaptive Radiotherapy**. In: Meier-Hein, K. H., Deserno, T. M., Handels, H. and Tolxdorff, T., eds, Bildverarbeitung für die Medizin 2017, Springer, Berlin, Heidelberg, pp. 260-262.

5. Teske, H., Bierstedt, C., Stoll, M., Stoiber, E. M., Bendl, R. and Giske, K. (2016). **Articulated head and neck patient model in the context of ART**. International Conference on the use of Computers in Radiation Therapy, London, United Kingdom.

6. Teske, H., Stoiber, E. M., Bendl, R. and Giske, K. (2016). **Articulated head and neck patient model in the context of ART**. 2nd Heidelberg Symposium on Novel Techniques in Ion Beam Radiotherapy, Heidelberg.

7. Meis, J., Teske, H. and Giske, K. (2017). **Abstract: Effiziente Visualisierung von Vektorfeldern in der Strahlentherapie**. In: Meier-Hein, K. H., Deserno, T. M., Handels, H. and Tolxdorff, T., eds, Bildverarbeitung für die Medizin 2017, Springer, Berlin, Heidelberg, pp. 230-230.

8. Bartelheimer, K., Teske, H., Bendl, R. and Giske, K. (2017). **Abstract: Soft Tissue Modelling with the Chainmail Approach**. In: Meier-Hein, K. H., Deserno, T. M., Handels, H. and Tolxdorff, T., eds, Bildverarbeitung für die Medizin 2017, Springer, Berlin, Heidelberg, pp. 318-318.

9. Bartelheimer, K., Merz, J., Teske, H., Bendl, R. and Giske, K. (2016). **EP-1903: Application of the Enhanced ChainMail algorithm with inter-element rotation in adaptive radiotherapy**. Radiother Oncol, *119*, S901-S902.

Publication 1 describes the construction of the biomechanical model based on section 3.1 of this dissertation. The construction is demonstrated on the same image data of a head and neck cancer patient as referred to patient 1 in this dissertation. Furthermore, the application of the deformation model for the purpose of validating deformable image registration algorithms in clinically implemented treatment planning systems is discussed in this publication. This potential application is also included in the discussion part of this dissertation in section 4.4. My contribution to this publication reaches from the preparation of the image data in terms of manual segmentation of the bones, the software-based implementation of the kinematic model and realization of the interface to couple the soft tissue deformation model, the generation of exemplary postures using the bio-mechanical model and writing the major parts of the publication except the methodology of the soft tissue deformation model. The soft tissue deformation model developed by K. Bartelheimer is used with the input of the resulting transformations of the bones.

Publication 2 covers the refinement of the localization of rotation centres for specified joints as described in section 3.1.3 of this dissertation. Moreover, the potential use-case of the kinematic model to represent large posture changes such as the arms-up arms-down motion for patient 2 (see section 2.3) is demonstrated and achieved qualitative results and quantitative results are part of this dissertation and can be found in section 3.3. The idea with of including an arms-up arms-down patient was adopted in this dissertation as part of the evaluation of the kinematic model in section 3.2 and the evaluation of the automated kinematics-based registration approach found in section 3.4.2. My contribution was the data preparation, the parametrization of the kinematic deformation model, the implementation of the joint refinements, running of the experiments, extraction of the results and writing of the publication. The coupled soft tissue deformation model was developed by K. Bartelheimer.

Publication 3 and publication 8 and publication 9 describe the soft tissue deformation model, which is used for this dissertation for the purpose of propagating the transformations of the bones into the surrounding tissue (as described in 2.7.3), except for the implemented volume preservation during deformation. The aspect of volume preservation as an extension to the chainmail model is briefly mentioned in section 2.7.3. Moreover, results of the combined biomechanical model, consisting of the kinematic model for the bones and the chainmail-based model for the soft tissue are qualitatively shown for the purpose of posture generation in section 3.3 and in the resulting image overlays of section 3.4 as part of the registration approach. While the soft tissue model is developed by K. Bartelheimer, my contribution to these publications were mainly focused on the generation of skeletal postures with the kinematic model as initialization for the soft-tissue deformation model, the provision of an interface to the designed application, which is also used for posture generation (see section 3.3) as well as sharing of the extracted geometry of the skeleton.

Publication 4 and publication 5 and publication 6 are conference proceedings with the purpose of sharing the concept of the proposed kinematic model with the scientific community. The delivered concepts and ideas in general are also addressed in this dissertation.

Publication 7 describes a novel technique for improving the visualization of DVFs in 3D rendering scenes. The proposed approach is implemented in the designed application, which is also used for the interactive posture generation as described in section 3.3. My contribution to this work was the involvement in the conceptual idea, the assistance of J. Meis during the implementation and provision of an interface to the main application.

Further publications

10. Stoiber, E. M., Bougatf, N., Teske, H., Bierstedt, C., Oetzel, D., Debus, J., Bendl, R. and Giske, K. (2017). **Analyzing human decisions in IGRT of head-and-neck cancer patients to teach image registration algorithms what experts know**. Radiat Oncol, *12*, 104.

11. Paredes, L., Mercea, P., Teske, H., Bendl, R., Giske, K. and Espinoza, I. (2017). **Abstract: 4D Template Library Generation for Real-Time Tracking on 2D Cine MRI**. In: Meier-Hein, K. H., Deserno, T. M., Handels, H. and Tolxdorff, T., eds, Bildverarbeitung für die Medizin 2017, Springer, Berlin, Heidelberg, pp. 267-267.

12. Bierstedt, C., Mercea, P., Teske, H., Stoll, M., Löpprich, K., Heib, K., Müssemann, H., Back, S., Pfaffenberger, A., Giske, K., Jäkel, O., Bendl, R. (2016). **byst: Tackling the challenges of adaptive radiation therapy with a novel workflow-based software**. International Conference on the use of Computers in Radiation Therapy, London, United Kingdom.

13. Teske, H., Mercea, P., Schwarz, M., Nicolay, N. H., Sterzing, F. and Bendl, R. (2015). **Real-time markerless lung tumor tracking in fluoroscopic video: Handling overlapping of projected structures**. Med Phys, *42(5)*, 2540-2549.

14. Teske, H., Mercea, P., Giske, K. and Bendl, R. (2015). **PO-1121 Model based 2D localization of lung tumors by incorporating the motion of diaphragm and heart**. Radiother Oncol, *115*, S608-S609.

15. Mercea, P., Teske, H., Giske, K., Bendl, R. (2015). **Adaptive search area template matching for image-based lung tumor tracking**. Radiother Oncol, *115*, S228-S229.

16. Teske, H., Giske, K. and Bendl, R. (2014). **Localization of lung tumors despite limited tumor visibility: Tracking anatomical structures in near proximity to model the tumor motion**. In: Klöck, S., 44th Joint Conference of the SSRMP, DGMP, ÖGMP, Dreiländertagung für Medizinische Physik, Zürich, pp. 102-103.

17. Schwarz, M., Teske, H., Stoll, M. and Bendl, R. (2014). **Improving accuracy of markerless tracking of lung tumours in fluoroscopic video by incorporating diaphragm motion**. J Phys Conf Ser, *489(1)*, 012082.

18. Teske, H., Schwarz, M., Sterzing, F. and Bendl, R. (2013). **Multiple-template approach to deal with overlapping effects in fluoroscopic tracking of lung tumors**. In: Treuer, H., Deutsche Gesellschaft für Medizinische Physik (DGMP), Köln, pp. 670-671.

Curriculum Vitae

Personal

Name:	Hendrik Tim Teske
Date of birth:	16.09.1987
Place of birth:	Heilbronn, Germany
Marital status:	unmarried
Father:	Manfred Teske
Mother:	Ruth Teske (née Knapp)

Pre-university education

1998 – 2007	Eduard-Mörike-Gymnasium, Neuenstadt a.K.
21.06.2007	Abitur

University education

WS 2008 – SS 2011	Heidelberg University / Heilbronn University Medical Informatics (Bachelor)
28.09.2011	Graduation Bachelor of Science (B.Sc.)
WS 2011 – WS 2013	Heidelberg University / Heilbronn University Medical Informatics (Master)
13.12.2013	Graduation Master of Science (M.Sc.)
2014 – 2018	German Cancer Research Center (DKFZ) Heidelberg PhD candidate at Medical Physics in Radiation Oncology

XXIV

Acknowledgements

First of all I would like to thank Prof. Dr. Oliver Jäkel for taking the role as a supervisor for my PhD project, for making it possible to attend international conferences to discuss project related details and further improve my knowledge about the field of medical physics and for the pleasant working atmosphere in the division.

My exceptional gratitude is dedicated to Dr. Kristina Giske and Prof. Dr. Rolf Bendl. Thank you Kristina for being my direct mentor, sparring partner, motivator, caregiver, colleague and friend in one person. Thank you for having confidence in me as your first PhD candidate in the marvellous E0401 - *Computational Patient Models* and for the everlasting motivation even during the darkest days in the 'submarine'. Mr. Bendl, thank you for paving my way up till now, in being the Professor during my university education and in opening the doors way to the DKFZ for my bachelor and master thesis. Thanks for being an advisor for various research tasks and for supplying the demand for new student assistants, bachelor students and master students with computer science background to support my project.

I would also like to express my gratitude to all former and current members of the groups E0401, E0403, E0409 and E076 for the wonderful time we spent together during lunch, coffee breaks, social activities and of course scientific projects and meetings. In particular, thank you Dr. Paul Mercea, Christian Bierstedt, Markus Stoll, Kathrin Bartelheimer, Dr. Kristina Giske, Dr. Eva Stoiber and all others for considerably contributing to the great team spirit and for creating a worthwhile time to enjoy. My thanks also go to Jan Meis and Alexander Bauer for enriching my project with great new functionalities and visualizations.

Last but not least I would like to thank my family, my mother Ruth, my father Manfred and my brother Sören for fully supporting my visions and decisions along my path. Thank you for your confidence and your persistent patience.

XXVI

Eidesstattliche Versicherung

1. Bei der eingereichten Dissertation zu dem Thema

   ....
   handelt es sich um meine eigenständig erbrachte Leistung.

2. Ich habe nur die angegebenen Quellen und Hilfsmittel benutzt und mich keiner unzulässigen Hilfe Dritter bedient. Insbesondere habe ich wörtlich oder sinngemäß aus anderen Werken übernommene Inhalte als solche kenntlich gemacht.

3. Die Arbeit oder Teile davon habe ich bislang nicht an einer Hochschule des In- oder Auslands als Bestandteil einer Prüfungs- oder Qualifikationsleistung vorgelegt.

4. Die Richtigkeit der vorstehenden Erklärungen bestätige ich.

5. Die Bedeutung der eidesstattlichen Versicherung und die strafrechtlichen Folgen einer unrichtigen oder unvollständigen eidesstattlichen Versicherung sind mir bekannt. Ich versichere an Eides statt, dass ich nach bestem Wissen die reine Wahrheit erklärt und nichts verschwiegen habe.

Ort und Datum   Unterschrift

XXVIII